ScuDo

Scuola di Dottorato ~ Doctoral School

WHAT YOU ARE, TAKES YOU FAR

Doctoral Dissertation

Doctoral Program in Environmental Engineering (*XXXI*cycle)

Linear and weakly nonlinear analyses of morphological instabilities

By

Matteo Bernard Bertagni

******

Supervisor:

Prof. Carlo Camporeale

Doctoral Examination Committee:

Prof. Guido Zolezzi, Referee, University of Trento, Italy

Prof. Stephen Morris, Referee, University of Toronto, Canada

Politecnico di Torino

2019

Declaration

I hereby declare that, the contents and organization of this dissertation constitute my own original work and does not compromise in any way the rights of third parties, including those relating to the security of personal data.

Matteo Bernard Bertagni
2019

* This dissertation is presented in partial fulfillment of the requirements for **Ph.D. degree** in the Graduate School of Politecnico di Torino (ScuDo).

Everything you can imagine, nature has already created.

Albert Einstein

Acknowledgements

First and foremost, I would like to express my gratitude to my supervisor Carlo Camporeale, for being a bright and inventive mentor. Most of the personal and scientific growth I have experienced in these three years is thank to him.

I acknowledge Prof. Paolo Perona from the University of Edinburgh, for the fruitful collaboration and the kind compliments he has always had for me.

I thank Prof. Stephen Morris and PhD. John Ladan from the University of Toronto, for involving me and Carlo in the interesting and puzzling problem of icicle formation.

I am grateful to Prof. Guido Zolezzi from the University of Trento, for the useful course on river bars I attended in Trento and for the valuable advices he has given us for a model validation.

Last, I wish to thank my parents, who taught me the importance of curiosity, imagination and knowledge. Without them, none of this would have been possible.

Abstract

The interactions between a fluid, such as water or air, and a deformable surface, such as rock, ice or sand, create marvellous natural patterns. The desert dunes generated by the winds, the cave speleothems shaped by thin water films and the sediment patterns on a river bed are just some examples. The branch of fluid mechanics devoted to the study of these patterns is the so-called morphodynamics. In this thesis, some morphological patterns from different natural environments are analytically modelled through stability analysis. This mathematical approach, commonly used to study every morphological pattern, addresses the stability of the spatially uniform solution to a small spatial perturbation. In unstable conditions, the perturbation grows in time to eventually form a finite-amplitude pattern. This thesis focuses on alternate bars, which are macro-scale river patterns, and on some small-scale ice and karst patterns.

In first place, bar formation in rivers with considerable amount of suspended load is investigated. Closed forms relations for the wavelength (linear stability analysis) and the finite amplitude (weakly nonlinear analysis through Center Manifold Projection) are achieved. Results show that suspension plays a destabilizing role in bar instability and it affects both the bar wavelength and amplitude. The theoretical outcomes are validated with field observations. In second place, the conditions for vegetation spreading on finite-amplitude bars are mathematically framed in a model that also includes flow stochasticity. Flow unsteadiness is identified as the main factor discouraging vegetation growth, up to the point that, above a certain threshold, plant spread is completely inhibited. Comparison with field data demonstrates that the model captures the physical conditions heralding the transition between bare and vegetated fluvial states.

Small-scale patterns in karst and glacial environments are usually generated by a falling liquid film. In some cases, the resulting patterns are so similar that a unified approach for the two environments is possible. This happens in the case of the longi-

tudinally oriented organ-pipe-like structures, called flutings, which are widespread in caves and in ice-falls. In this thesis, an analytical model for fluting formation is proposed and closed form relations for the wavelength and the finite-amplitude (linear and weakly nonlinear analyses) are provided. The theoretical results are confirmed by numerical simulations of the fully nonlinear equations.
The last part of this thesis deals with the problem of icicle formation. Recent experiments have revealed that small amounts of dissolved impurities are required for radial ripples to appear on icicle surface. This is contrary to existing theories, which would predict ripples on icicles formed by pure water. The theoretical model here proposed shows that icicles made by pure water do not develop ripples. Moreover, some considerations on the reason why dissolved impurities drive the ripple instability are presented.

Contents

Nomenclature

Greek symbols

α	Floquet coefficient for vegetation growth
β	River aspect ratio
ΔT	Difference in temperature across the liquid film at base state
Δt	Duration of a periodic event
Δ	Relative density
δ	Alternative version of δ'
δ'	Small parameter for the asymptotic approach of ψ
η	Solid-liquid interface
η_d	dune height
γ	Ratio of morphological and hydrodynamic time scales
κ	Von Karman constant
κ_{w}	Temperature diffusivity in water
Λ	Derivative of σ to T
λ_d	dune wavelength
λ_f	Latent heat
λ_p	Sediment porosity

ν	Kinematic viscosity of water
ν_d	Dimensionless decay factor for vegetation
ν_g	Dimensionless growth factor for vegetation
Ω	Eigenvalues for the two-dimensional fluting problem
ω	Complex frequency-Eigenvalue of the linear system
ω_i	Angular phase of the perturbation
ω_r	Growth rate of the perturbation
ϕ	Number of plants per unit area
ψ	Depth-averaged concentration of suspended sediment
ρ	Water density
ρ_I	Ice density
ρ_s	Sediment density
σ	Surface tension
σ_f	Surface tension of pure water at T_f
τ	Bottom shear stress
Θ	Perturbation of η
θ	Shield stress
θ'	Effective Shield stress
Υ	Dimensionless solid discharge
ε	Water film small parameter
ϖ	Coefficient of the diffusive term in the Ginzburg-Landau equation
ρ_c	ratio of molar mass to density of calcite
ς	Slope of the liquidus line

ϑ Angle with the horizontal for the falling liquid film

Ξ Landau coefficient

ξ Coordinate that rectangularizes the domain

ζ Gravitational parameter for the falling liquid film

Latin symbols

$\bar{V}$ Dimensional velocity of the uniform translation of $\hat{\eta}$

$\bar{v}$ Dimensionless velocity of the uniform translation of η

$\mathbf{f}$ Eigenfunctions

$\mathbf{L}_{0,1}$ Linear matrices

$\mathbf{N}(\cdot)$ Second order nonlinearities

$\mathbf{U}$ vector of the state variables

$\mathscr{F}$ Freezing point effect

$\mathscr{H}$ Henry's constant

$\mathscr{L}$ Linear differential operator

$\mathscr{T}$ Integral time scale

$\tilde{K}$ Modulus of the two-dimensional wavenumber

$\tilde{k}$ Wavenumber perpendicular to fluting instability

A_1 Amplitude of the fundamental mode

A_s Pattern finite amplitude

$A_{[m,p]}$ Amplitude of the longitudinal mode p and eigenvalue m

$A_{\frac{1}{2}}$ Amplitude of the first subharmonic

B River half-width

b Assigned depth in the ice

Bi	Biot number
c	Concentration of a dissolved species in the liquid film
C_f	Friction factor
c_v	Variation coefficient
c_v^*	Threshold variation coefficient for plant growth
C_{CO_2}	Concentration of carbon dioxide in air
D	River water depth
d	Sediment particle diameter
D_a	Diffusivity of carbon dioxide in air
D_c	Diffusivity of the dissolved impurities in water
d_s	Relative roughness
D_u	Uniform flow depth
D_{CO2}	Carbon dioxide diffusivity in water
E	Approximation of the invariant manifold
F	Flux of carbon dioxide from the film to the atmosphere
Fr	Froude number
g	Gravitational acceleration
G_i	Coefficients for the CMP
H	Bar height, from through to crest
h	Water film thickness
H_t	Heat transfer coefficient water-air
J	Heat flux flowing through the liquid film
K	Carrying capacity

k	Wavenumber in the direction of the instability
K_I	Thermal conductivity of ice
k_s	Pattern selected wavenumber
K_w	Thermal conductivity of water
$K_{0,1,n}$	Parameters for the evaluation of ψ
Ka	Kapitza number
l_c	Capillary length
l_{opt}	Water table depth maximizing plant growth
M	Marangoni number
m	Integer coefficient for the $m-$eigenvalue (lateral mode in the bar problem)
n	Transversal coordinate in the SWE for rivers
P	Pressure
p	Integer coefficient of the longitudinal mode
P_i	Coefficients for CMP
Pe_c	Peclet number for the dissolved impurities
Pe_T	Peclet number for temperature
Q	Water discharge
q	Flow rate per unit-span
Q^b	Bedload
Q^s	Suspended load
Q_f	Formative water discharge
Q_{max}	Peak water discharge in the periodic event
Q_{min}	Minimum water discharge in the periodic event

R	Generic control parameter
r	Radial distance from the center of the stalactite/icicle
r_ρ	Ratio of ice and water densities
r_c	Ratio between specific heat of water and ice
R_p	Reynolds particle
R_s	Radius of the stalactite/icicle
r_Δ	Ratio of temperature differences in the icicle problem
Re	Reynolds number
Re_t	Transition Reynolds number (discriminating fluting/ripple regimes)
S	River slope
s	Longitudinal coordinate in the SWE for rivers
S_j	Coefficients for CMP
St	Stefan number
T	Temperature
t	Time
t^+	Upcrossing time
T_f	Freezing temperature of pure water
t_s	Saturation time
T_∞	Air temperature
T_b	Temperature at an assigned depth in the ice
U	Depth-averaged longitudinal velocity
u	Water film longitudinal velocity
V	Depth-averaged transversal velocity

v Normal to the base bottom velocity of the falling liquid film

w Transversal velocity of the falling liquid film

We Weber number

x Longitudinal coordinate for the falling liquid film

y Normal to the base bottom coordinate for the falling liquid film

Z Rouse number

z Transversal coordinate for the falling liquid film

Z_i Coefficients for the CMP

Subscripts and superscripts

$\bar{\cdot}$ Averaged variable

$\cdot^*$ Complex conjugate

$\cdot^\dagger$ Adjoint

$\cdot^T$ Transpose

$\cdot_0$ Uniform solution (base state)

$\cdot_1$ Small perturbation of the base state

$\cdot_c$ Critical condition for the instability

$\cdot_I$ Referred to the ice

$\cdot_i$ Imaginary part

$\cdot_K$ Referred to Karst

$\cdot_r$ Real part

$\cdot_w$ Referred to the water

$\cdot^{(1)}$ Order one in series expansions

$\hat{\cdot}$ Dimensional variable

$.^{(0)}$ Order zero in series expansions

Acronyms

AVI Areal Vegetation Index

CMP Center Manifold Projection

CPP Compound Poisson Process

pde Partial differential equation

SWE Shallow Water and Exner equations

Chapter 1

Introduction

1.1 Brief overview on morphodynamics

The beauty and richness of nature have inspired and amused humankind since pre-historical times, when the first groups of men drew animals and landscapes in the caves in which they sheltered. Throughout all human history, the plethora of different natural environments has influenced cultures, arts, scientific discoveries and, more in general, the anthropological evolution of mankind. In the current time, which is now accepted to be called the *Anthropocene*, this influence has somehow reversed and human-activities are strongly impacting Earth's ecosystems worldwide (e.g., Crutzen (2006); Lewis and Maslin (2015); Waters et al. (2016)). Besides the orientation of the nature-humans feedbacks and the ethical questions that may arise, a deeper physical understanding of natural environments remains a crucial challenge for scientists and an opportunity for improvement for every social community.

All natural ecosystems, from the northern glaciers to the tropical forests, from the underground caves to the mountains peaks, from the ocean floors to the sand deserts, are strongly influenced, and partially shaped, by two key natural elements: water and air. Even though water and air are the most common fluids in nature, and also the most important as every living being relies on them to survive, their physical behavior is far to be clear. The reason is that is fluids are composed by microscopic particles that randomly travel in space by subsequent collisions. A slightly different initial condition for just one of the particles may lead to drastic changes in the macroscopic motion of the fluid. This is why weather forecast are so unreliable on

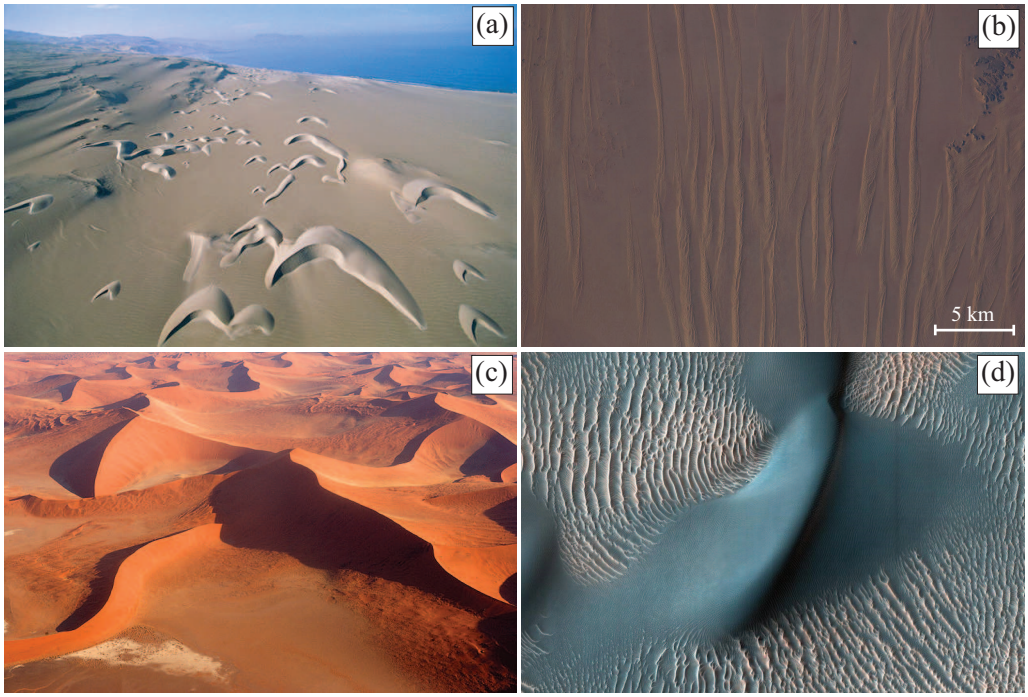

Fig. 1.1 Eolian dunes. (a) Barchan dunes in Paracas National Park, Perù (©George Steinmetz). (b) Transverse dunes in the Great Grand Sea, Egypt (NASA satellite photo). (c) Star dunes in Namibia (©James Parker). (d) Sand patterns on Mars (photo from NASA). The light blue macro-scale pattern is a dune, the smaller scales patterns are ripples.

the long term! This complex behavior of fluids is referred to as *chaos* in the theory of dynamical system (Wiggins, 2003) and as *turbulence* in fluid-mechanics. Although turbulence has been broadly studied in the last centuries from the seminal experiment of Reynolds (1883), it has still many aspects that need to be unveiled (e.g., Pope (2000); Wilcox (1998)).

When a fluid, such as water or air, interacts with a movable solid boundary, such as ice, rock or sand, a further element of complexity is added to the problem. The fluid flow may trigger the transport of sediment particles (e.g., Charru et al. (2013); Lancaster (2013); Seminara (2010)), melting-freezing processes (e.g., Camporeale and Ridolfi (2012a); Chen and Morris (2013)), or the erosion-dissolution of cohesive surfaces (e.g., Dreybrodt (2012); Ford and Williams (2013)), thus modifying the solid boundary. The alteration in the solid boundary affects in turn the fluid flow, triggering a chain of subsequent feedbacks. If these feedbacks are such to annihilate each other (stability), the solid boundary remains flat, on the opposite, if such feedbacks enhance each other (instability), the solid boundary develops into a very ordered wavy pattern.

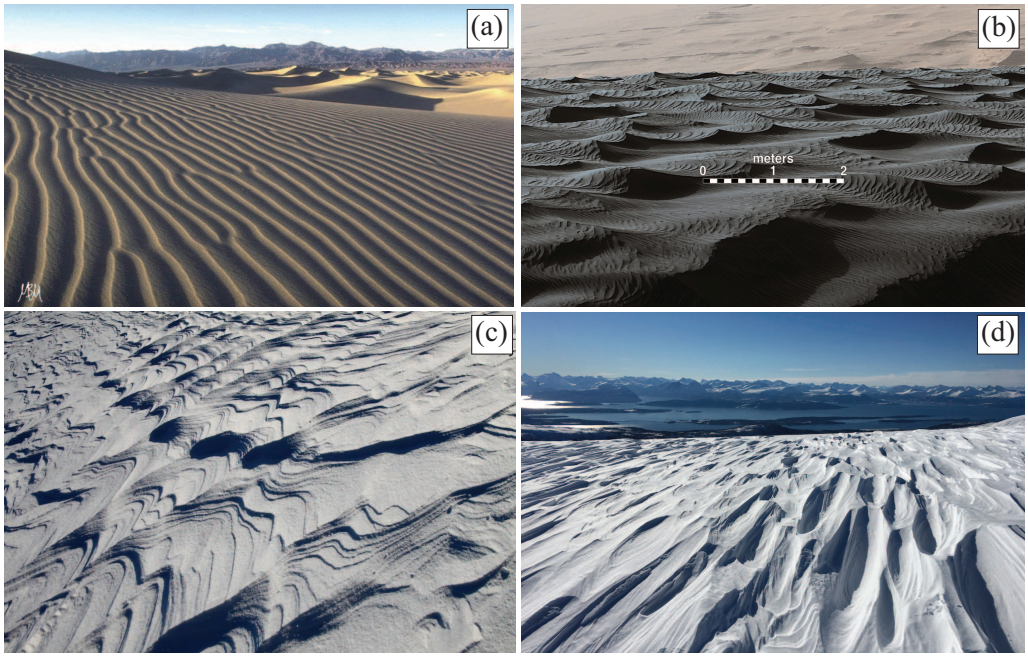

Fig. 1.2 Eolian microscale patterns. (a) Sand ripples in the Death Valley, California. (b) Ripples on Mars (NASA image). (c) Snow ripples in Eldorado Peak, Washington, USA. (d) Sastrugi in Norway.

In nature, there is a multitude of fascinating morphological patterns induced by fluid flows and the branch of fluid mechanics devoted to the study of these patterns is called *morphodynamics*.

Eolian sand dunes in the desert are one of the most renowned example of macroscale morphological pattern. The wind-sediment interactions responsible for dune formation depend on many environmental parameters, such as the wind intensity and direction, the presence of unmovable obstacles and the sediment particle size (e.g., Lancaster (2013); Pye and Tsoar (2008)). Consequently, dunes exhibit various enchanting geometries, e.g., photos of barchan, transverse and star dunes are reported in Fig. 1.1a-c. The research on sand dunes has implications that range from defining the sources of dust storm (Sweeney et al., 2016), to the effect of desertification on anthropic activities (Heshmati and Squires, 2013; Wang et al., 2008), and, exceptionally, to astrophysics. In fact, the dunes spotted on Mars' surface (see Fig. 1.1d) have allowed evaluations on wind regimes (Bridges et al., 2012) and seasonal variability (Ayoub et al., 2014) on the Red Planet.

On smaller scales, wind generates numerous and variegated patterns. Eolian action on non-cohesive sediment leads to the formation of sand ripples (Andreotti

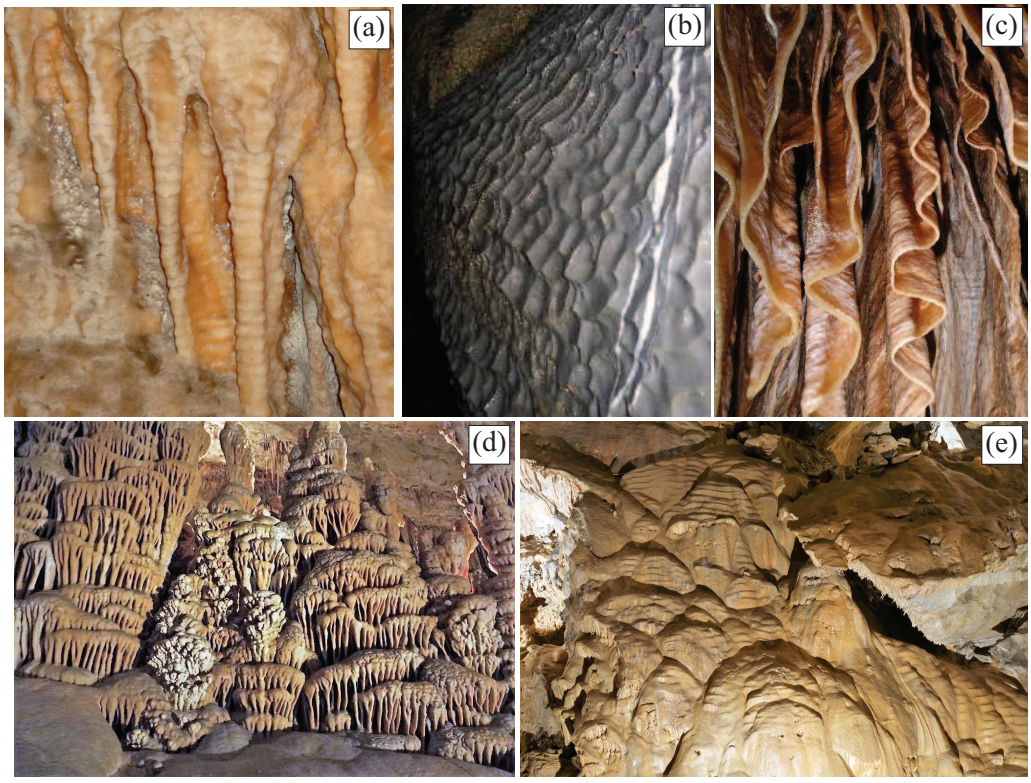

Fig. 1.3 Cave patterns driven by thin water films. (a) Crenulations in the Chifley cave, Australia. (b) Scallops. (c) Meandering draperies (©Dave Bunnel). (d) Cave ripples in the Bossea Cave, Italy (photo courtesy of Bartolomeo Vigna). (e) Flutings on flowstone in Soreq Cave, Israel.

et al. (2006), Fig. 1.2a), which are very common in deserts and coastal beaches, and have also been detected on Mars dunes (Silvestro et al. (2010), Fig. 1.2b). Remarkably similar ripples can be observed on snow surfaces (Filhol and Sturm (2015); Kosugi et al. (1992), Fig. 1.2c). Another ice pattern created by the wind are the sastrugi, or yardangs (Goudie (2007), Fig. 1.2d).

Water is the most important modeller of Earth's surface. From the steep mountain valleys to the flat land, fresh water running downhill develops landforms and sediment patterns through processes of erosion and deposition (Charru et al., 2013; Seminara, 2010). All coasts worldwide are dynamically modelled by the salty water of seas and oceans (Blondeaux, 2001; De Swart and Zimmerman, 2009; Ribas et al., 2015). Underground caves are shaped by aqueous solutions that trigger dissolution and precipitation of cohesive surfaces such as limestone or dolostone (Dreybrodt,

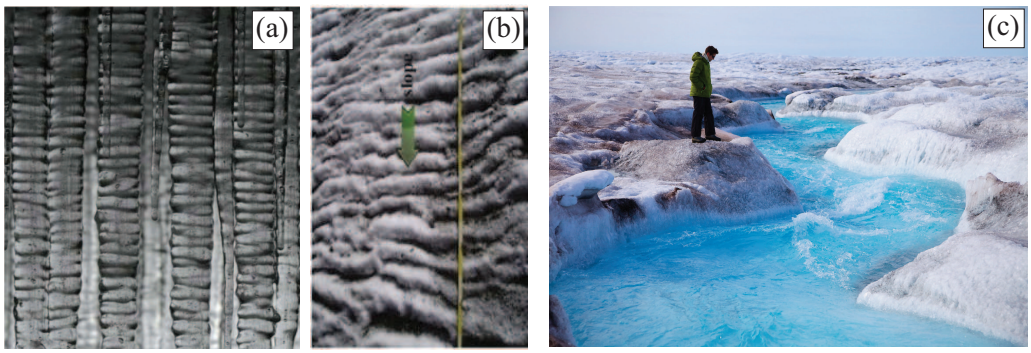

Fig. 1.4 Ice patterns driven by melting water. (a) Ripples on the surface of icicles (Chen and Morris, 2013). (b) Snow ripples on the Chardonney glacier, Italy (Camporeale and Ridolfi, 2012a). (c) Supraglacial channel in Greenland.

2012). Glacier and ice surfaces are carved by melting water through heat transport phenomena (e.g., Camporeale and Ridolfi (2012a); Chen and Morris (2013)).

In caves, precipitation-dissolution processes driven by thin water films (some micrometers thick) shape different types of speleothems, which are karst formations typically generated in limestone or dolostone caves (Meakin and Jamtveit, 2009). Since speleothem morphogenesis can last thousands of years (Proctor et al., 2000), speleothems are silent repositories of past climates and their importance as palaeo-climate proxy is growing among geologists (Baker et al., 1998; Fairchild et al., 2006; McDermott, 2004). Although the hydro-geochemical aspects of cave speleogenesis are well-known (Dreybrodt, 2012; Ford and Williams, 2013), a mathematical approach to the morphodynamic modelling of these water-driven patterns has been introduced only recently. For example, in the case of crenulations, i.e., the sub-centimetre ripples on stalactites surface (Camporeale and Ridolfi (2012b), Fig. 1.3a), scallops (Claudin et al. (2017), Fig. 1.3b) and flutings, the organ-like vertical structures (Camporeale (2015), Fig. 1.3d). Many other speleothems, among which draperies (Martín-Pérez et al. (2012), Fig. 1.3c) and cave ripples (see Fig. 1.3e), still lack a quantitative modelling.

Through a remarkable parallelism, the ice environment is able to generate very similar patterns which are driven by melting-freezing processes, again regulated by the interaction with thin water films. Notice, for example, the analogy between ripples on the surface of icicles (Chen and Morris (2013); Ueno et al. (2009a), Fig. 1.4a) and the crenulations on stalactites (Fig. 1.3a), or the similarity of ice ripples (Camporeale and Ridolfi (2012a); Yokokawa et al. (2016), Fig. 1.4b) with their cave

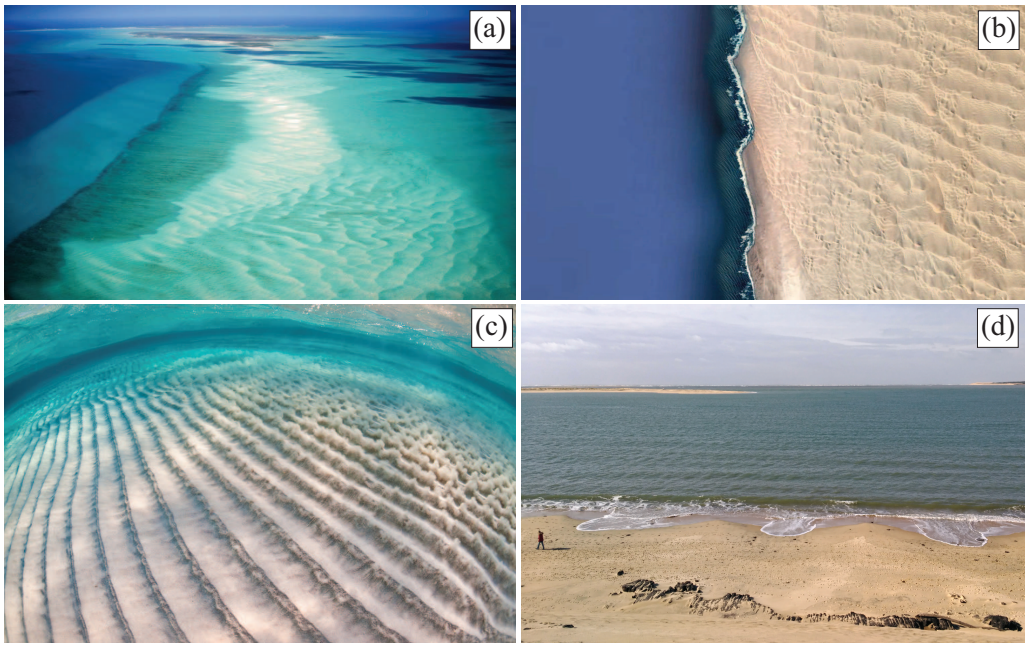

Fig. 1.5 Sea sediment patterns. (a) Pearlescent sand bar in the Caicos Islands, Caribbean Sea. Notice the submerged dunes on the bar. (b) High-angle wave instability in Conception Bay, Namibia. Eolian desert dunes are also present. (c) Sand ripples in the Cayman Islands, Carribean sea. (d) Beach cusps in Arcachon's Bay, France.

counterparts (Fig. 1.3e). At bigger scale, the interaction of turbulent water with ice creates astonishing patterns, as supra-glacial streams (Mantelli et al. (2015); Parker (1975b), Fig.1.4c).

The interaction between water and sediment is the most widespread worldwide, and also the more investigated in the scientific literature (e.g., Blondeaux (2001); Charru et al. (2013); De Swart and Zimmerman (2009); Ribas et al. (2015); Seminara (2010)). Every stream and sea exerts drag forces on the non-cohesive material, such as sand or gravel, whose motion, in turn, alters the water flow. The results are marvellous sediment patterns, which range over many temporal and spatial scales.

In seas and oceans, the flow currents generated by tides or winds drive different phenomena both in the offshore and the nearshore regions (Blondeaux, 2001; De Swart and Zimmerman, 2009; Dronkers, 2005; Ribas et al., 2015). Offshore, common sediment features are sand banks (Huthnance, 1982; Tambroni and Blondeaux, 2008), sand waves (Besio et al., 2006) and sand ridges (Blondeaux et al., 2009), which are, respectively, inclined, perpendicular and parallel to the formative currents. These offshore features are macroscale sediment patterns, with length scales order

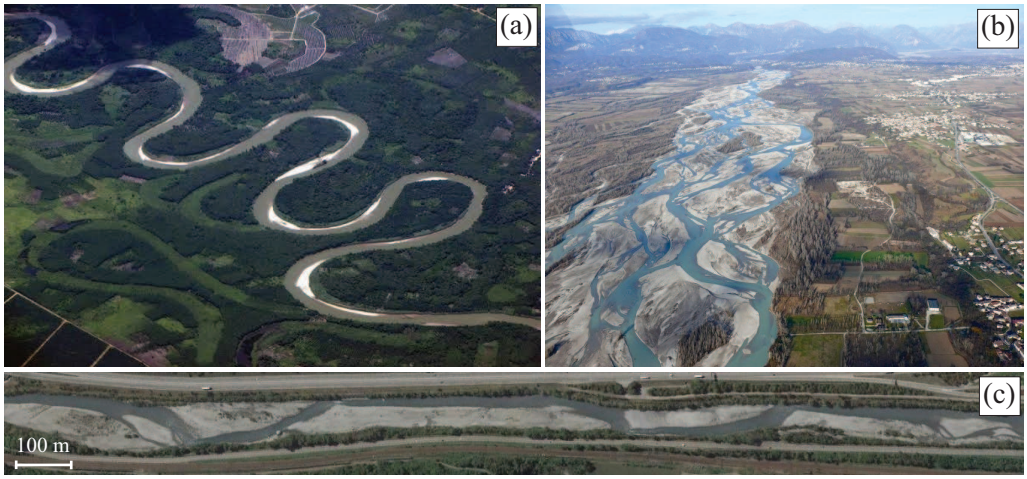

Fig. 1.6 River meso- and large-scale patterns. (a) Meandering river in Turkey. The locations of the cutoff events are recognizable from the green meadows with horse-shoe shape. (b) The Tagliamento River, which is one of the last naturally braided river in Italy (Bertoldi et al., 2009). (c) Alternate bars in the Arc River, France.

of tens of kilometres and time scales order of centuries (van de Meene and van Rijn, 2000). Nearshore, typical morphologies are the bars (Blondeaux (2001); Zhang and Sunamura (1995), Fig. 1.5a) and the high-angle wave instability (Ashton et al. (2001), Fig. 1.5b). On the sandy shorelines, other common patterns are the sand ripples (Blondeaux et al. (2000), Fig. 1.5c) and the beach cusps (Werner and Fink (1993), Fig. 1.5d).

Rivers provide one of the greatest collection of morphodynamic phenomena. River patterns can be classified in small-, meso-, or large-scale depending on their typical wavelengths, scaling with flow depth, channel width, or some larger scale (Seminara, 2010). Patterns of different spatial, and temporal, scales may coexist, but they usually require distinct theoretical tools to be investigated.

River meanders and braided patterns are example of large scale morphologies. Meandering rivers (Fig. 1.6a) can be assimilated to planar curves evolving under two contrastating actions: the continuous elongation induced by the local bed erosion and the sudden and sproadic shortening due to cutoff events (Camporeale et al., 2005; Liverpool and Edwards, 1995). This sequence of elongation and shortening phases is impacted by several external forcings, such as flow variability, riparian vegetation and anthropic actions (Perucca et al., 2007; Visconti et al., 2010).
Braided rivers have complex and astonishingly beautiful geometries (Fig. 1.6b), characterized by sediment islands emerging from a network of water channels. This

complexity causes the stream dynamics to be strongly nonlinear (Murray and Paola, 1994; Parker et al., 2011), especially in the areas of flow bifurcation and merging occurring at the edges of the islands (Federici and Paola, 2003). Moreover, this complexity is also responsible for the richness of different environments in the riverbed, which ranges from the main channel with high flow discharge to the death zones basically at rest (Kemp et al., 2000).

A variety of small-scale patterns arise as instability of the uniform riverbed (Allen, 1982; Seminara, 2010). The mechanism that drives the instability is a phase lag between the bottom perturbation and the sediment flux (Colombini, 2004; Gradowczyk, 1968). This phase lag determines if the perturbation of the riverbed grows or decays in time and if the morphological features travel downstream (e.g., ripples and dunes) or upstream (e.g., antidunes). However, evaluating this phase lag is not an easy task as the sediment interface is affected by many mechanisms such as particle inertia (Parker, 1975a), suspension (Richards, 1980), flow separation (Best, 2005) and particle saltation (Charru et al., 2013). Another element of complexity is that all these small-scale patterns can be two-dimensional, with straight crests, or three-dimensional, with curved crests (Best, 2005; Colombini and Stocchino, 2012).

Bars are the most famous example of meso-scale river patterns (e.g., Bertoldi et al. (2009); Blondeaux and Seminara (1985); Crosato et al. (2012); Siviglia et al. (2013)). They can be classified in free and forced. Free bars grow as an instability of the riverbed to any spatial perturbation and they migrate downstream. Forced bars develop in the presence of a natural or anthropic obstacle, as a meander or a groyne, and they are steady. Moreover, free bars are ulteriorly classified in: alternate bars (Fig. 1.6c), which are a regular sequences of rifles and pools separated by diagonal fronts, and multiple bars in braided rivers (Fig. 1.6b). Alternate free bars have longitudinal scale around ten times the river width, transverse scale constrained by the river width and amplitude with similar scales to the flow depth. Bars are the equilibrium result between secondary flows, which destabilize the flat riverbed, and gravity, which tends to stabilize it (Blondeaux and Seminara, 1985; Federici and Seminara, 2006). This equilibrium is strongly dependent on the channel geometry, so that, as a general rule, narrow channels do not exhibit bars, while alternate and multiple bars appear in wider channels.

In recent years, the morphodynamic field has been extended to include the fundamental role of vegetation in shaping the landscape. This has given rise to the

emerging discipline of *ecomorphodynamics*, in which vegetation is not only seen as a passive element affecting fluid flow and sediment transport (Baptist et al., 2007; Rominger et al., 2010), but also as an active element within the whole dynamics (Bennett and Simon, 2004). In ecomorphodynamics research, fluid flow, sediment transport and vegetation dynamics are the three fundamental elements that interact through a chain of complex feedbacks on different spatial and temporal scales (Camporeale et al., 2013; Vesipa et al., 2017). These interactions determine the morphodynamics of rivers (Bertoldi et al., 2014; Siviglia and Crosato, 2016) and, for example, the shape of aeolian dunes in coastal and semi-arid regions (Kutiel et al., 2004; Nield and Baas, 2008). In rivers, riparian and riverbed vegetation affects the flow field (Bennett et al., 2008) and the processes of sediment transport and deposition (Ishikawa et al., 2003). Moreover, plants act as chemical filters improving the water quality (Dosskey et al., 2010) and plant roots affect the mechanical and hydraulic soil properties, stabilizing landforms and river banks (Gyssels et al., 2005). On the other hand, fluid dynamics controls vegetation growth through seed dispersal (Merritt and Wohl, 2002), provision of water and nutrients (Sabater et al., 2000), uprooting by erosion (Edmaier et al., 2011) and creation of new depositional sites for plant colonization (Stella et al., 2013). Furthermore, the water regimes can influence root architecture (Pasquale et al., 2012), which is determinant for the survival of pioneering vegetation (Perona et al., 2012). The research on these complex interactions and feedbacks involves multidisciplinary knowledge from hydrology, hydraulic, geomorphology and ecology and, due to the broad applications, it is attracting an increasing number of scientists (see Vesipa et al. (2017) for a recent review).

1.2 The mathematical approach to morphological instabilities

The governing equations for morphological systems are partial differential equations (pdes) arising from physical conservation laws: the Navier-Stokes equations for the fluid dynamics and an evolution equation for the solid boundary. The generic system of pdes reads

$$\partial_t \mathbf{U} = \mathbf{G}(\mathbf{U}, \partial_{\mathbf{x}}\mathbf{U}, \partial_{\mathbf{xx}}\mathbf{U}...R), \tag{1.1}$$

where $\mathbf{U}$ is the vector of the state variables, $\mathbf{x}$ is the vector of spatial coordinates, t is time and R is a generic *control parameter*, which depends on the environment considered. From the system of pdes (1.1), to theoretically extract reliable informations is not an easy task (Charru, 2011; Cross and Hohenberg, 1993). The common analytical approach to study morphodynamic patterns is the so-called *stability analysis*, which addresses the stability of the steady and spatially uniform solution $\mathbf{U}_0$ ($\partial_t \mathbf{U}_0 = 0$) to small perturbations.

As a physical example, we can imagine the spatially uniform solution $\mathbf{U}_0$ as a completely flat riverbed made of sand particles (ideally neglecting the sand roughness). If the water flow is sufficiently strong, a sand particle can be dragged and transported above another sand particle, thus introducing a small spatial perturbation in the riverbed. This spatial irregularity of the riverbed affects in turn the water flow, that might enhance the accumulation (excavation) of sand particles on the crest (through) of the riverbed perturbation. If this happens, the uniform solution (the flat riverbed) is said to be *unstable*, the perturbation grows in time and the non-equilibrium spatial pattern develops (see Figures 1.1-1.6).

Mathematically, the vector of the state variables is recast as the sum of the uniform steady solution $\mathbf{U}_0$ and a small perturbation $\mathbf{U}_1$, as follows

$$\mathbf{U} = \mathbf{U}_0 + \mathbf{U}_1. \tag{1.2}$$

By substituting (1.2) in (1.3) and truncating to quadratic nonlinearities, one obtains the weakly nonlinear system for the perturbation

$$\partial_t \mathbf{U}_1 = \mathbf{L}\,\mathbf{U}_1 + \mathbf{N}(\mathbf{U}_1) + O(\mathbf{U}_1^3), \tag{1.3}$$

in which $\mathbf{L}$ is the linear matrix and $\mathbf{N}(\mathbf{U}_1)$ contains all second order nonlinearities.

At this point, it is convenient to write the small perturbation in the Fourier space,

$$\mathbf{U}_1 \propto A(t) \mathrm{e}^{\mathrm{i}\mathbf{k}\mathbf{x}}, \tag{1.4}$$

where $\mathbf{k}$ is the wavenumber, which for morphological instabilities is usually one- or two-dimensional, and $A(t)$ is the complex amplitude of the perturbation. In pattern formation, a good approximation of the amplitude dynamics in time is given by the

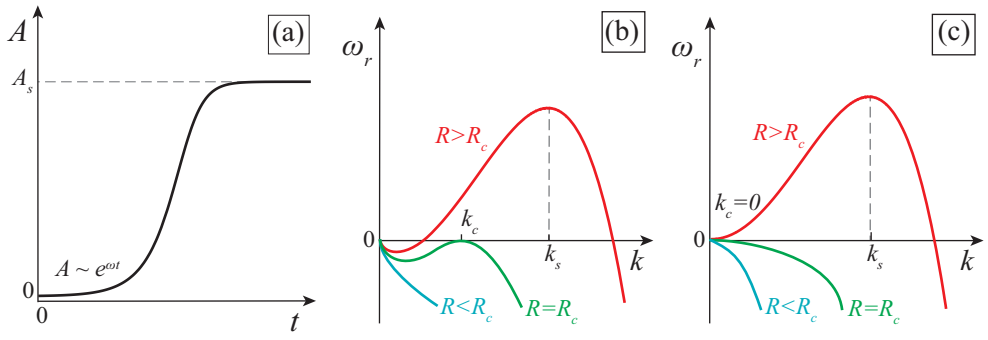

Fig. 1.7 Generic results from the stability analysis. (a) Amplitude dynamics in time as described by the Stuart-Landau eq. (1.5). (b-c) Behaviour of the growth rate versus the wavenumber in stable (light blue), neutral (green) and unstable (red) conditions. Instabilities of type I (panel b) and II (panel c) in the classification of Cross and Hohenberg (1993).

Stuart-Landau equation

$$\partial_t A = \omega A + \Xi |A|^2 A. \tag{1.5}$$

A graphical example of the amplitude dynamics, as described by the Stuart-Landau equation (1.5), is given in Fig. 1.7a.

1.2.1 Linear analysis

When A is very small, the nonlinear term in (1.5) is negligible and the amplitude essentially grows exponentially $A \propto e^{\omega t}$. Analogously, $\mathbf{N}(\mathbf{U}_1)$ can be neglected in the system (1.3), which reduces to

$$(\mathbf{L} - \omega \mathbf{I})\,\mathbf{U}_1 = 0, \tag{1.6}$$

where $\mathbf{I}$ is the identity matrix. Imposing $|\,(\mathbf{L} - \omega \mathbf{I})\,| = 0$, one obtains the dispersion relation

$$f(\omega, \mathbf{k}, R) = 0. \tag{1.7}$$

The dispersion relation (1.7) links the wavenumber $\mathbf{k}$ and the control parameter R to the complex frequency ω, whose real part determines the growth rate of the perturbation. If $\omega_r > 0$, the perturbation grows in time to form the morphological pattern. The dispersion relation (1.7) usually reveals that the instability develops when the system is brought away from equilibrium by increasing R. When $R >$

R_c, where R_c is the threshold *critical* value, the system is unstable to a band of infinitesimal perturbations. Among these perturbations, the one that grows faster, determines the pattern wavenumber k_s . In Fig. 1.7 b-c, typical behaviors of the growth rate ω_r versus the wavenumber k are reported. The difference in the two panels regards the critical wavenumber k_c. In the first case (panel b), k_c has a finite value and there is a range of unstable wavenumber that does not span from zero, as it happens for example in river bar instability (Blondeaux and Seminara, 1985). This is the type I instability in the classification suggested by Cross and Hohenberg (1993). In the second case (panel c), $k_c = 0$ and the range of unstable wavenumbers spans from zero. This means that the low modes and the subharmonics of the fundamental k_s are linearly unstable and may destabilse the growth of the fundamental (Cheng and Chang, 1990, 1992). This is the type II instability in the classification suggested by Cross and Hohenberg (1993) and is the common instability in problems with thin liquid films (Craster and Matar, 2009; Kalliadasis et al., 2011). Notice that, in both cases, $\omega_r = 0$ for $k = 0$ because the system (1.1) arises from physical laws of conservation (the Navier-Stokes equation).

1.2.2 Weakly nonlinear analysis

When A is no longer infinitesimal, nonlinear effects became predominant and dampen the perturbation growth expected by the linear theory. To evaluate the nonlinear effects, one needs to solve the weakly nonlinear system (1.3). In the study of morphological instabilities, the classical analytical approach to do so has always been the multiple-scaling (e.g., Colombini et al. (1987); Ji and Mendoza (1997); Tambroni and Blondeaux (2008); Vittori and Blondeaux (1990)). Instead, in this thesis, we have performed the weakly nonlinear analyses through the mathematichal technique of Center Manifold Projection (CMP, Fujimura (1997); Guckenheimer and Holmes (2013); Wiggins (2003)). This represents a novelty in the morphodynamics field. The advantages of CMP with respect to multiscale theories are mainly two: i) CMP is a more rigorous and simplified tool; ii) CMP furnishes an amplitude equation that is not constrained around the critical point (Carr and Muncaster, 1983; Chang, 1994). The main result obtained through CMP is the Landau coefficient Ξ for eq. (1.5). If $\Xi_r < 0$, the amplitude of the perturbation reaches a finite-value A_s (as shown

in Fig. 1.7a), which reads

$$A_s = \sqrt{-\frac{\Xi_r}{\omega_r}}. \tag{1.8}$$

Alternatively, if $\Xi_r > 0$, two possibilities arise: i) the nonlinearities that dampen the growth are higher order, so that a quintic Stuart-Landau equation is needed (Fujimura, 1997) ii) the pattern does not saturate to a finite amplitude (as meanders in rivers). Beyond the finite amplitude A_s, the weakly nonlinear analysis through CMP allows to evaluate the influence that some modes, as the side-bands or the subharmonics, have on the dynamics of the fundamental (Cheng and Chang, 1990, 1992). For example, the sideband stability analysis (Lin, 1974) determines the stability of the finite-amplitude monochromatic fundamental to perturbations of sideband wavenumbers. In multiscale theory, a similar result can be obtained by using the Ginzburg-Landau equation instead of the Stuart-Landau equation (1.5). The Ginzburg-Landau equation reads

$$\partial_t A = \omega A + \Xi |A|^2 A + \varpi \frac{\partial^2 A}{\partial X^2}, \tag{1.9}$$

where the additional diffusive term ($\varpi\, \partial^2 A/\partial X^2$) introduces a spatial modulation in the monochromatic finite-amplitude pattern. However, equation (1.9) is valid only in a neighbourhood of the critical point, when the tangency condition $(\partial \omega_r/\partial k)_c = 0$ is satisfied. Such condition is not satisfied when the weakly nonlinear analysis is performed around a generic point of the neutral stability curve instead of the critical point, so when CMP is used. Furthermore, the Ginzburg-Landau equation is erroneous for the type II instability (Fig. (1.7)c), as also in this case the nonlinear analysis is performed around the neutral curve and not the critical point (basically because $R_c = k_c = 0$, Chang (1994)). The sideband stability analysis through CMP generalizes the validity of (1.9). Moreover, the use of CMP in the sideband analysis provides more reliable results as it also includes the effects of the low modes ($k \sim 0$) in the instability of the fundamental (Cheng and Chang, 1990).

1.3 Thesis contents

This thesis is divided in two parts:

1. Part I, composed of Chapter 2 and 3, regards the river environment with focus on alternate bars (Fig. 1.6c).
   In Chapter 2, alternate bar formation is investigated through linear and weakly nonlinear analyses, including the effect of suspended load. The theoretical bar wavelength and amplitude are consequently verified with field observations.
   In Chapter 3, the possibility for vegetation to spread on alternate bar crests depending on flow variability is analytically examined. This latter Chapter describes a theory in which, for the first time, the three main cornerstone of the emerging discipline of ecomorphodynamics (sediment transport, flow stochasticity and vegetation dynamics) are linked in a whole. Also in this case, the theory predictions are satisfactorily verified with field observations.

2. Part II, composed of Chapter 4 and 5, regards the cave and glacial environments, with focus on patterns shaped by thin water films.
   In Chapter 4, fluting formation (Fig. 1.3d) is analytically investigated through linear and weakly nonlinear analyses. The analytical results are validated through numerical simulations.
   In Chapter 5, we introduce a preliminary model, based on experimental evidences, for the morphological evolution of the icicle surface (Fig. 1.4a).

The content of Chapter 3 has been developed in collaboration with the University of Edinburgh (Prof. Paolo Perona). The model in Chapter 5 originates from a collaboration with the University of Toronto (Prof. Stephen Morris and PhD. John Ladan).

1.4 Novel contributions and publications

Parts of this work are discussed in the following publications:

1. Bertagni, M. B., & Camporeale, C. (2018). Finite amplitude of free alternate bars with suspended load. Water Resources Research (Chapter 2)

2. Bertagni, M. B., Perona, P., & Camporeale, C. (2018). Parametric transitions between bare and vegetated states in water-driven patterns. Proceedings of the National Academy of Sciences, 115(32), 8125-8130 (Chapter 3)

3. Bertagni, M. B., & Camporeale, C. (2017). Nonlinear and subharmonic stability analysis in film-driven morphological patterns. Physical Review E, 96(5), 053115 (Chapter 4)

Chapter 5 will form the basis for another journal publication.

Part I: Alternate bars in rivers

Bars constitute the most important fluvial pattern, strongly influencing water flow and any anthropogenic or natural activity in a river. Bars are the key elements that trigger the meandering (Parker, 1976) and they cause localised erosion of river banks (Visconti et al., 2010). Moreover, bars limit the navigability of river channels and can play a fundamental role in river renaturalization by increasing the bed channel area and favoring biodiversity (Gilvear and Willby, 2006). For these reasons, river bars have been studied extensively over the last decades through field observations (Bertoldi et al., 2009; Eekhout et al., 2013), experiments (Crosato et al., 2012; Lanzoni, 2000), numerical simulations (Defina, 2003; Siviglia et al., 2013) and analytical modelling (Blondeaux and Seminara, 1985; Colombini et al., 1987; Schielen et al., 1993).

From classical theoretical investigations of shallow water equations coupled with 2D sediment transport conservation (Exner equation), it is known that a base plane bed becomes unstable when the aspect ratio β, which is the ratio between the half channel width and the uniform flow depth, exceeds a critical value ($\beta > \beta_c$) (Blondeaux and Seminara, 1985). In such unstable conditions, any infinitesimal spatial perturbation is able to trigger the development of the bar pattern. Bars have been modeled, through this instability approach, by means of linear and weakly nonlinear analyses (Blondeaux and Seminara, 1985; Callander, 1969; Colombini et al., 1987; Parker, 1976; Schielen et al., 1993). In two noticeable works, the effect of flow unsteadiness has been included (Hall, 2004; Tubino, 1991).

In the next two Chapters, we extend the research on alternate bars by addressing two open issues:

1. the inclusion of suspended load in alternate bar modeling, with focus on alternate bar finite amplitude (Chapter 2),

2. the possibility for vegetation to spread on bar crests depending on flow variability (Chapter 3).

Chapter 2

Finite amplitude of free alternate bars with suspended load

2.1 Introduction

The work described in this chapter has been partially derived from Bertagni and Camporeale (2018).
The main geometrical features of alternate bars (wavelength and amplitude) depend on the mutual interactions between hydrodynamics and sediment transport. Regarding sediment transport, most of the research in the last decades (e.g., Colombini et al. (1987); Schielen et al. (1993)) has focused only on the role of bedload, neglecting suspended load. This approximation is satisfactory for the standard conditions in gravel-bed rivers, but it is not adequate for a correct morphodynamic modelling of those river with very fine sediment.

The problem of coupling bar formation with suspended sediment was first addressed by Tubino et al. (1999), through a three-dimensional approach. The authors showed that suspension has a strong quantitative effect on bar instability as it reduces β_c (i.e., the critical aspect ratio) and leads to longer wavelengths at criticality. However, the linear stability analysis was solved numerically, thus limiting the possibility of additional analytical studies. A further advancement was made by Bolla Pittaluga and Seminara (2003), who revisited some previously formally incorrect asymptotic approaches and demonstrated the validity of a depth-averaged river modeling even in the presence of suspension. The main assumption is that advective and

unsteady effects are smaller than gravitational settling and turbulent diffusion. Bars instability was linearly and analytically investigated through this approach (Federici and Seminara, 2006), and the semi-analytical results of Tubino et al. (1999) were confirmed.

The main task of the present Chapter is to provide an analytical tool able to compute the amplitude of alternate bars in presence of suspended load. To this aim, the model of Federici and Seminara (2006) and the weakly nonlinear technique of Center Manifold Projection (CMP) are adopted. This technique is based on the assumption that the stable modes have fast dynamics, which can be projected onto the slow dynamics of the quasi-neutral or weakly unstable mode (the alternate bar mode). Eventually, a differential equation with closed-form coefficients is obtained, i.e., the well-known Stuart-Landau equation, in which only the bar amplitude is involved. Such an equation quantifies the nonlinear terms that dampen the exponential growth that can be expected from the linear theory, and its stationary solution results to be the finite amplitude A_s of alternate bars.

Validation of the analytical results has been performed considering field observations of alternate sandy bars available in literature. In particular, bathymetry data from the Mississippi river (Ramirez and Allison, 2013) and a straight artificial channel in the Netherlands (Eekhout et al., 2013) have been used. In addition, some speculative considerations have been made pertaining to partial data on the Yellow River in China (Ma et al., 2017).

This chapter is structured as follows: the mathematical framework is presented in Sec. 2.2, together with the linear and the nonlinear analyses that lead to the Stuart-Landau equation; the outcomes of the analytical theory are verified and discussed with field data in Sec. 2.3; some concluding considerations are given in Sec. 2.4.

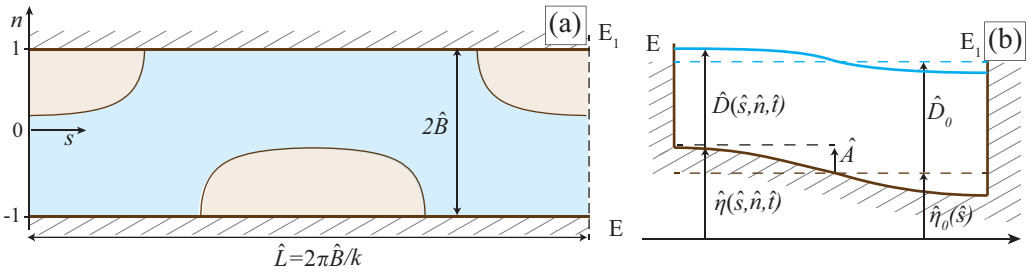

Fig. 2.1 Graphic framework. (a-b) Aerial sketch and channel section. The superscript hat refers to dimensional quantities and $\hat{A}$ is the amplitude of the bar, i.e., the height of the bar crest with respect to the flat bottom condition.

2.2 Mathematical model

2.2.1 Dimensionless Shallow Water and Exner equations

Dimensionless Exner and shallow water equations under quasi-steady approximation (i.e., the flow adapts instantaneously to variations in the bed height) read as:

$$U\partial_s U + V\partial_n U + Fr^{-2}\partial_s(D+\eta) + \beta D^{-1}\tau_s = 0, \tag{2.1}$$

$$U\partial_s V + U\partial_n V + Fr^{-2}\partial_n(D+\eta) + \beta D^{-1}\tau_n = 0, \tag{2.2}$$

$$\partial_s(UD) + \partial_n(VD) = 0, \tag{2.3}$$

$$-\Upsilon\left(\partial_s Q_s^b + \partial_n Q_n^b\right) - \partial_s Q_s^s - \partial_n Q_n^s = \partial_t \eta, \tag{2.4}$$

with boundary conditions that impose a vanishing transversal flux of water and sediment at the river banks

$$V = Q_n^{b,s} = 0, \qquad (n = \pm 1). \tag{2.5}$$

In the system (2.1)-(2.5), s and n are the longitudinal and transversal coordinates, see Fig. 2.1; U and V are the longitudinal and transversal depth-averaged velocities; D and η are the water depth and bottom height; ∂ refers to partial derivative; τ_s and τ_n are the two components of the bottom shear stress; Q_s^b and Q_n^b are the two components of the bedload solid discharge; Q_s^s and Q_n^s refer to the suspended solid discharge. Note that eqs. (2.1)-(2.5) have been made dimensionless through the

following scaling:

$$\begin{aligned}
(s,n) &= (\hat{s},\hat{n})/\hat{B}, & (U,V) &= (\hat{U},\hat{V})/\hat{U}_0,\\
(D,\eta) &= (\hat{D},\hat{\eta})/\hat{D}_0, & t &= \hat{t}\,\hat{U}_0/\hat{B},\\
(Q_s^b,Q_n^b) &= (\hat{Q}_s^b,\hat{Q}_n^b)/\sqrt{\Delta g\hat{d}^3}, & (Q_s^s,Q_n^s) &= (\hat{Q}_s^s,\hat{Q}_n^s)/(\hat{U}_0\hat{D}_0),\\
(\tau_s,\tau_n) &= (\hat{\tau}_s,\hat{\tau}_n)/(\rho\hat{U}_0^2)
\end{aligned} \tag{2.6}$$

where the hat refers to dimensional quantities, $\hat{B}$ is the channel half width, $\hat{D}_0$ and $\hat{U}_0$ are the uniform flow depth and velocity, $\hat{d}$ is the sediment particle diameter (granulometry is assumed uniform), ρ the water density, g the gravitational acceleration and $\Delta=(\rho_s-\rho)/\rho\sim 1.65$ with ρ_s the sediment density. The dimensionless parameters appearing in eqs. (2.1)-(2.5) are

$$Fr=\frac{\hat{U}_0}{\sqrt{g\hat{D}_0}}, \qquad \Upsilon=\frac{\sqrt{\Delta g\hat{d}^3}}{(1-\lambda_p)\hat{D}_0\hat{U}_0}, \qquad \beta=\frac{\hat{B}}{\hat{D}_0}, \tag{2.7}$$

where Fr is the Froude number; Υ is the dimensionless solid discharge; λ_p is the porosity of the granular medium (around 0.3 for sand mixtures); and β is the aspect ratio, which is the main parameter controlling bar instability. The closure relationships for shear stress τ and bedload Q^b, which depend on the relative roughness $d_s=\hat{d}/\hat{D}_0$, are reported in Appendix A.1.

2.2.2 Inclusion of suspended load

Suspended load is accounted for in eq. (2.4) through the asymptotic approach derived by Bolla Pittaluga and Seminara (2003) and successively adopted by Federici and Seminara (2006) for the linear analysis of bar instability. Such an approach is based on an asymptotic expansion of the exact solution of the advection-diffusion equation for the sediment concentration, under the hypothesis that the flow is slowly varying. Here the approach is briefly summarized. The dimensional advection-diffusion equation for suspended sediment reads

$$\partial_{\hat{t}}C+\hat{U}\partial_{\hat{s}}C+\hat{V}\partial_{\hat{n}}C+(\hat{W}-\hat{W}_s)\partial_{\hat{z}}C=\hat{D}_z\partial_{\hat{z}\hat{z}}C, \tag{2.8}$$

where $\hat{z}$ and $\hat{W}$ are the dimensional vertical coordinate and velocity, and $\hat{W}_s$ is the settling velocity of a sediment particle (see Appendix A.2.1. Only the the vertical eddy diffusivity $\hat{D}_z$ has been retained in eq. (2.8), as transversal and longitudinal eddy diffusions provide a negligible contribution. The variables are scaled as follows

$$(s,n) = (\hat{s},\hat{n})/\hat{L}, \qquad (U,V) = (\hat{U},\hat{V})/\hat{U}_0, \qquad W = \frac{\hat{W}\hat{B}}{\hat{D}_0\hat{U}_0}, \tag{2.9}$$
$$(D,z) = (\hat{D},\hat{z})/\hat{D}_0, \qquad t = \hat{t}\,\hat{U}_0/\hat{L}, \qquad D_z = \frac{\hat{D}_z}{\hat{u}_*\hat{D}_0},$$

where $\hat{u}_*$ is the friction velocity and $\hat{L}$ is the scale of the longitudinal variation of the flow field, which in our problem is the bar wavelength. Using the scaling (2.9), the advection-diffusion equation (2.8) reduces to

$$\delta'(\partial_t C + U\partial_s C + V\partial_n C + \partial_z C) = \partial_z C + \frac{1}{\kappa Z}\partial_{zz} C, \tag{2.10}$$

where

$$\delta' = \frac{\hat{U}_0\hat{D}_0}{\hat{W}_s\hat{L}}, \tag{2.11}$$

and $\kappa Z = \hat{W}_s/\hat{u}_*$, being κ and Z the von Karman constant and the Rouse number respectively. Notice that the parameter δ' is a small quantity for slowly varying flows (Bolla Pittaluga and Seminara, 2003). This physically means that advective and unsteady effects, l.h.s. of eq. (2.10), are smaller than gravitational settling and turbulent diffusion, r.h.s. of eq. (2.10). Carrying out the expansion $C = C^{(0)} + \delta' C_1^{(1)}$, the leading order problem reads

$$\partial_z C^{(0)} + \frac{1}{\kappa Z}\partial_{zz} C^{(1)} = 0. \tag{2.12}$$

Eq. (2.12), coupled to a boundary condition of no flux of sediment in the air and to an assumption of particle entrainment on the riverbed, yields the classical Rouse profile for $C^{(0)}$. The order δ' problem reads

$$\partial_t C^{(0)} + U\partial_s C^{(0)} + V\partial_n C^{(0)} + \partial_z C^{(0)} = \partial_z C^{(1)} + \frac{1}{\kappa Z}\partial_{zz} C^{(1)}, \tag{2.13}$$

whose solution $C^{(1)}$ accounts for the non-equilibrium effect induced by spatial and temporal variations of the flow field. Depth-averaging $C = C^{(0)} + \delta' C_1^{(1)}$, one obtains

the depth-averaged concentration $\psi = \psi^{(0)} + \delta' \psi_1^{(1)}$. Through some mathematical manipulation, Bolla Pittaluga and Seminara (2003) found

$$\psi^{(0)} = \frac{\bar{\psi}_0 K_0}{1-\lambda_p}, \qquad \psi^{(1)} = \frac{K_1 D(U\partial_s \bar{\psi}_0 + V\partial_n \bar{\psi}_0)}{1-\lambda_p}, \tag{2.14}$$

where $\bar{\psi}_0$ is the depth-averaged concentration of the Rouse profile, while $K_{0,1}$ are functions of the relevant physical parameters (see Appendix A.2.2). The function K_1 had previously been obtained numerically (Bolla Pittaluga and Seminara, 2003; Federici and Seminara, 2006), while here a completely analytical solution has been adopted (see Appendix A.2.3 for further details).

In the bar formation problem, to avoid δ' to depend on the a-priori unknown bar wavelength $\hat{L}$, is convenient to use $\hat{B}$ as a longitudinal scale (Federici and Seminara, 2006). This gives a slightly different parameter δ,

$$\delta = \delta' \frac{\hat{L}}{\hat{B}} = \frac{\hat{U}_0}{\hat{W}_s} \frac{1}{\beta}, \tag{2.15}$$

that is formally assumed to be small. In order to assure validity of the approach, the parameter δ' has to be necessarily small (i.e., $\delta \ll \hat{L}/\hat{B}$).

Finally, the suspended load, with the dimensionless depth-averaged concentration ψ reads

$$(Q_s^s, Q_n^s) = D\,(U,V)\,(\psi^{(0)} + \delta\,\psi^{(1)} + O(\delta^2)). \tag{2.16}$$

Notice that, to address the closure relationships for suspended load, the Reynolds particle R_p needs to be introduced

$$R_p = \frac{\sqrt{\Delta g \hat{d}^3}}{\nu}, \tag{2.17}$$

where ν is the kinematic viscosity of water.

2.2.3 Stability analysis

Free alternate bars develop as an instability of the uniform flow solution to an infinitesimal perturbation. Hence, the vector of the state variables $\mathbf{U} = (U, V, D, \eta)$ is

recast as the sum of the base state $\mathbf{U}_0$ and a small perturbation $\mathbf{U}_1$ as follows:

$$\mathbf{U} = \mathbf{U}_0 + \mathbf{U}_1 = (1,0,1,\eta_0(s)) + (U_1, V_1, D_1, \Theta_1), \tag{2.18}$$

where $\eta_0 = -S\beta\, s$ is the bed height at the base state, S is the river slope and Θ_1 is the bed height perturbation. By substituting (2.18) in the system (2.1)-(2.4) and truncating to quadratic nonlinearities, one obtains:

$$\mathbf{L}_0\, \partial_t \mathbf{U}_1 = \mathscr{L}_1 \mathbf{U}_1 + \mathbf{N}(\mathbf{U}_1) + O(\mathbf{U}_1^3), \tag{2.19}$$

where $\mathscr{L}_1$ is a linear differential operator; $\mathbf{L}_0$ is a matrix with null elements except for the lower-right entry, which is 1; and $\mathbf{N}(\mathbf{U}_1)$ contains all the second order nonlinearities. Notice that $\mathbf{L}_0$ arises from the quasi-steady approximation, i.e., the fact that the only time derivative in the system (2.1)-(2.4) is the one for η. The Center Manifold Projection technique requires the unknown $\mathbf{U}_1$ to be further expanded in terms of the $\mathbf{f}_m$ eigenfunctions through the following ansatz

$$\mathbf{U}_1(s,n,t) = \sum_{p=-n_p}^{n_p} \sum_{m=1}^{n_m} A_{[m,p]}(t)\, \mathbf{f}_m(pk,n) \mathrm{e}^{\mathrm{i}pks}, \tag{2.20}$$

where k is the longitudinal wavenumber and $A_{[m,p]}(t)$ is the generic amplitude of the longitudinal mode p and lateral mode m. Such an expansion takes on slightly different meaning for linear and nonlinear analyses, as explained hereafter.

2.2.4 Linear order

A linear analysis of the system (2.19) has already been investigated by Federici and Seminara (2006) with the closure relationship for suspended load provided by Bolla Pittaluga and Seminara (2003), thus it is only briefly reported here. In general, linear analyses rely on the hypothesis that perturbations of different modes are infinitesimally small, decoupled and grow/decay exponentially in time. Therefore, if reference is made to the expansion (2.20), the only longitudinal harmonic of interest is the fundamental one ($p = 1$). Each transversal harmonic m leads to a decoupled problem ($m = 1$ is an alternate bar mode, $m = 2$ is a central bar mode) and the amplitudes read $A_{[m,p]}(t) \sim \mathrm{e}^{\omega_m t}$, where ω_m is a complex number, whose real and imaginary parts determine the growth rate and the angular phase. In order to satisfy

the boundary conditions (2.5), the $\mathbf{f}_m$ eigenfunctions are written as:

$$\mathbf{f}_m = \begin{cases} \left(u_m, v_m \cot\left(\frac{m\pi}{2}n\right), d_m, \eta_m\right) \sin\left(\frac{m\pi}{2}n\right) + c.c., & (m \text{ odd}), \\ \left(u_m, v_m \tan\left(\frac{m\pi}{2}n\right), d_m, \eta_m\right) \cos\left(\frac{m\pi}{2}n\right) + c.c., & (m \text{ even}), \end{cases} \tag{2.21}$$

where $c.c.$ means complex conjugate. If the closure relationships for suspended sediment (2.14) are expanded in the perturbations of the state variables, one obtains:

$$\psi^{(0)} = \psi_0^{(0)}(1 + t_1 U_1 + t_2 D_1), \tag{2.22}$$

$$\psi^{(1)} = K_n \left(t_3 \partial_s U_1 + t_4 \partial_s D_1\right), \tag{2.23}$$

with $\psi_0^{(0)}$ and K_n defined as in Appendix A.2.2, while t_{1-4} are the same as Federici and Seminara (2006). Moreover, τ_s, τ_n, Q_s^b, Q_n^b are written as a first-order Taylor expansion of the state variable perturbation, as reported in Colombini et al. (1987). By substituting (2.21)-(2.23) in the system (2.19) and linearizing (i.e., neglecting $\mathbf{N}$), one obtains:

$$\left(\mathbf{L}_0 \omega_m - \mathbf{L}_1^m\right) \mathbf{f}_m = 0, \tag{2.24}$$

where the algebraic matrix $\mathbf{L}_1^m$ is reported in Appendix A.3. After imposing $|(\mathbf{L}_0 \omega_m - \mathbf{L}_1^m)| = 0$, the dispersion relation, and consequently the ω_m eigenvalue, are obtained. The analytical expression for ω_m is reported in Appendix A.3. It should be noted that, unlike Federici and Seminara (2006), we have not expanded the perturbations (2.20) in the δ parameter, but we have instead solved the linearized problem directly.

The neutral condition for alternate bar formation is defined as the solution to the dispersion relation that satisfies $\omega_{1,r} = 0$, where $\omega_{1,r}$ is the growth rate for alternate bars (the subscript r refers to the real part). This condition manifests as a *marginal* curve in the (k,β) plane, with a minimum at the critical point (k_c,β_c). In Fig. 2.2a-b, neutral stability curves for alternate bar formation ($m = 1$) and for higher transversal modes ($m = 2$, $m = 3$) are reported for both the plane-bed and dune covered configurations, which differ for the closure relationships reported in Appendixes A.1 and A.2.2.

The behaviour of the alternate bar growth rate $\omega_{1,r}$ versus k for different values of β is reported in Fig. 2.2c. For $\beta < \beta_c$, all perturbations decay in time ($\omega_{1,r} < 0$). For $\beta = \beta_c$, the perturbation of wavenumber k_c does not decay nor grow in time (neutral critical condition). For $\beta > \beta_c$, the growth rate becomes positive for a band of wavenumbers that does not span from 0 [1]. For bar formation, we make the classical

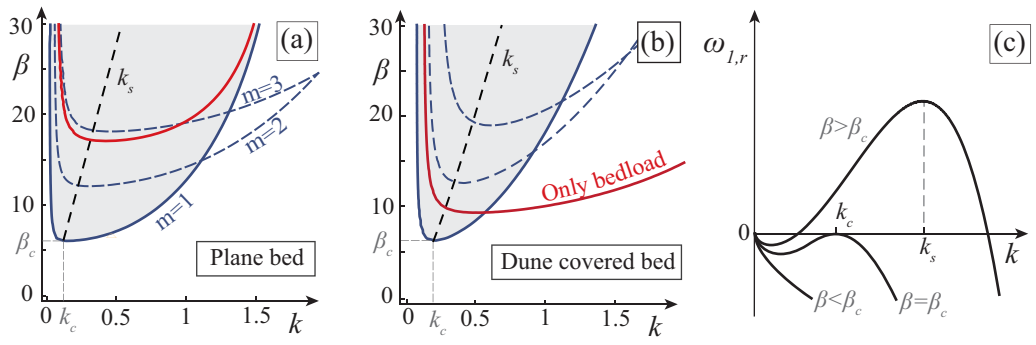

Fig. 2.2 Linear results. (a-b) The solid blue lines are the neutral stability curves for alternate bar formation in plane and dune covered configurations, with the unstable domains emphasized in gray ($\theta_0 = 0.5$, $d_s = 10^{-3}$, $R_p = 8$). The dashed blue lines stand for the neutral stability curves of higher transversal modes ($m = 2$, $m = 3$) and the solid red lines refer to the case where only the bedload is considered. (c) Growth rate for alternate bars $\omega_{1,r}$ versus the wavenumber k for diffent values of β. k_s is the wavenumber of maximal instability (black dashed lines in panels (a) and (b)).

assumption of linear theories that the wavenumber of maximum instability k_s, i.e., the fastest growing one, is the one that is most likely to be observed in nature. This assumption has already been verified on gravel bars (Blondeaux and Seminara, 1985). In Fig. 2.2a-b, the black dashed lines reveal the trend of k_s, which increases almost linearly with β.

The validity of the asymptotic approach (2.11)-(2.14) for suspended sediment is verified by the condition $\beta/k_s \gg \hat{U}_0/(2\pi\hat{W}_s)$, which is obtained by manipulation of eq. (2.11). Usually, β/k_s is one order of magnitude greater than the ratio between velocities. In order to ensure continuity with previous works on sand bar instability, the figures were obtained by fixing d_s, R_p and the Shield stress in the unperturbed condition θ_0 (however, a different combination of parameters may be chosen). Fig. 2.2 also shows how suspension influences the domain of instability (blue solid lines) to a great extent, reducing both β_c and k_c, especially in the plane-bed case, compared to the case where only bedload is considered (red lines).

This aspect is further explored in Fig. 2.3, where several neutral stability curves are plotted for different parameter combinations in the plane-bed configuration.

[1] Bars instability corresponds to the type I-oscillatory instability of the classification suggested by Cross and Hohenberg (1993).

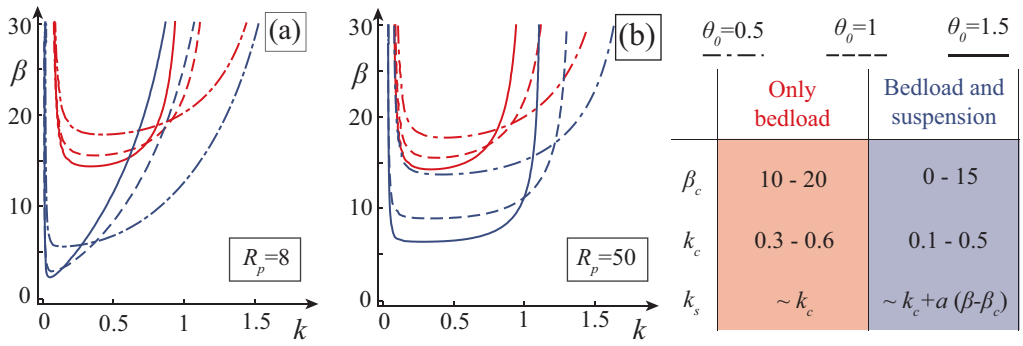

Fig. 2.3 Influence of suspension on sandbar linear instability for the plane-bed configuration. (a-b) Neutral stability curves for different θ_0 and R_p ($d_s = 10^{-3}$). The addition of suspension to bedload enhances bar instability, reducing β_c and k_c, especially for finer sediments (for panel (*a*) $\hat{d} \sim 0.1$mm and for panel (*b*) $\hat{d} \sim 0.5$mm). The table on the right shows the influence of suspension on the numerical outcomes of sandbar instability (usually $a \sim 0.015$).

Suspension is confirmed as a destabilizing mechanism that reduces β_c and leads to longer bars at the critical conditions (Federici and Seminara, 2006; Tubino et al., 1999). In the case where only bedload is considered, three dimensionless parameters, usually θ_0, d_s and β, define the problem, while suspension needs a fourth parameter to characterize the suspended particle size, i.e., R_p from eq. (2.17). For this reason, the red curves in panels (a) and (b) are the same, while the blue curves show that the destabilizing effect of suspension is enhanced for finer sediments ($\hat{d} \sim 0.1$mm for panel (a) and $\hat{d} \sim 0.5$mm for panel (b)). Some comparisons of how sediment transport influences the linear results of bar instability are presented on the right of Fig. 2.3. However, more precise considerations of general validity are jeopardized by the high number of control parameters, the two possible initial bed configurations (flat and dune covered), the instability of higher order transversal modes (central bars) and the absence of closed form relationships for k_s and the neutral stability curve. Overall, as suspension becomes the main sediment transport mechanism, neglecting it leads to incorrect predictions.

2.2.5 Weakly nonlinear order

In this section, we present a weakly nonlinear analysis performed through Center Manifold Projection (CMP), with the aim of providing an analytical solution for the finite amplitude of the fundamental mode ($m = 1$). The CMP has been verified as a powerful analytical method to simplify and rigorize the bifurcation analysis of

multiple-scale theories. In fact, the amplitude equations can be more easily derived and they are not constrained around the critical point, as they are in multiple-scale theories (Carr and Muncaster, 1983). In addition, CMP can be applied to study subharmonic and superharmonic instabilities (Armbruster et al., 1988; Bertagni and Camporeale, 2017). A good theoretical introduction to CMP can be found in Wiggins (2003), while the mathematical procedure, which we adopted, is shown concisely in the work by Cheng and Chang (1992).

The first step requires finding the solution to the linear adjoint eigenvalue problem

$$\left(\mathbf{L}_0^{\dagger}\omega_m^{*} - \mathbf{L}_1^{m,\dagger}\right)\mathbf{f}_m^{\dagger} = 0, \tag{2.25}$$

where the star * refers to complex conjugate, while the symbol † refers to the adjoint operator. In this case, the internal product that defines the adjoint operator is

$$\int_{-1}^{1} (\mathscr{L}\,\mathbf{x})\cdot\mathbf{y}^{*}\mathrm{d}n = \int_{-1}^{1} \mathbf{x}\cdot(\mathscr{L}^{\dagger}\mathbf{y})^{*}\mathrm{d}n, \tag{2.26}$$

where x and y are generic vectors. Through (2.26) and the boundary conditions (2.5), one obtains that $\mathbf{L}_0 = \mathbf{L}_0^{\dagger}$ and $\mathscr{L}_1^{\dagger}$ is the complex conjugate of $\mathscr{L}_1$ with the derivatives in n switched in sign. After proper normalization, the eigenfunctions of the linear problem $\mathbf{f}_m$ and the adjoint eigenfunctions $\mathbf{f}_m^{\dagger}$ become orthonormal with respect to the internal product (2.26) with $\mathscr{L} = \mathbf{L}_0$, so that

$$\int_{-1}^{1} (\mathbf{L}_0\,\mathbf{f}_m)\cdot\mathbf{f}_{m'}^{\dagger,*}\,\mathrm{d}n = \delta_{mm'}. \tag{2.27}$$

Let us recall the expansion of the perturbation in terms of the linear eigenfunctions (2.20). Unlike the linear analysis, when non-linearities are at play, the modes are coupled. Therefore, in order to evaluate the dynamics of the nearly neutral fundamental mode ($p = m = 1$), it is necessary to consider the dynamics of the stable modes (all other superharmonic and transversal modes). For the present analysis, the expansion (2.20) has been truncated to second-order harmonics ($n_p = n_m = 2$), since higher lateral and longitudinal harmonics provide a negligible contribution (it should also be noted that $A^{*}_{[m,p]} = A_{[m,-p]}$). By substituting (2.20) in the perturbation system (2.19), taking the internal product with the adjoint eigenfunctions and collecting the terms of the same Fourier modes, the equation for the nearly neutral amplitude

($A_{[1,1]}$) and the two equations for the stable amplitudes ($A_{[m,2]}$) are obtained

$$\dot{A}_1 = \omega_1(k)A_1 + P_1 A_1^* A_{[1,2]} + P_2 A_1^* A_{[2,2]}, \tag{2.28}$$

$$\dot{A}_{[m,2]} = \omega_m(2k)A_{[m,2]} + S_m A_1^2 + \cdots, \qquad (m = 1,2) \tag{2.29}$$

where we have posed $A_{1,1} = A_1$. Eqs. (2.28)-(2.29) represent a Galerkin-type projection of the full equations truncated at the second order non-linearities. The ellipses in the right hand side of eq. (2.29) refer to the omitted quadratic terms involving interactions of the stable modes, while the derivation of the coefficients P_i,S_j, which follows the procedure introduced by Cheng and Chang (1992), is reported in Appendix A.4. The fundamental mode, in the unstable domain close to the the neutral stability curve (see Fig. 2.2a-b), has a slow dynamics due to its weak instability. On the other hand, the stable modes have fast dynamics and can thus be projected onto the slow dynamics of the neutral or weakly unstable mode. Mathematically, this means that $A_{[m,2]}$ can be recast as a non-linear combination of the neutral mode A_1 and its complex conjugate A_1^* as follows

$$A_{[m,2]} = aA_1^2 + bA_1A_1^* + cA_1^{*2}, \tag{2.30}$$

where the projection coefficients a,b,c still have to be determined and the expansion has been truncated to $O(A_1^2)$ as the higher order corrections are negligible. The time derivative of (2.30) reads:

$$\dot{A}_{[m,2]} = 2a\dot{A}_1A_1 + b\left(\dot{A}_1A_1^* + \dot{A}_1^*A_1\right) + 2c\dot{A}_1^*A_1^*. \tag{2.31}$$

By substituting eqs. (2.28)-(2.29) and (2.30) in eq. (2.31), maintaining only the leading order terms and collecting like powers of A_1, A_1^*, one obtains

$$A_1^2\left[a\,\omega_m(2k) + S_m - 2a\,\omega_1\right] + bA_1A_1^*\left[\omega_m(2k) - \omega_1 - \omega_1^*\right] + cA_1^{*2}\left[\omega_m(2k) - 2\omega_1^*\right] = 0. \tag{2.32}$$

From (2.32), it is straightforward to conclude that $b = c = 0$ and $a = -S_m/(\omega_m(2k) - 2\,\omega_1)$, thus the stable amplitudes can be written as

$$A_{[m,2]} \sim -\frac{S_m}{\omega_m(2k) - 2\,\omega_1(k)}A_1^2. \tag{2.33}$$

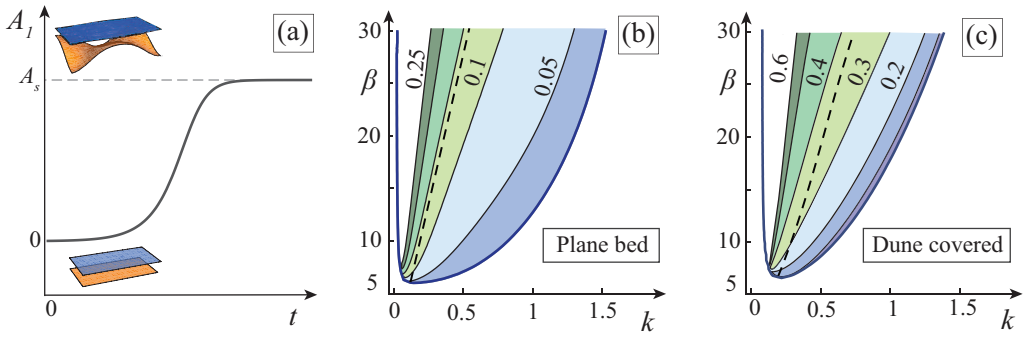

Fig. 2.4 Nonlinear results. (a) Amplitude dynamics in time as described by the Stuart-Landau eq. (2.34). (b-c) Contour plots for the dimensionless amplitude A_s, with a value that increases from blue to green (the same cases as Fig. 2.2a-b). The black dashed lines refer to k_s.

Finally, after substituting (2.33) into (2.28), the Stuart-Landau equation is obtained

$$\dot{A}_1 = (\omega_1 + \Xi |A_1|^2) A_1, \tag{2.34}$$

where Ξ is the complex Landau coefficient, whose analytical expression is reported in Appendix A.4. Eq. (2.34) describes the time dynamics of the fundamental amplitude. A graphical example of the amplitude dynamics, which refers to the real part of the equation, is reported in Fig. 2.4a. Starting from an infinitesimal perturbation, the amplitude initially grows exponentially through the ω_1 eigenvalue as expected from the linear analysis, then the rising effect of nonlinearities ($\Xi|A_1|^2$) dampens the growth, until an equilibrium value is eventually reached.

This equilibrium stationary value can readily be obtained by setting $\dot{A}_{1,r} = 0$, which gives, apart from the trivial solution, the finite amplitude $A_s = \sqrt{-\omega_{1,r}/\Xi_r}$. The contour plots of A_s in the instability domain are presented in Fig. 2.4b-c for plane and dune-covered bed configurations, respectively. In this case, the dune presence leads to higher bars. However, this is not a general rule, since the dune effect is negligible for other parameter combinations. The white areas in Fig. 2.4b-c are due to positive values of Ξ_r, which means there is no damping effect of nonlinearities, i.e., no saturation (this is a sign that a quintic-order Stuart-Landau equation is formally needed). However, these areas correspond to modes that are not observed in nature, as they grow much slower than k_s, see Fig. 2.2c, and they are easily destabilized by nonlinear interactions with neighborhood modes (Schielen et al., 1993). Dimensionally speaking, the amplitude reads $\hat{A}_s = 2A_s\hat{D}_0$, where the pre-factor 2 is due to the complex conjugation.

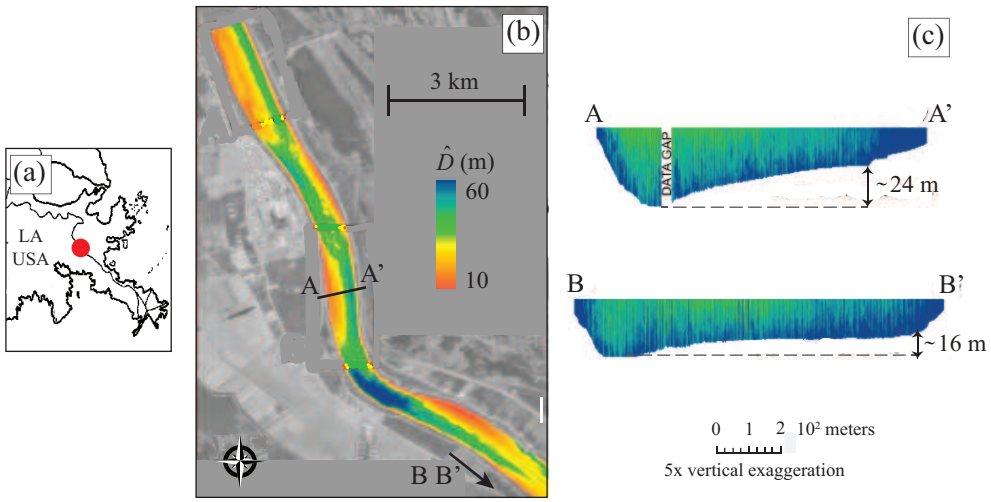

Fig. 2.5 Panels edited from Ramirez and Allison (2013)., (d-f) from Eekhout et al. (2013). (a) Location of the study reach on the Mississippi river in Louisiana, USA. (b-c) Submerged alternate bars revelead by the bathymetry and two cross-sections.

2.3 Validation and discussion of the results

From an experimental point of view, bedform formation characterized by a significant fraction of sediment transport in suspension is a very complicated task. For this reason, the conducted experiments have only focused on the role of bedload (e.g., Crosato et al. (2012)). In the laboratory experiments on bar patterns by Lanzoni (2000), some tests exhibited a certain amount of suspended load. However, bedload was still the main transport mechanism, and our theoretical predictions, which include suspended load, are almost the same one would obtain with those theories that only consider bedload (Colombini et al., 1987).

The lack of experimental data reduces the possibility of validating analytical and numerical models to just the few field observations of sandy bars present in literature. In the following, we focus on a reach of bathymetry of the Mississippi river (Ramirez and Allison, 2013) and on a field experiment in a straight artificial channel in the Netherlands (Eekhout et al., 2013). Some explicative figures regarding these two field studies are reported in Fig. 2.5 and 2.6.

The four dimensionless parameters necessary to define each case study are reported in Tab. 2.1, together with the field measurements and the theoretical predictions for the alternate bars. Closure relationships for sediment and suspended loads are the one used throughout the paper and reported in appendixes A.1-A.2 (Meyer-Peter

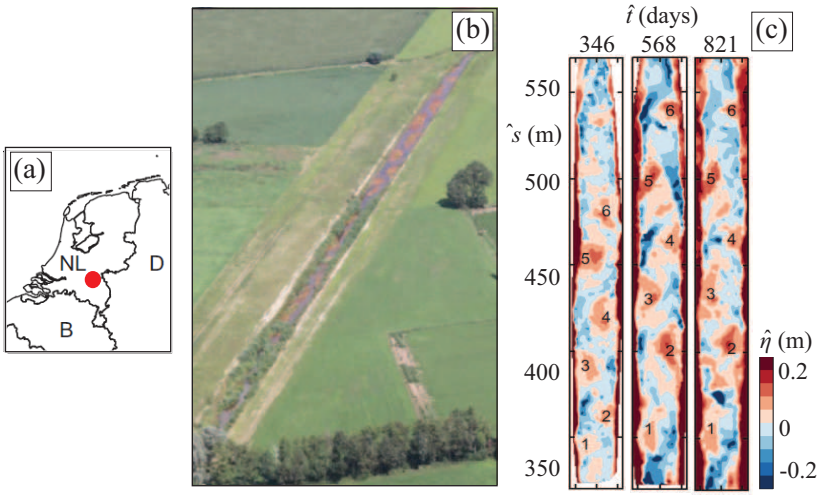

Fig. 2.6 Panels edited from Eekhout et al. (2013). (a) Location of the field experiment in the Netherlands. (b) Aerial photo of the artificial channel. (c) Detrended bed topography highlighting the six alternate bars at different times from the beginning of the experiment.

Muller formula for the bedload (Meyer-Peter and Müller, 1948) and the asymptotic approach (2.11)-(2.14) for the suspended load (Bolla Pittaluga and Seminara, 2003)). Finally, some speculative considerations are also made for partial data on the Yellow River in China (Ma et al., 2017).

2.3.1 The Mississippi River

The Mississippi River is the third longest river in the world (considering the Missouri-Jefferson), with a basin that covers one third of the United States, and it carries several kilotons of suspended sediment a day (Mossa, 1996). A field work conducted 100 km upstream of the delta in the Gulf of Mexico by (Ramirez and Allison, 2013), examined a 20 km reach of bathymetry and imaged five submerged alternate bars, which were usually obscured by murky water, see Fig. 2.5. These bars were approximately 6 km long and had heights that varied from 16 m to 24 m (with the height $\hat{H}$ measured from the bar trough to the bar crest and neglecting the effect of the banks). Comparisons of the *field* measurements (subscript f) and *theoretical* predictions (subscript t) of the present model are reported in Tab. 2.1. The model results have been obtained by fixing the hydrodynamic and sediment physical quantities to averaged values: $\hat{Q} = 14'307$ m^3/s is the mean flow rate recorded in the period 1961-2010; $\hat{U}_0 = 0.85$ is the averaged velocity for mean flow conditions;

Case	θ_0	$d_s(10^{-4})$	R_p	β	$\hat{L}_f$(m)	$\hat{H}_f$(m)	δ'	$\hat{L}_t$(m)	Δ_L	$\hat{H}_t$(m)	Δ_H
Miss.	0.66	0.113	13.6	20.6	6000	20	0.1	7500	25%	16	20%
								6650	11%	7	65%
E1	0.94	12	13	20	55	0.27	0.08	70	27%	0.26	2%
								58	6%	0.14	48%
E2	0.9	6	13	10.4	75	0.3	0.09	125	66%	0.35	17%
								–	$> 100\%$	–	$> 100\%$

Table 2.1 Data for the model validation. Miss. stands for the Mississippi River and E1, E2 for the artificial channel in the Netherlands after the formative events $\hat{Q}_1$ and $\hat{Q}_2$. The subscripts f and t stand for $field$ and $theoretical$, respectively. $\hat{H}$ is the height of the bar measured from the bar trough to the bar crest and $\hat{L}$ is the bar length. The small values of the δ' parameter prove the validity of the asymptotic approach (2.11)-(2.14). Δ_L (Δ_H) is the relative error between theoretical predicition and field measurement for the bar length (height). The model results for the case in which suspension is added to the bedload are presented in blue (considering only bedload leads to the results in red). Bar formation is not detected for E2 if the suspended load is not included.

$\hat{D}=20$ m is the averaged depth of the channel centreline; $2\hat{B}=825$ m and $\hat{d}=0.225$ mm (Ramirez and Allison, 2013). Moreover, the presence of 0.4 m high and 10 m long dunes, which were detected by the bathymetry, has been superimposed. The results show that the inclusion of suspension leads to longer and higher bars, which match the observations more satisfactorily for the bar heights and less precisely for the bar lengths. It should be pointed out that the constant values for the hydrodynamic and sediment quantities are approximations of reality that is unsteady and noisy. Moreover, other characteristics of this Mississippi reach differ from the model hypotheses, e.g., the reach is not straight and it is influenced to a great extent by anthropic activities that have not been considered in the present model. Nonetheless, the linear and nonlinear outcomes seem to correctly predict both the length and height of the bars.

2.3.2 The artificial channel in the Netherlands

The second field observations used to validate the model are the ones of Eekhout et al. (2013). The authors monitored the morphological evolution of a 600 m straight channel under unsteady flow conditions in the Netherlands for almost three years, see Fig. 2.6. The sediment was fine sand with $\hat{d}=0.218$ mm and the channel was 7.5 m wide, with a slope that adjusted from 1.8‰ at the beginning of the experiment to 0.9‰ at the end. Six alternate bars were observed in the final part of the reach after the first survey, which was performed 250 days from the beginning of the experiment. The bars were emerged for ordinary flows, and they became morphologically active during the flood events. However, the duration of these events was not sufficient to trigger migration of the bars, but only to adjust their amplitude and in second place their wavelength. For this reason, the bars were classified as non-migrating (steady) by the authors. From the hydrograph reported in Eekhout et al. (2013), it is reasonable to suppose that the bar geometry was initially shaped by two formative events of intensity $\hat{Q}_1 \sim 1$ m^3/s (days 150 and 210). Susbequently, bars became higher and longer when two floods of $\hat{Q}_2 \sim 2$ m^3/s occured (around day 550). After the $\hat{Q}_2$ events, the bars remained almost geometrically constant. This result is in agreement with the value of the unsteady coefficient $U \gg 1$ found by Eekhout et al. (2013), which showed that bar development was much slower than the time evolution of the basic flow, which was thus unable to affect the bars (Tubino, 1991). The dimensionless parameters for the two formative events ($\hat{Q}_1$ and $\hat{Q}_2$), and the

measurements and model predictions for the associated bars are reported in Tab. 2.1 with the names E1 and E2. The theoretical outcomes show that, as in the Mississippi River, the inclusion of suspension in the E1 case leads to higher and longer bars, which match the observations more satisfactorily for the bar heights. While the model detects bar instability only if suspended load is considered in the E2 case. In order to include the effect of the irregular channel bed in the field experiment, the closure relationships that account for dune presence have been used. Apart from the unsteady flow, other model hypotheses not fulfilled in the field experiment were the non-rectangular shape of the channel cross-section and the finite longitudinal length of the reach.

2.3.3 The Yellow River

A further comment can be made regarding a field work conducted by Ma et al. (2017) on the Yellow River, which owes its name to the huge amount of suspended sediment. The main focus of the paper by Ma et al. (2017) concerned the correct evaluation of the suspended load, which was underestimated by one order of magnitude when classical formulas were used. Our interest has instead been on the 1.5 km long longitudinal section of bathymetry surveyed by Ma et al. (2017) near one of the river banks. Because it is just a longitudinal section, it is not possible to make accurate deductions. However, the bathymetry data for the base flow revealed bedforms with a length/height ratio of 1200. The authors attributed such bedforms to extremely long dunes, which were not in agreement with classical theories that predict a ratio of between 10 and 100 (e.g., Colombini (2004)). Our interpretation is that those bedforms could actually be bars, for which our model has predicted a length/height ratio of 1100 ($\theta_0 = 1.05$, $d_s = 6\,10^{-5}$, $\beta = 113$ and $R_p = 3.5$). However, this ratio has been calculated as the bars were alternate bars, while, in reality, the very high β value causes many transversal modes to be unstable ($m > 1$). Therefore, any further considerations on wavelength and amplitude would not be reliable without more bathymetry data.

2.4 Concluding remarks

In this Chapter, the linear model of Federici and Seminara (2006) has been extended to the weakly nonlinear level through the Center Manifold Projection (CMP). In this way, the Stuart-Landau equation (2.34) for the bar amplitude and the analytical relation for bar finite amplitude have been achieved. Results show that suspension plays a quantitative role in bar formation: i) suspended load enhances the instability, reduces the critical aspect ratio β_c (see Fig. 2.2 and 2.3) and it may therefore lead to finite amplitude bars in conditions for which the bedload is not even sufficient to trigger the instability; ii) the critical wavenumber k_c is smaller (longer bars at critical condition) and the selected wavenumber k_s has an almost-linear dependence on the aspect ratio β; iii) suspended load usually increases bar length and height (see Tab. 2.1). In addition, both the linear and nonlinear outcomes have been satisfactorily verified with the few field observations of the sandy alternate bars present in literature. In particular, for one of the test cases, suspended load has proven to be crucial to detect bar instability, and for the other two cases, inclusion of suspension has increased the accuracy in the prediction of the bar height. Nonetheless, experiments would allow a further validation to be made. Formally speaking, the Stuart-Landau equation obtained through the Center Manifold Projection is not rigorously valid for the entire unstable domain (the gray areas in Fig. 2.2a-b). In fact, the application of CMP needs just one eigenvalue (ω_1, the one related to alternate bars) to be unstable. If, for example, the central bar eigenvalue (ω_2) is also unstable, the usage of eq. (2.34) becomes a further approximation. For this reason, the analytical relationships for alternate bars should not be used for multiple bars in braided rivers, where many transversal modes are unstable and nonlinearly interact among them. These results can be used in any engineering project that deals with river bedforms, such as bridges, groynes or bed regulations, and to study organizational patterns of channel forms in natural rivers and support restoration projects.

Chapter 3

Parametric transitions between bare and vegetated states on alternate bars

The work described in this chapter has been partially derived from Bertagni et al. (2018).

The conditions for vegetation spreading on alternate bars are here mathematically framed through a novel analysis encompassing flow unsteadiness. The three cornerstones of the present theory (flow variability, sediment transport and vegetation dynamics, henceforth referred as *ecomorphological triad*), are common to many aquatic and aeolian morphogenic features, and understanding their interactions is the mission of the emerging discipline of *ecomorphodynamics*. A physically-based and quantitative understanding of the ecomorphodynamic processes is still elusive. The reason of this failure is connected to the limited knowledge of the mutual interactions in the ecomorphodynamic triad. In practice, this goal has been addressed through field observations (Bertoldi et al., 2009), experiments (Gran and Paola, 2001; Tambroni et al., 2016) or numerical simulations (Bertoldi et al., 2014; Siviglia and Crosato, 2016). A limitation of these approaches is that they are partially able to shed light on the fundamental aspects of the involved dynamics, and need thus to be complemented with analytical models. To this end, advances have been achieved by considering just two issues at a time, such as flow stochasticity and vegetation (Camporeale and Ridolfi, 2006) or vegetation and sediment transport (Bärenbold et al., 2016).

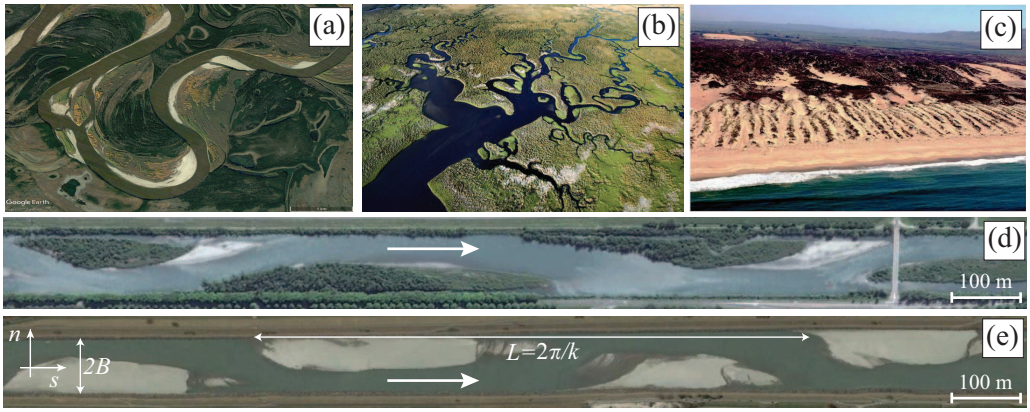

Fig. 3.1 Examples of vegetation spreading in water-driven systems. (a) Porcupine River (Alaska). (b) Everglades wetlands (Florida). (c) Parabolic coastal foredunes (California). (d,e) Two straight rivers with alternate bars and very similar hydrogeomorphological conditions, flow from left to right. (d) Vegetated bars on Isère river near Arbin, France. (e) Bare bars on Alpine Rhine, near Vaduz, Liechtentstein.

In this Chapter, we formulate an analytical physically-based approach that links for the first time all the aspects of ecomorphodynamics (flow stochasticity, vegetation dynamics and sediment transport) within the same theory. The rationale of the following theory is quite general and it could be broadened to different kinds of spatially extended vegetated systems forced by time-dependent disturbances, such as salt-marshes, wetlands, mangrove ecosystems, meandering rivers, aeolian dunes covered by biogenic crusts or coastal foredunes (Goldstein and Moore, 2016; Hurst et al., 2015; Kinast et al., 2013; Marani et al., 2010) (see Fig. 3.1a-c). Indeed all these systems share very similar processes embedded into the above mentioned ecomorphological triad.

In particular, the present theory addresses a yet open puzzling question of physical geography: why two single-thread fluvial systems, having nearly the same hydrogeomorphologic features (sediment size $\hat{d}$, slope S and mean annual discharge $\bar{Q}$), can assume two completely different states, for example, fully vegetated or bare bars (see Fig. 3.1d,e)? Physically speaking, the answer is that the phase space describing the dynamical system exhibits two different equilibrium points in the basin of attraction, thus making parametric transitions possible from one state to the other. To address the answer, an analytical theory that accounts for the triad interactions and describes the vegetated-unvegetated transition in morphologically active rivers is formulated. Implications range from unravelling certain mechanisms

underpinning effects of plants on rivers and landscape evolution through Earth history (Algeo and Scheckler, 1998; Gibling and Davies, 2012) to understanding the role of environmental and anthropogenic disturbances in water-driven patterns under changing scenarios.

3.1 Ecomorphological triad

The main result of our theory states that vegetation encroachment on bare sediment undergoing occasional inundation is a secondary instability problem whose asymptotic behavior can be summarized into a single parameter, α -given by (3.5)- which determines whether and how vegetation patterns develop. Thus, the spreading of plants is possible only if their biomechanical characteristics (e.g., growth rate and rooting efficiency) can cope with the removal action by stochastic floods in that particular sedimentary environment. The links among hydrology, biomechanics, and morphodynamics, are all contained in the parameter α, and determine its sign, which controls the transition from one to another state. Eventually, these processes select suitable plant characteristics in and among species and thus contribute to determine riparian vegetation biodiversity. We obtained this result by mathematically framing the processes of the ecomorphological triad as follows.

The scaling quantities are the same used in the previous Chapter, i.e., eqs. (2.6).

3.1.1 Flow variability

Modelling flow variability using a minimalist approach is a challenging task in river science, because of the non-trivial features of the discharge time series $Q(t)$ (e.g., long-term correlation, intermittent behavior, etc.). The Compound Poisson Process (CPP) provides a parsimonious and robust strategy (Botter et al., 2013) by addressing the stochastic equation $\partial_t Q = G(t) - Q/\mathscr{T}$, in which: t is time; $\mathscr{T}$ is the integral temporal scale (namely the integral of the autocorrelation function of Q); G is a shot noise with mean intervals between two pulses equal to $\mathscr{T} c_v^2$ and mean value $\bar{Q} c_v^2$; in which $\bar{Q}$ and c_v are the mean and the variation coefficient of the discharge. A sample realization of CPP is reported in Fig. 3.2a (blue line). At steady state, the pdf of the CPP is Gamma-distributed (right graph in Fig. 3.2a) and the upcrossing time t_ξ^+, i.e. the average time Q stays above a certain threshold ξ, is known in closed form (Laio

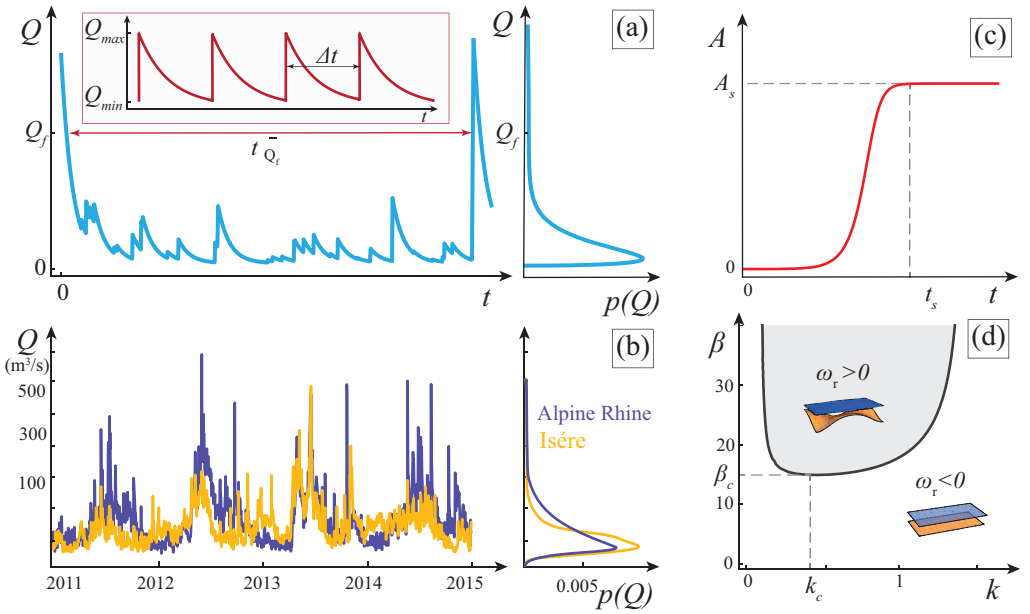

Fig. 3.2 Compound Poisson Process CPP (a-b) and alternate bar formation (c-d). (a) Simulated CPP for the river water discharge Q and its probability density function p_Q (light blue lines). The inset shows the periodic signal used for the Floquet theory (red lines). (b) Water discharge series for the Isère and the Alpine Rhine (last four years reported). Notice the different shape of the PDF, with the sharper Gamma distribution for the Isère. (c) Saturation of bar amplitude during a time t_s as described by the Landau (2.34). (d) Neutral stability curve discriminating the domain of bar formation (grey area) from the stable uniform solution (k is the longitudinal wavenumber, $d_s = 0.005$ and $Fr = 0.75$.)

et al., 2001)

$$t_\xi^+ = \mathscr{T} e^{\xi/\bar{Q}c_v^2} E\left(1-\frac{1}{c_v^2}, \frac{\xi}{\bar{Q}c_v^2}\right), \tag{3.1}$$

where $E(\cdot,\cdot)$ is the exponential integral function (Abramowitz et al., 1966). (3.1) will be used later on in the triad interaction.

3.1.2 Morphodynamics

The second element of the triad interaction – sediment transport – is a threshold process that activates when the flow rate overcomes a lower critical value, and becomes morphologically effective when an upper statistically rare flow rate Q_f, is overcome (Fig. 3.2(a)). This so-called *formative discharge*, an open issue in geomorphology, resets the riverbed by erasing any previous pattern and uprooting all vegetation. The bare flat state so created is the starting point of our analysis.

In a straight river with non-erodible banks, when $Q > Q_f$, the sediment transport morphodynamically triggers the pattern formation of migrating alternate bars (Fig. 3.1d-e). Starting from infinitesimal perturbations, the bar amplitude $A(t)$ asymptotically saturates to a finite value A_s in a nonlinear fashion (Fig. 3.2c), essentially following the Stuart-Landau equation (2.34) obtained in the previous Chapter. Notice that, in the present Chapter, we have only included the effect of bedload in bar formation, thus neglecting suspended load. The saturation time t_s is defined such that $A(t_s)$=$0.99A_s$ and $A(0)$=$0.01\,A_s$, and we stipulate that a condition for bar formation is that the formative event must have a duration at least equal to the saturation time, i.e. $t_{Q_f}^+ \geq t_s$.

From eq. (2.34), one obtains A_s=$\sqrt{-\omega_r/\Xi_r}$ and $t_s \sim 6.6/\omega_r$. Furthermore, as the definition of the formative discharge reads Q_f=$2\beta Fr\sqrt{g}(\hat{d}/d_s)^{5/2}$, both the saturation time and the formative discharge are functions solely of the morphodynamic parameters (d_s, $\hat{d}$, β, Fr). This allows us to define just two out of the three CPP parameters $(\bar{Q}, c_v, \mathscr{T})$, because the third one is given by the above-mentioned condition for bar formation, i.e., $t_{Q_f}^+(\bar{Q}, c_v, \mathscr{T})$=$t_s$. With the aid of (3.1), such condition leads to

$$\mathscr{T} \sim (t_s Q_f)/(c_v^2 \bar{Q}), \quad \text{for } Q_f \gg \mu. \tag{3.2}$$

3.1.3 Vegetation dynamics

After the formative event is extinguished, the flow decreases to ordinary values, reducing the water level and letting the crests of the recently formed bars emerge. At this point, vegetation may grow on the dried areas depending on flow variability. Vegetation is assumed to develop by following a logistic Holling type-III equation, wherein the carrying capacity, $\hat{K}$, can be assumed as a quadratic function of the water depth, $\hat{K}$=$\hat{K}(D)$ (Camporeale and Ridolfi, 2006; Muneepeerakul et al., 2007). In fact, fluvial tree species usually perform the maximum growth when the water table is at an optimal depth: at lower stages the roots cannot reach the water, while at higher stages, water logging occurs, thus reducing respiration and gas exchange in the root zone (Naumburg et al., 2005). In addition, the submerged sites experience a decline in vegetation because of anoxic conditions and uprooting induced by flow drag, that is proportional to the water velocity squared (Bärenbold et al., 2016; Perona et al., 2014). After assuming a linear relationship between flow drag and biomass removal, and defining ϕ, as the density of biomass per unit area normalized to the maximum carrying capacity, we have

$$\frac{\partial \phi}{\partial t} = \nu_g \phi (K - \phi) - He(D) \nu_d D (U^2 + V^2) \phi, \tag{3.3}$$

where ν_g, and ν_d are dimensionless growth and decay factors of vegetation and are proxies of the plant biomechanical properties in relation to the specific hydromorphological context and K is the normalized carrying capacity (see Sec. B.1) ; $He(\cdot)$ is the Heaviside function (i.e., the decay is active only at submerged sites, when the water depth D is positive). We emphasize that, since the water velocities (U,V) and depth D account for the presence of the bar, the coefficients of (3.3) are space and time dependent. During ordinary flows, it is likely that sediment transport vanishes in most of the submerged sites, so that the bars can be approximately regarded as stable, until the occurrence of the next formative event. Moreover, the different time scales for bar saturation, order of days, and vegetation growth, order of years, allows us to separate mathematically the process and treat it analytically.

In this description, vegetation develops as a *secondary* instability (Schmid and Henningson, 2012) over the finite-amplitude bed topography. Encompassing bar topography in space and flow variability in time, a secondary instability is therefore

performed by linearising (3.3) about a *new* basic state (labelled with tilde), namely

$$\tilde{D} = D_u(t) + A_s \hat{D}_1(k)\mathbf{f}_1(n)e^{\mathrm{i}ks}. \tag{3.4}$$

In (3.4), the first term r.h.s. refers to the uniform solution, which is dependent on time through the CPP ($D_u(t)$ is related to $Q(t)$ through Manning's equation). The second term accounts for the presence of the finite amplitude bars (through eqs. 2.20), in which $\hat{D}_1$ and $\mathbf{f}_1$ are the linear perturbation of the water depth and its transversal structure. Similar forms are considered for the other variables. In order to make the computation analytically accessible, we substitute the discharge stochastic time series with a statistically equivalent periodic one, constituted by a repetition of the typical mean hydrograph. The latter is obtained by the following compatibility conditions (see red curve in Fig. 3.2a): i) the duration of the event equals the average interval between subsequent shots, $\Delta t = \mathscr{T} c_v^2$; ii) the discharge mean value between formative events is preserved; iii) the peak value is such that the coefficient of variation c_v of the stochastic series is preserved. In this manner, the time dependency in (3.3) becomes periodic and Floquet's theorem can be applied. Thus, linearising (3.3) around (3.4), the solution for the vegetation is $\phi \sim P(t)e^{\alpha(s,n)t}$, where $P(t)$ is a periodic function and $\alpha(s,n) \in \mathbb{R}$ is the so-called Floquet exponent, which reads

$$\alpha = \frac{1}{\Delta t}\int_0^{\Delta t} (\nu_g \tilde{K} - \nu_d \theta(\tilde{D})\,\tilde{D}(\tilde{U}^2 + \tilde{V}^2)\,dt, \tag{3.5}$$

where $\tilde{K}$=$K(\tilde{D})$. We remind the reader that α is spatially distributed and its sign provides the asymptotic behavior of the secondary instability: wherever $\alpha > 0$ vegetation patterns develop. The value of α is more easily evaluated numerically, as the analytical solution of the integral in (3.5) is particularly cumbersome. Although the above theory has been described for river systems, it is quite general, and the same steps could be repeated for other ecogeomorphologic systems driven by unsteady flows.

3.2 Results and discussion

3.2.1 Parametric transitions driven by flow variability

Once the triad interaction is set up (i.e., hydrodynamics, sediment and vegetation parameters are provided), the present mathematical framework can evaluate the surface area of alternate bars where plants endure flow variability ($\alpha > 0$) between two formative events resetting the morphology. A graphical example of finite amplitude computation and pattern formation is given in Fig. 3.3a. Let us define the *Areal Vegetation Index*, AVI, as the ratio of the vegetated area over the emerged area at the minimum discharge, Q_{min}, i.e., the region theoretically colonisable by vegetation. Fig. 3.3b shows the dependence of AVI on flow variability c_v, for two typical cases: a sand bed river (orange line) and a gravel bed one (light blue line). These two rivers share the same mean discharge $\bar{Q}$, formative event $13\bar{Q}$, and channel width, but they differ in term of the sediment and the Froude number Fr (a proxy of slope variation). This, in turn, affects the CPP correlation $\mathscr{T}$ through (3.2). The two cases exhibit analogies and discrepancies. In fact, both rivers show that higher flow variability (increasing c_v and thus Q_{max}) reduces the bar portion colonized by vegetation. In particular, there is a threshold value of flow variability, henceforth referred to as c_v^*, above which plant growth is completely inhibited (namely AVI decays to zero). In such conditions, vegetation does not have sufficient time to develop since it is frequently removed by the flow. This c_v^* threshold corresponds to a parametric transition from vegetated to bare states. On the other hand, there is also a lower limit in the flow variability, which precludes the discharge time series to reach the formative event that is necessary to bar formation. In-channel vegetation can in fact develop just after bars with finite amplitude are formed. Concerning the discrepancies, the longer saturation time of the sand bed river (10 hours) with respect to the gravel bed river (2 hours), corresponds -via (3.2)- to a discharge time series that is more correlated in the former case. This leads to longer submergence periods in the sand river and to plant uprooting for a fatigue stress. In the gravel river, the periods of bar submergence are instead shorter, but the more frequent events are equally able to remove mature vegetation. Another discrepancy concerns the two values of c_v^*, due to distinct slopes and bar heights. Under the same discharge conditions, the gravel bed river exhibits higher bars and shallower water depths and

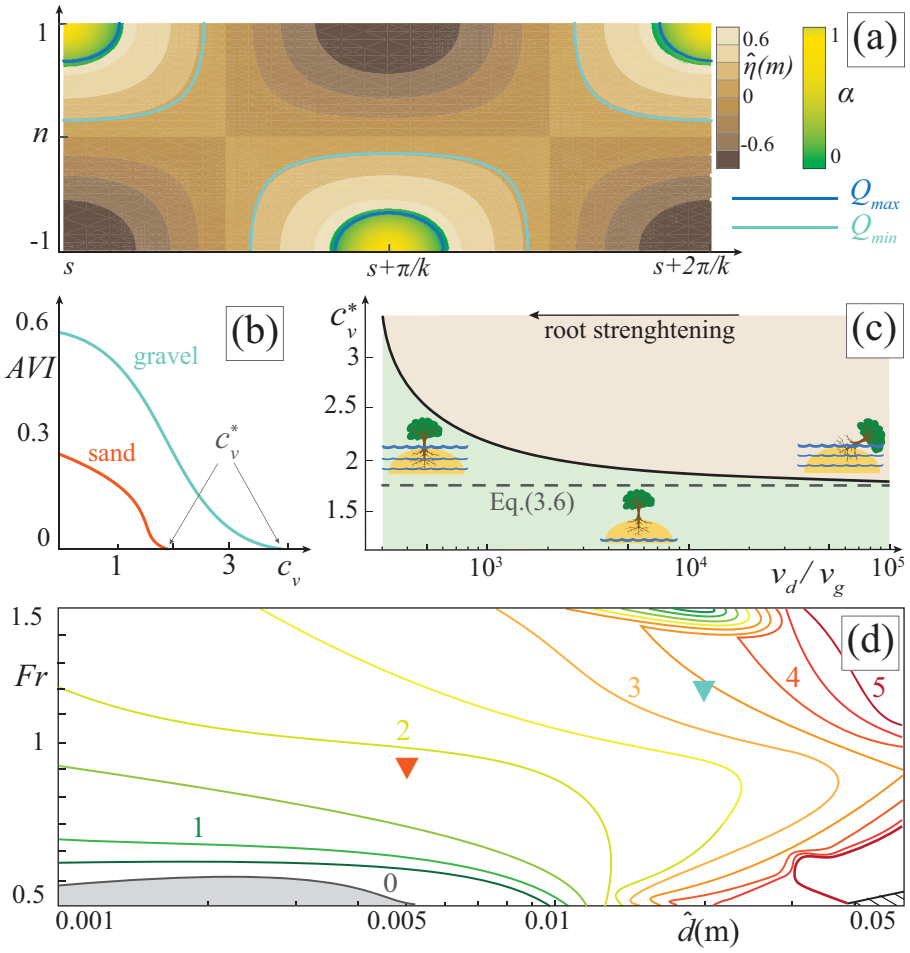

Fig. 3.3 Parametric transition driven by flow variability (all graphs obtained for $\{\bar{Q}[\mathrm{m}^3/\mathrm{s}], \hat{Q}_f, 2\hat{B}[\mathrm{m}]\}=\{45, 13\bar{Q}, 80\}$). (a) Density plot of $\alpha(s,n)$ and $\eta(s,n)$ for a finite amplitude bed topography of a sand river $\{Fr, \hat{d}[\mathrm{mm}]\}=\{0.9, 5\}$. The maximum ($Q_{max}$) and minimum ($Q_{min}$) water levels are marked by colored solid lines. (b) Areal Vegetation Index versus c_v for the sand bed river (orange line) and a gravel bed river (light blue line, $\{Fr, \hat{d}[\mathrm{mm}]\}=\{1.2, 20\}$). In evidence, the threshold c_v^* discriminating between vegetated and bare state. (c) Transition variation coefficient c_v^* discriminating the bare (light brown) and vegetated state (green) as a function of the dimensionless vegetational parameters (same data set of the sand river of panel *b*). As the root system strengthens, plants endure more easily flow variations (c_v^* increases). Dashed line is the prediction of (3.6). (d) The behavior of c_v^* in the parameter space. The triangles refer to the rivers of panel *b*. Grey and dashed areas correspond to no bar formation and no bedload, respectively.

requires the maximum discharge Q_{max} (or flow variability) to be higher in order to flood the bar top and remove all the vegetation.

The value of c_v^* is a key quantity, which results from an equilibrium between plant growth and decay. It corresponds to the flow variability that nullifies the integral (3.5) at the most favored site, that is the bar top. The exact way to compute c_v^*, which is a cumbersome formulation, is provided in Sec. B.2. However, as the uprooting mechanism is much faster than plant growth, it is possible to simplify c_v^* evaluation assuming that no vegetational pattern develops when the maximum flow (Q_{max}) reaches the bar top. In this way, c_v^* can be numerically obtained as the solution of the following equation

$$D_0(c_v^*, Q_{max}) + A_s \left[\hat{D}_1(k) + \hat{D}_1(-k)\right] \sim 0. \tag{3.6}$$

Figure 3.3*c* shows that the above approximation is asymptotically exact for very fast uprooting (i.e., $\nu_d/\nu_g \gg 1$, typical values are of order 10^4). With the aid of (3.6), the behavior of c_v^* can be investigated in the parameter space (Fig. 3.3d). In the region where bedload transport occurs and alternate bars develop, c_v^* generally increases when moving from subcritical sand bed rivers ($Fr<1$, $\hat{d}<2$ mm) to supercritical gravel bed ($Fr>1$, $\hat{d}>2$ mm). This mechanism allows vegetation spread in mountain rivers with high flow variability.

3.2.2 Test cases

The computation of AVI is here shown for five actual fluvial cases of widespread interest to the scientific community (a summary of river features and validation results is provided in Tab. 3.1). The Isère (France) and the Alpine Rhine (border Austria-Switzerland) share almost identical hydrodynamic and sediment parameters (Fig. 3.1d-e), but flood events of the latter are much stronger and flow variability is higher (Adami et al., 2016; Serlet et al., 2018). This implies slightly lower bar elevation in the Alpine Rhine, with frequent inundation and consequent inhibition of plant growth. In contrast, the slightly more regular discharges of the Isère favor vegetation development. Another test case concerns the Vedder canal in Canada (Ferguson et al., 2011). Upstream of the canal, the river is braided with multiple vegetated bars. In the canal itself, the bed is narrower with well-developed alternate bars that are easily submerged by ordinary flows. Thus no vegetation develops in the

canal (see Fig. B.5). Finally, the Arc river (France) has undergone a width reduction due to the construction of a highway in the nineties (Jaballah et al., 2015). This triggered a parametric transition between a fully vegetated condition to a weakly vegetated bed (see Fig. B.6), where plants are periodically uprooted by annual flood events.

As also reported in Fig. 3.4, the present theory quantitatively captures the underlying physics providing a good matching between theoretical predictions and measurements. A partial exception is the actual vegetation cover of the Arc river, which is not fully captured. This might be due to: i) the very strong anthropic influences upstream of the study area (dams and sediment mining); ii) the Arc river has not yet reached the ecomorphological equilibrium and thus we might expect bars to slowly vegetate in the future.

These encouraging results may be useful to depict changes in biogeomorphological styles induced by man in the Anthropocene and of natural origin since the Paleozoic. For example, the model is able to capture the underlying physics for the river environments tested here, and provide insights about the physical conditions that must subsist in order to allow for the colonization and the spreading of plants. Thus, the recent Devonian plant hypothesis, which suggests how plant root evolution might have contributed to the spreading of vascular plants (Gibling and Davies, 2012), is supported by this theory. In fact, more robust root systems lead to a decrease in the uprooting coefficient ν_d and to a transition to vegetated states, Fig. 3.3c. However, further implications concerning how established plants have in turn affected landscape evolution are not contained in the present theory. This requires introducing the feedback of vegetation cover on morphodynamics and would explain why our river bar model underestimates the vegetated bar length (Tab. 3.1) with respect to the linear theory. Similarly, other processes not accounted for in this analytical theory concern sediment mining, alteration of sediment supply because of hydropower regulation, different root morphologies and conditions for seed dispersal.

3.3 Concluding remarks

This novel methodology couples the three main processes controlling ecomorphodynamic pattern formation under a single analytical model. Results show that flow

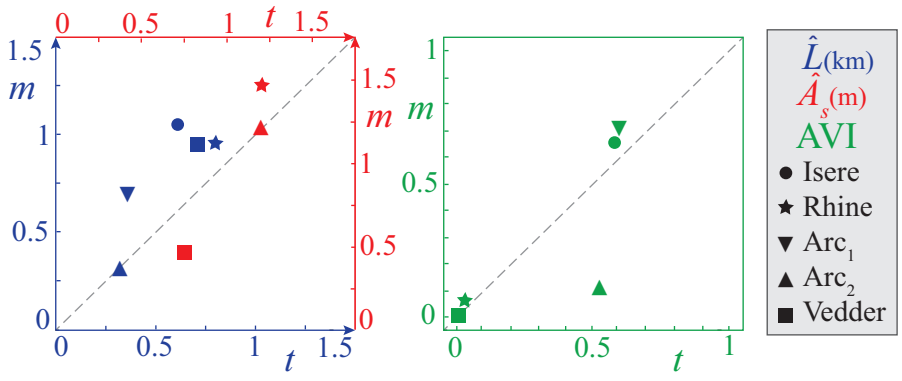

Fig. 3.4 Comparison between theory (t) and field (f) measurements for the bar wavelength $\hat{L}$ (blue), amplitude $\hat{A}_s$ (red) and AVI (green). Dataset is reported in Tab. 3.1

variability discourages vegetation growth, up to the point that above a certain threshold, c_v^* in (3.6), plant spread is completely inhibited. Such transition from vegetated to bare state depends parametrically on flow stochasticity, morphology and plant biomechanical characteristics. In particular, c_v^* is generally higher for gravel-bed rivers than sand-bed rivers and it increases for plants that can endure periodical submergence. This last outcome supports the idea behind the Devonian plant hypothesis, for which plant root evolution might have contributed to the spreading of vascular plants through the Paleozoic. The mathematical framework of this model can be adapted to other extended vegetated systems forced by unsteady flow conditions and it may serve practitioners such river scientists and water managers to predict the effect of changing flow-regime scenarios, or better plan restoration works (Montgomery, 1997; Wohl et al., 2015).

River	$\bar{Q}[m^3/s]$	c_v	c_v^*	$\hat{Q}_f[m^3/s]$	$\hat{d}[m]$	$S‰$	$2\hat{B}[m]$	$\hat{L}_f[m]$	$\hat{A}_{s,f}[m]$	AVI_f	$\hat{L}_t[m]$	$\hat{A}_{s,t}[m]$	AVI_t
Alpine Rhine	150	0.65	1.1	2200	0.02	2	110	950	1.5	0.05	800	1.2	0.03
Isère	120	0.5	2.6	800	0.02	2	120	1050	n.a	0.65	610	1.55	0.58
Arc_1	15	1	7.7	500	0.08	6	70	680	n.a	0.70	360	1.45	0.6
Arc_2	15	1	3.8	500	0.08	6	50	290	1.25	0.10	310	1.2	0.52
Vedder	67	0.75	0	650	0.001	0.7	90	950	0.5	0	710	0.75	0

Table 3.1 Arc_1 and Arc_2 refer to before and after the highway construction, respectively. The subscripts f and t stand for *field* and *theory*, respectively. For the river satellite pictures and the daily discharge series see Sec. B.3 and Fig. B.3-B.6.

Part II: Cave and glacial patterns

Patterns carved by water in ice or stones are ubiquitous in nature and their beauty attracts the curiosity of most, scientists and common people alike (see Figures 1.3-1.4). In most cases, the driver of the instability is a thin water film (some micrometers thick) and the resulting patterns on the solid substrate (calcite or ice) appear very similar, even though the underlying instability mechanisms are different. In fact, in the karst environment, pattern formation is caused by precipitation-dissolution phenomena, and in the ice environment, by melting-freezing processes. However, as both the chemical and the thermodynamical processes are driven by the thin water film dynamics, the resulting patterns are very much alike and a unified mathematical approach is sometimes possible.

The water film dynamics can be studied through the Benney equation, so-called after the original work of Benney (1966). This strongly nonlinear equation mathematically describes all physical phenomena happening in a thin water film through just one variable, i.e., the film thickness h. In the last decades, the Benney equation has been broadly analysed (Dávalos-Orozco et al., 1997; Joo et al., 1991b; Rosenau et al., 1992), improved (Ruyer-Quil and Manneville, 1998, 2000) and extended to its weakly nonlinear version (Hyman et al., 1986; Oron and Rosenau, 1989; Sivashinsky and Michelson, 1980). In the following Chapters, we derive a Benney-type equation, through the classical long-wave theory for falling films (Craster and Matar, 2009; Kalliadasis et al., 2011), that also accounts for the evolving solid topography η. The coupling of our Benney-type equation with a wall evolution equation, which depends on the environment considered, provides the morphological system.

In the glacial environment, a good physical approximation of the ice-water interface dynamics is given by the Stefan equation. This equation was first used by Stefan (1891) to study the thickness of sea ice and since then, it has been used in every problem dealing with a phase-change and a moving interface (Camporeale and

Ridolfi, 2012a; Mantelli et al., 2015; Rubinštejn, 2000; Ueno, 2007). The advantage is that all heat fluxes, i.e., latent heat released by freezing water (or absorbed by melting ice), heat conducted in the ice and heat convected and conducted by water, are balanced in just one equation which dynamically describes the evolution of the solid-liquid interface.
Regarding the cave environment, less research has been performed to find a proper physical equation that might describe the time evolution of the solid substrate. Normally, empirical equations calibrated through observations are used. In these equations, the common approach is to consider a film of water over-saturated in Ca that favors the precipitation of $CaCO_3$ through some proportional coefficient (Camporeale, 2015; Dreybrodt, 2012; Short et al., 2005). The same equations handle with under-saturated water that causes erosion (the proportionality coefficient just switches in sign). In this sense, more work to properly address the evolution of the calcite substrate is needed.

In Chapter 4, a unified approach is adopted in the study of karst and ice flutings, which are longitudinally oriented organ-pipe-like patterns common in caves (Fig. 1.3d) and ice-falls. These stunning patterns had already been linearly modelled (Camporeale, 2015). However, the mathematical approach here presented has furnished a considerable simplification in the analytical relations and has consequently allowed for a first nonlinear investigation of the problem.

Chapter 5 deals with the problem of icicle formation. A recent extensive experimental study of icicles (Chen and Morris, 2013, 2011) revealed that small amounts of dissolved impurities are required for ripples to appear (see Fig. 1.4b). This is contrary to existing linear stability theories (Ogawa and Furukawa, 2002; Ueno, 2007; Ueno and Farzaneh, 2011; Ueno et al., 2009b), which would predict ripples on icicles formed from pure water. The model here proposed shows that icicles made of pure water do not develop ripples. Moreover, some considerations on the reason why dissolved impurities drive the ripple instability are presented.

Chapter 4

Nonlinear and subharmonic stability analyses of fluting formation

4.1 Introduction

The work described in this chapter has been partially derived from Bertagni and Camporeale (2017).

Fig. 4.1 shows two pictures regarding the target of the present work, that is the formation of longitudinally oriented organ-pipe-like structures, called flutings, which are widespread in caves and ice-falls. Flutings are due to a gravity-driven thin film flowing over an inclined (usually overhanging) plane, composed of stone or ice. In the cave case, the underlying process is the precipitation-dissolution of calcite content dissolved in the water film, while in the ice case the freezing-melting condition is determined by a heat flux balance at the liquid-solid interface. Although the driving mechanism is different in the two environments, a previous work has shown that a unified approach is possible (Camporeale, 2015), since at *inverted conditions* ($\vartheta > \pi/2$, where ϑ is the angle with the horizontal) the key role in driving the morphogenesis is played by the free surface dynamics.

The film dynamics is addressed through a Benney-type equation, obtained through the classical long-wave theory (Craster and Matar, 2009; Kalliadasis et al., 2011) with the novelty that also the lower boundary (the solid substrate) is movable. The coupling of the Benney-type equation with a wall evolution equation provides an algebraic eigenvalue problem considerably simplified, but in complete

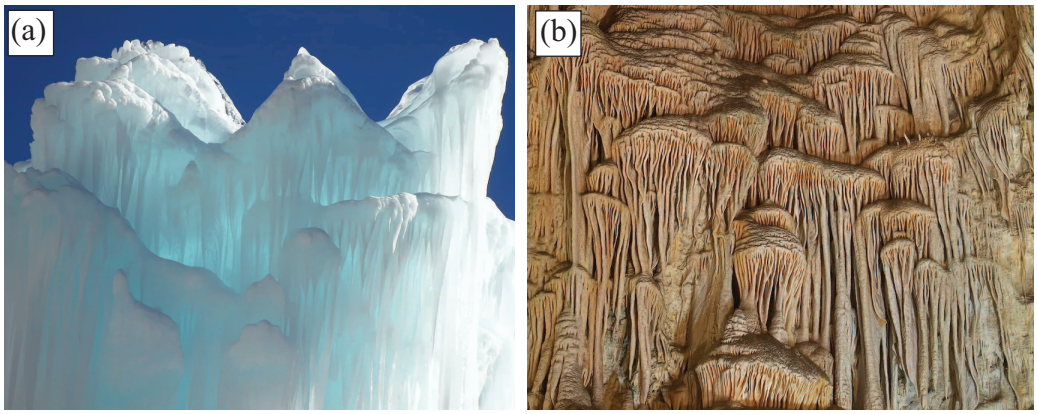

Fig. 4.1 (a) Example of ice flutings, photo courtesy of Antonio Giani. (b) Flowstone with cave flutings, photo courtesy of Alexey Sergeev.

agreement, with respect to the outcomes of the previous work (Camporeale, 2015). Namely, flutings are long-wave instabilities that develop at inverted conditions for all Reynolds numbers. This simplification has furnished a more suitable form for the eigenfunctions and therefore has allowed for a nonlinear investigation of the problem, performed through the Center Manifold Projection.

Formally, the sum of the linear and nonlinear solutions define in a complete way the spatial structure of flutings in the parameter space. Nevertheless, finite-amplitude monochromatic waves may be destabilized by modes with different wavenumbers. In experimental and theoretical works on falling liquid films (Brauner and Maron, 1982; Cheng and Chang, 1995; Liu and Gollub, 1993), sideband and subharmonic instability were detected. Subharmonic instability was also found in other open-flow systems with long-wave instabilities (Kelly, 1967; Monkewitz, 1988; Prokopiou et al., 1991). However, we point out that differently from these last works, in our system the modulation is not parallel to the base flow, but it is transversal to it, see Fig. 4.2. For these reasons, we have performed a subharmonic stability analysis, showing that, even though the subharmonic of the fundamental is linearly unstable, the rising effect of the non-linearities may allow the fundamental to saturate and the subharmonic to decay. From a practical point of view, this means that the predictions of the linear and nonlinear analyses are robust.

To verify the outcomes of the analytical model, numerical simulations of the full equations have been performed.

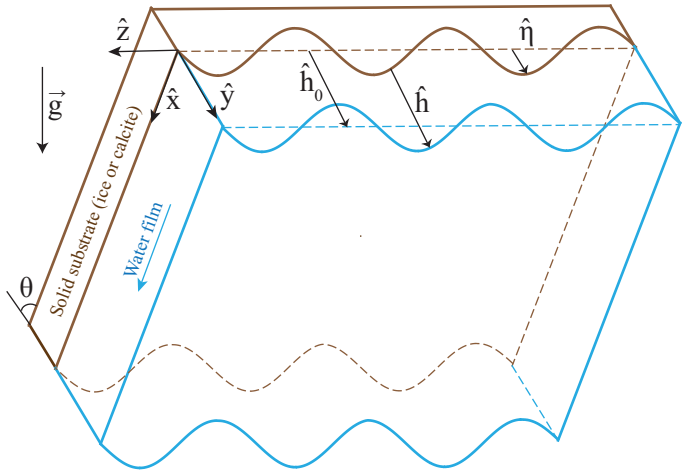

Fig. 4.2 Sketch of the water film flowing down the solid substrate.

This Chapter is organized as follows: in section 4.2 the mathematical problem is formulated for both types of patterns, ice and karst flutings; in section 4.3 the linear analysis is performed and an explicit form of the selected wavelength of the fundamental is given; in section 4.4 the Stuart-Landau equation for finite amplitude of flutings is achieved through the center-unstable manifold technique. Then, the stability of the finite-amplitude to subharmonic disturbances is verified both analytically and numerically. Finally, the outcomes of the numerical simulations of the full equations are provided. Last section 4.5 presents a discussion of the results.

4.2 Mathematical model

4.2.1 Water film dynamics through long-wave theory

The dynamical system leading to fluting formation consists in a water film flowing over an overhanging evolving solid substrate (calcite or ice), as presented in the sketch of Fig. 4.2. The unperturbed solution for the water film provides the well-known Nusselt's semi-parabolic velocity profile (Nusselt, 1916), whose solutions in terms of film thickness $\hat{h}_0$ and surface velocity $\hat{u}_0$ are

$$\hat{h}_0 = \left(\frac{3\nu\hat{q}}{g\sin\vartheta}\right)^{1/3} \qquad \hat{u}_0 = \left(\frac{9g\hat{q}^2\sin\vartheta}{8\nu}\right)^{1/3}, \tag{4.1}$$

where ν is the kinematic viscosity, g the gravitational acceleration, ϑ the angle with the horizontal and $\hat{q}=2\hat{u}_0\hat{h}_0/3$ the flow rate per unit span. The hat refers to dimensional variables. Flutings usually develop with very low Reynolds numbers ($Re=\hat{h}_0\hat{u}_0/\nu \ll 1$), a slope of the interface not too far from verticality and small ratio ε between the film thickness and the pattern wavelength (order 10^{-3}), so that they can be regarded as long-wave instabilities. This is especially so when the effect of surface tension is predominant with respect to viscous stresses, i.e., high values of the Weber number $We{=}\sigma/(\rho\hat{h}_0\hat{u}_0^2)$, being σ the surface tension and ρ the water density. In the case of a film flowing over a fixed flat boundary, the long-wave approach through the so-called gradient expansion Kalliadasis et al. (2011), leads to the well-known Benney equation (Benney, 1966) and its weakly nonlinear versions (Kuramoto-Sivashinsky equation) (Hyman et al., 1986; Oron and Rosenau, 1989; Sivashinsky and Michelson, 1980), see (Craster and Matar, 2009) for a complete review. In the present morphodynamic context, the gradient expansion technique is extended to the case where the lower boundary is also unknown and deformable (see also (Camporeale, 2017) for a recent application in the crenulation instability problem).

The variables are made dimensionless through the following scaling

$$(\hat{x},\hat{z})=\hat{L}(x,z), \qquad (\hat{y},\hat{\eta},\hat{h})=\hat{h}_0\,(y,\eta,h), \qquad \hat{t}=\frac{\hat{L}}{\hat{u}_0}t \tag{4.2}$$

$$(\hat{u},\hat{w})=\hat{u}_0(u,w), \qquad (\hat{v},\bar{V})=\frac{\hat{h}_0\hat{u}_0}{\hat{L}}(v,\bar{v}), \qquad \hat{P}=\rho\,\hat{u}_0^2P, \tag{4.3}$$

$$\tag{4.4}$$

where (x,y,z) are defined as the dimensionless downslope, normal-to-the unperturbed solid surface and span-wise directions, respectively (see Fig. 4.2); $\mathbf{u}=(u,v,w)$ are the corresponding velocities and P stands for pressure. The elevations $y=\eta(x,z,t)$ and $y=\eta(x,z,t)+h(x,z,t)$ correspond to the liquid-solid interface and the free surface, respectively. $\hat{L}$ is the fluting wavelength, which is a-priori unknown. Notice that at this level, the $\hat{L}$ value is not needed, the only necessary assumption is that $\hat{h}_0/\hat{L}\ll 1$, i.e., the fluting typical wavelength (order of cm) is much longer than the film thickness (order of μm). After applying the scaling (4.2), the non-dimensional

governing equations are

$$\nabla \cdot \mathbf{u} = 0, \tag{4.5}$$

$$\varepsilon Re(u_t + \mathbf{u}\cdot\nabla u) + \varepsilon Re\, P_x - u_{yy} - 2 = O(\varepsilon^2), \tag{4.6}$$

$$Re\, P_y - \varepsilon v_{yy} + \zeta = O(\varepsilon^2), \tag{4.7}$$

$$\varepsilon Re(w_t + \mathbf{u}\cdot\nabla w) + \varepsilon Re P_z - w_{yy} = O(\varepsilon^2), \tag{4.8}$$

where subscripts refer to the partial derivatives, ζ is the dimensionless parameter that accounts for the slope of the solid substrate

$$\zeta = 2\cot\vartheta, \tag{4.9}$$

and we have introduced the *film parameter*

$$\varepsilon = \frac{\hat{h}_0}{\hat{L}}. \tag{4.10}$$

Notice that for fluting formation, i.e., $Re \ll 1$, the convective terms in (4.6)-(4.8) could be neglected. In Sec. 4.3.1 we show why it is instead important to keep these terms. On the liquid-solid interface, no slip and the dynamic condition are

$$u = w = 0, \qquad\qquad v = \eta_t\ ; \tag{4.11}$$

while on the free surface, the boundary conditions read

$$(h+\eta)_t = -v + u(h+\eta)_x + w(h+\eta)_z, \tag{4.12}$$

$$P + 2\varepsilon\partial_y v/Re = -We[(h+\eta)_{xx} + (h+\eta)_{zz}], \tag{4.13}$$

$$u_y = w_y = 0. \tag{4.14}$$

Equations (4.13)-(4.14) define the dynamic conditions, whereas (4.12) is the kinematic condition, which will be used later on as a solvability equation. Carrying out the long wave approach, the variables are expanded in powers of ε: $(u,v,w,P) = (u^{(0)},v^{(0)},w^{(0)},P^{(0)}) + \varepsilon(u^{(1)},v^{(1)},w^{(1)},P^{(1)}) + O(\varepsilon^2)$. Moreover, We is considered of order ε^{-2}, in order to assure the validity of the boundary layer approximation and in agreement with experimental observations Kalliadasis et al. (2011) (e.g., $Re \sim 10^{-2}$ and $\vartheta = \pi/2 + \pi/10$ give $We \sim 10^6$).

Substituting the gradient expansion in the hydrodynamic problem (4.5)-(4.14), and collecting coefficients of like powers of ε, we obtain the problems at the different orders. At the leading order, the system reduces to

$$u^{(0)}_{yy} = -2, \qquad w^{(0)} = 0, \qquad v^{(0)}_{y} + u^{(0)}_{x} = 0, \tag{4.15}$$

$$P^{(0)}_{y} = -\zeta/Re, \qquad u^{(0)}|_{\eta} = 0, \qquad u^{(0)}_{y}|_{\eta+h} = 0, \tag{4.16}$$

$$v^{(0)}|_{\eta} = \eta_t, \qquad P^{(0)}|_{\eta+h} = -We[(h+\eta)_{xx} + (h+\eta)_{zz}], \tag{4.17}$$

with solutions

$$u^{(0)} = (y-\eta)(2h-y+\eta), \tag{4.18}$$

$$v^{(0)} = \eta_t - (y-\eta)[h_x(y-\eta) + \eta_x(-2h-\eta+y)], \tag{4.19}$$

$$w^{(0)} = 0, \tag{4.20}$$

$$P^{(0)} = Re^{-1}\zeta(h+\eta-y) - We[(h+\eta)_{zz} + (h+\eta)_{xx}], \tag{4.21}$$

At the order ε, the system reads

$$Re\,(u^{(0)}_{t} + P^{(0)}_{x} + u^{(0)}u^{(0)}_{x} + v^{(0)}u^{(0)}_{y}) = u^{(1)}_{yy}, \tag{4.22}$$

$$Re\,P^{(0)}_{z} = w^{(1)}_{yy}, \qquad u^{(1)}_{x} + v^{(1)}_{y} + w^{(1)}_{z} = 0, \tag{4.23}$$

$$u^{(1)}|_{\eta} = 0, \qquad u^{(1)}_{y}|_{h+\eta} = 0, \qquad w^{(1)}|_{\eta} = 0, \tag{4.24}$$

$$w^{(1)}_{1,y}|_{h+\eta} = 0, \qquad v^{(1)}|_{\eta} = 0, \tag{4.25}$$

whose solutions are cumbersome and reported in the Appendix C.1 for the sake of space. The solutions obtained for the flow field can now be substituted into the kinematic condition (4.12), which serves as solvability equation. To order ε, this leads to the first main equation of our analysis

$$h_t + 2h^2 h_x + \varepsilon\{\frac{8}{15}Re\left(h^6 h_x\right)_x + \nabla_{xz}\cdot[-\zeta\frac{h^3}{3}\nabla_{xz}(h+\eta) + ReWe\frac{h^3}{3}\nabla_{xz}\nabla^2_{xz}(h+\eta)]\} = 0. \tag{4.26}$$

If one fixes the bottom to be undeformable, namely $\eta = 0$, eq. (4.26) reduces to the standard Benney equation (Benney, 1966), with the effect of surface tension as firstly introduced by Gjevik (1970).

4.2.2 Wall evolution equation

In order to address the morphological instability, a second equation, uniquely for the wall evolution, is necessary. We firstly consider the ice environment, where the heat propagation determines melting-freezing processes at the interface. The disequilibrium in the heat fluxes is regulated by the so-called Stefan's equation

$$\rho_I \lambda_f \, \hat{\eta}_{\hat{t}} = [(K_I \nabla \hat{T}_I) - (K_w \nabla \hat{T}_w)] \cdot \mathbf{n}, \tag{4.27}$$

where $K_{i,w}$ and $\hat{T}_{w,i}$ are the thermal conductivity and the temperature for water and ice respectively, ρ_I is the ice density, λ_f the latent heat, $\mathbf{n}$ the versor normal to η and pointing in the water. The derivation of a more amenable form for eq. (4.27) is now briefly summarized, following Camporeale (2015). At first, the temperature can be decomposed into the sum of a base state plus a small pattern-induced perturbation $\hat{T}_{w,I} = \hat{T}^0_{w,I}(\hat{z}) + \zeta \hat{T}^1_{w,I}(\hat{x},\hat{y},\hat{z})$. Then, another normalized coordinate is introduced $\xi_I = (\hat{y} - \hat{\eta})/(\hat{b} + \hat{\eta})$ in order to rectangularize also the solid domain, being $\hat{b}$ an assigned depth in the ice. Hence, both liquid and solid domains are rectangularized, $\xi_w \in [0,1]$ and $\xi_I \in [-1,0]$ respectively. In this way, the base state for the temperature is linearly distributed over the depth

$$\hat{T}^0_w = \hat{T}_\infty \xi_w, \qquad\qquad \hat{T}^0_I = \hat{T}_b \xi_I, \tag{4.28}$$

where $\hat{T}_{\infty,b}$ are the temperature at the free surface and at $\hat{y} = -\hat{b}$, respectively. Due to the very low Reynolds numbers, thermal convection can be neglected in the heat equation for the liquid phase. Thus, $\hat{T}$ satisfies the Laplace equation $\nabla^2 \hat{T} = 0$ in both domains. Using the normalized coordinates and Fourier-transforming from $(\hat{x},\hat{z})$ to the horizontal two-dimensional wavenumber $\tilde{K}$, the diffusive thermal problem at first order in ζ becomes

$$\hat{T}^{1,*}_{\xi\xi} - \hat{h}_0^2 \tilde{K}^2 \hat{T}^{1,*} + \hat{h}_0 \tilde{K}^2 \hat{T}_\infty (\hat{\eta}^*_1 + \xi \hat{h}^*_1) = 0 \qquad \text{Water} \tag{4.29}$$

$$\hat{T}^{1,*}_{\xi\xi} - \hat{b}^2 \tilde{K}^2 \hat{T}^{1,*} + \hat{\eta}^*_1 \hat{b} \tilde{K}^2 \hat{T}_b (1+\xi) = 0 \qquad \text{Ice} \tag{4.30}$$

where here * refers to the Fourier transform, $\hat{h}$ and $\hat{\eta}$ have been decomposed into the sum of a basic state and a small local perturbation, i.e., $\hat{h} = \hat{h}_0 + \zeta \hat{h}_1$ and $\hat{\eta} = \hat{\eta}_0 + \zeta \hat{\eta}_1$. The boundary conditions for (4.29)-(4.30) ensure melting temperature

at the liquid-solid interface and continuity of the heat flux throughout the domain

$$\hat{T}^{1,*} = \hat{T}^{1,*}_{\xi}|_{\xi=1} = 0. \tag{4.31}$$

Solving the problems (4.29)-(4.31) and substituting in (4.27), at first order in ζ, yields

$$\rho_I \lambda_f \left(\hat{\eta}_0 + \zeta \hat{\eta}_1\right)_{\hat{t}} = \hat{I}_I - \hat{I}_w + \zeta \left(\frac{\hat{h}_1}{\hat{h}_0}\hat{I}_w - \frac{\hat{\eta}_1}{\hat{b}}\hat{I}_I - \frac{\tilde{K}^2}{2}\mathscr{P} \right) \tag{4.32}$$

where $\mathscr{P} = \left[(2\hat{\eta}_1 + \hat{h}_1)K_w\hat{T}_\infty + \hat{\eta}_1\kappa_I\hat{T}_b\right]$, $\hat{I}_I = K_I\hat{T}_b/\hat{b}$, $\hat{I}_w = K_w\hat{T}_\infty/\hat{h}_0$. The third term in the brackets of (4.32) is a diffusive term whose numerical influence we have verified being negligible. Without considering the perturbations, the liquid-solid interface rigidly translates due to a freezing/melting process. Both experimentally and in field observation, measuring a uniform vertical translation of the interface might be a simpler task than evaluating the temperature at an assigned depth in the ice (Camporeale et al., 2017). Thus, for assigned values of the air temperature, the ice depth and the translation rate, $\hat{\eta}_0 = \bar{V}_I\hat{t}$, from (4.32) it follows

$$\hat{T}_b = (\rho_I\lambda_f\bar{V}_I + \hat{I}_w)\frac{\hat{b}}{K_I}. \tag{4.33}$$

Notice that $\hat{T}_b$ is defined as positive in order to have a negative temperature at $\hat{y} = -\hat{b}$, see eq. (4.28). Substituting expression (4.33) in eq. (4.32) yields

$$\hat{\eta}_t = \bar{V}_I + (\hat{h} - \hat{h}_0)\hat{B}_I - (\hat{\eta} - \bar{V}_I\hat{t})\hat{B}_I/b, \tag{4.34}$$

where $\hat{B}_I = \hat{I}_w/(\rho_I\lambda_f\hat{h}_0)$, $b = \hat{b}/\hat{h}_0$ and $\bar{V}_I \ll \hat{B}_I\hat{h}_0$.

In the karst context, the precipitation-dissolution processes of calcium carbonate are able to shape multitudinous speleothems. In particular, the evolution of the liquid-solid interface is driven by reactions that can be stoichiometrically summarised as (Romanov et al., 2008)

$$CaCO_3 + CO_2 + H_2O \rightleftharpoons Ca^{++} + 2HCO_3^- . \tag{4.35}$$

From (4.35), one can notice that for each molecule of $CaCO_3$ depositing on the solid surface, there is a molecule of CO_2 diffusing into the atmosphere. This is the key principle of the equation derived by Short et al. (2005), as briefly summarized

below. Let us start from the slowest chemical reactions involved in the growth of speleothems, that are those coupling carbon dioxide to bicarbonate

$$CO_2 + H_2O \overset{k_{\pm 1}}{\rightleftharpoons} H^+ + HCO_3^-, \tag{4.36}$$

$$CO_2 + OH^- \overset{k_{\pm 2}}{\rightleftharpoons} HCO_3^-. \tag{4.37}$$

From (4.36) and (4.37), the production rate of CO_2 can be written as

$$R_{CO_2} = k_-[HCO_3^-] - k_+[CO_2], \tag{4.38}$$

where the square brackets refer to concentrations and

$$k_- = k_{-1}[H^+] + k_{-2}, \qquad k_+ = k_{+1} + k_{+2}[OH^-]. \tag{4.39}$$

To evaluate carbon dioxide dynamics, a full reaction-diffusion equation for $[CO_2]$ within the fluid layer is considered. Then, some assumptions are introduced: i) the concentrations of the other chemical species are almost constant over the film, ii) the longitudinal and transversal diffusion and advection of CO_2 are negligible, iii) $[CO_2] = \mathscr{H}\hat{C}_\infty(1 + c_1(x,\xi,z,t))$, where $\mathscr{H}$ is Henry's constant, $\hat{C}_\infty$ is the far atmospheric carbon dioxide concentration and ξ is the normalized coordinate that rectangularizes the fluid domain, i.e., $\xi = (\hat{y} - \hat{\eta})/\hat{h}$. In these conditions, the dimensionless reaction-diffusion equation for $[CO_2]$ reads

$$c_{1,\xi\xi} = h^2\varpi(c_1 - \mathscr{U}), \tag{4.40}$$

where

$$\varpi = \frac{k_+\hat{h}_0^2}{D_{CO2}}, \qquad \mathscr{U} = \frac{k_-[HCO_3^-]}{k_+\mathscr{H}\hat{C}_\infty} - 1, \tag{4.41}$$

being D_{CO2} the carbon dioxide diffusivity in water. The two boundary conditions for eq. (4.40) ensure zero flux of carbon dioxide at the solid interface and flux continuity between the fluid and the atmosphere. Because of the latter condition, the solution of eq. (4.40) depends on the atmospheric carbon dioxide field $\hat{C}_{CO_2}$, that satisfies the Laplace equation. In cylindrical coordinates, it reads $\hat{C}_{CO_2} = \hat{C}_\infty + A/\hat{r}$ being $\hat{r}$ the dimensional distance from the center of the stalactite. Although in our case the base state geometry is planar, in (Short et al., 2005) it was demonstrated the irrelevance

of the geometry considered to the final result. For this reason, as done in (Short et al., 2005), the more amenable cylindrical coordinates for the Laplace equation are adopted. It follows that

$$\hat{c}_1|_{\xi=1} = \frac{A}{\hat{R}_s \hat{C}_\infty}, \qquad \hat{F} = \frac{D_a A}{\hat{R}_s^2} = -\frac{D_{CO2}\mathscr{H} C_\infty}{\hat{R}_s} c_{1,\xi}|_{\xi=1}, \tag{4.42}$$

where $\hat{R}_s$ represents the radius of the stalactite ($\hat{R}_s \gg \hat{h}$), $\hat{F}$ is the dimensional flux of carbon dioxide leaving the film into the atmosphere (calculated through Fick law) and D_a is the diffusivity of CO_2 in air. Eliminating the constant A from (4.42), the two boundary conditions are eventually achieved

$$\hat{c}_{1,\xi}|_{\xi=0} = 0, \qquad \hat{c}_{1,\xi}|_{\xi=1} = -\frac{\hat{h} D_a}{\hat{R}_s \mathscr{H} D_{CO2}} \hat{c}_1|_{\xi=1}. \tag{4.43}$$

Recalling that $\varpi \ll 1$, a solution of the problem (4.40)-(4.43) to the lowest order in ϖ reads

$$\hat{c}_1 = \varpi \hat{h}^2 \mathscr{U} \left(\frac{1-\xi^2}{2} + \frac{\mathscr{H} D_{CO2} \hat{R}_s}{D_a \hat{h}} \right). \tag{4.44}$$

At this point, it is sufficient to equal the total flux of CO_2 leaving the fluid by the free surface to the total flux of $CaCO_3$ depositing on the solid wall. The result reads

$$\hat{F}_{\mathrm{CaCO_3}} = \rho_c \, \hat{\eta}_{\hat{t}} = \hat{h} \left(k_- [\mathrm{HCO_3^-}] - k_+ \mathscr{H} \hat{C}_\infty \right), \tag{4.45}$$

where ρ_c is the ratio of molar mass to density of calcite. Due to the assumptions previously made, the whole content of the brackets in eq. (4.45), denoted as $\rho_c \hat{B}_K$, can be considered independent of hydrodynamics. Thus, eq. (4.45) reduces to

$$\hat{\eta}_{\hat{t}} = \hat{h} \hat{B}_K. \tag{4.46}$$

Similarly to the ice case, even in not-perturbed conditions the liquid-solid interface undergoes a vertical translation ($\bar{V}_K = \hat{h}_0 \hat{B}_K$) due the precipitation of $CaCO_3$ contained in the liquid film.

Eventually, the corresponding dimensionless evolution equations of (4.34)-(4.46) read

$$\eta_t = \bar{v}_I + (h-1)/\gamma_I - (\eta - \bar{v}_I t)/(\gamma_I b) \qquad \text{Ice} \qquad (4.47a)$$

$$\eta_t = \bar{v}_K + (h-1)/\gamma_K \qquad \text{Karst} \qquad (4.47b)$$

where $\gamma_{I,K} = \hat{u}_0/(B_{I,K}\hat{h}_0)$ is the ratio of the morphological to hydrodynamic time scale. The equations become equivalent for $b \to \infty$. Assuming $\hat{T}_s = 0.01$°C, $\hat{b} = 0.5$ m, $\bar{V}_I = 4$ cm/d for the ice case and standard conditions for speleothem formation (Short et al., 2005) one obtains

$$\gamma_I \sim 10^4 Re, \qquad \gamma_K = \frac{\hat{u}_0}{\hat{c}}, \qquad (4.48)$$

where $\bar{V}_K$ is the average velocity of speleothem formation (henceforth $\bar{V}_K = 5$ cm/century). Expressions (4.48) furnish γ_I of order 10^2 and γ_K of order 10^7 or larger. In fact, karst flutings evolve much slower than their ice counterpart. To sum up, the dimensionless differential system for fluting formation is provided by the two equations accounting for the free surface and bottom evolution, namely (4.26) and (4.47).

4.3 Linear stability analysis

4.3.1 2D analysis

With the aim of addressing a linear stability analysis, the vector of the state variables $\mathbf{U} = (h, \eta)$ is recast as the sum of the base state $\mathbf{U}_0$ and a small perturbation $\mathbf{U}_1$ as follows:

$$\mathbf{U} = \mathbf{U}_0 + \mathbf{U}_1 = (1, \bar{v}_{I,K} t) + (H, \Theta)\, \mathrm{e}^{\mathrm{i}\tilde{k}x + \mathrm{i}kz + \Omega t}, \qquad (4.49)$$

where $\tilde{k}$ and k are the longitudinal and transversal wavenumbers, respectively; the real part of Ω determines the growth rate, while its imaginary part stands for the angular phase. By substituting (4.49) into equations (4.26) and (4.47) and linearising we obtain

$$\mathbf{L}_{I,K} \cdot \mathbf{U}_1 = 0. \qquad (4.50)$$

where the matrices $\mathbf{L}_{I,K}$ are reported in the Appendix C.2. After imposing the determinant of the matrices equal to zero, the dispersion relation are obtained

$$f_{I,K}(\Omega, \tilde{k}, k, \zeta, \gamma, Re, We) = 0, \tag{4.51}$$

whose solutions $\Omega_{1,2}$ are the corresponding eigenvalues of the algebraic linear system (4.50). Both f and the eigenvalues $\Omega_{1,2}$ are reported in Appendix C.2 for the karst and the ice cases. Although the two problems are slightly different due to eqs. (4.47), the same considerations hold for both environments. This is due to the fact that the dynamics is driven by the hydrodynamics (Camporeale, 2015).

The control parameters in the system are apparently three: ζ, Re and We. However, through the definition of the Weber number and eqs. (4.1), We can be recast in a form involving its dependence on ζ and Re, as done for example in (Lin and Kondic, 2010). This leads to

$$We = \frac{Ka}{(\sin\vartheta Re^5)^{1/3}} \tag{4.52}$$

where $Ka = \sigma/(\rho g^{1/3}\nu^{4/3})$ is the Kapitza number, that depends only on the fluid properties and it is thus constant for our purpose. Eq. (4.52) reduces the effective control parameters to two: Re and ζ. Fixing an overhanging wall, one may evaluate the eigenvalues behaviours with respect to different values of Re.

Fig. 4.3 shows the growth rate Ω_2^r in the wavenumbers plane (while Ω_1^r is always negative). For sufficiently small Re, the absolute maximum of Ω_2^r lays on the k axis ($\tilde{k}=0$), panel a_1. Therefore, the fastest growing mode is associated with a transverse perturbation, i.e., flutings. There is also a relative maximum on the $\tilde{k}$ axis, but its value is smaller, as reported in panel a_2. Instead, increasing Re, the longitudinal maximum on the $\tilde{k}$ axis ($k=0$) exceeds the transverse one, see panels b_1 and b_2. In addition, in panel b_2 it is also furnished Ω_2^r under the Stokes approximation (red dotted line). Due to the relatively high values of Re, the lack of the convective terms jeopardizes the correct boundary of the ripple-fluting transition. Instead in panel a_2, where Re is smaller, the computation of Ω_2^r is less by the Stokes approximation. Hence, although fluting formation could be modelled using the Stokes approximation, it would be impossible to correctly define the margin between the fluting and ripple regimes.

In order to differentiate these two regimes, the transition Reynolds number Re_t below which flutings develop is evaluated with respect to the deviation from the

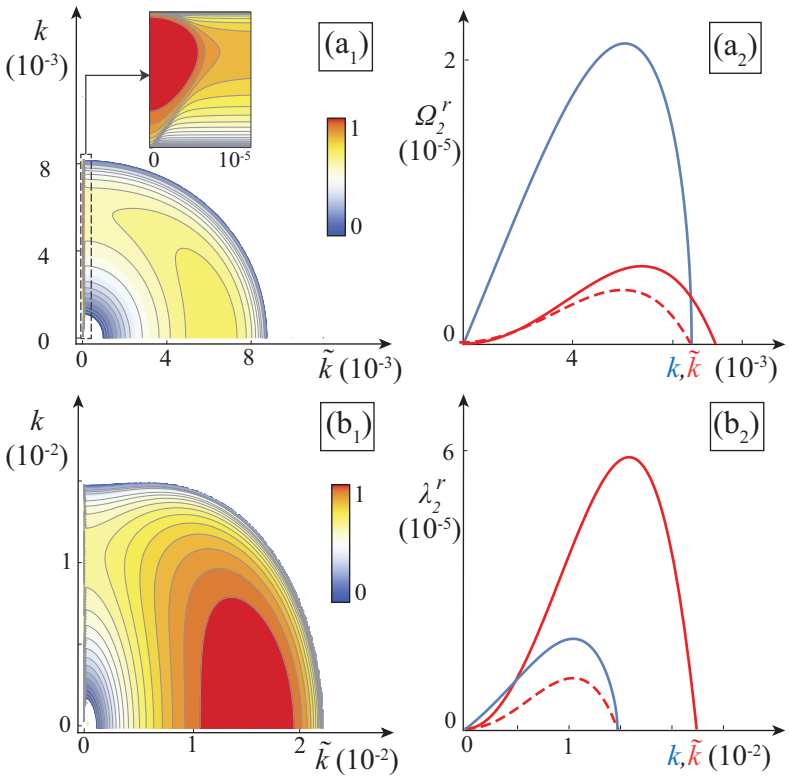

Fig. 4.3 Analysis of the growth rate Ω_2^r from the 2D dispersion relation (ice case and $\vartheta = \pi/2 + \pi/9$). ($a_1$) Normalized contour plot of Ω_2^r for $Re = 0.1$. The maximum lays on the k axis, therefore flutings develop. (a_2) Comparison of Ω_2^r on the k and $\tilde{k}$ axes. (b_1) Normalized contour plot of Ω_2^r for $Re = 0.6$. The maximum lays on the $\tilde{k}$ axis, therefore ripples develop. (b_2) Comparison of Ω_2^r on the k and $\tilde{k}$ axes. The red dotted line is the solution under the Stokes approximation, that is not adequate to reveal the ripple regime.

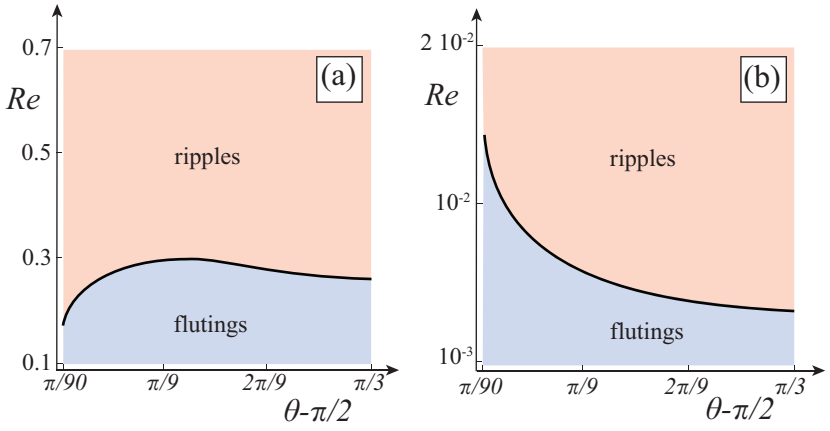

Fig. 4.4 Transition Reynolds number discriminating fluting and ripple regimes. Ice case (a) and karst case (b).

vertical $\vartheta - \pi/2$ (Fig. 4.4). It turns out that it is $O(10^{-1})$ for the ice case and $O(10^{-2})$ for the karst case.

In overall, for fluting formation ($Re < Re_t$), we can consider only the span-wise perturbation and thus develop a more parsimonious model.

4.3.2 1D analysis

The previous section has demonstrated that for low Reynolds numbers, i.e., $Re < Re_t$, the fastest growing mode is associated with a span-wise perturbation. Therefore, we can introduce a normal mode ansatz with only transversal dependency

$$\mathbf{U} = \mathbf{U}_0 + \mathbf{U}_1 = (1, \bar{v}_{I,K}\, t) + \zeta\,(H, \Theta)\, \mathrm{e}^{\mathrm{i}kz+\omega t}, \tag{4.53}$$

where the notation for the time dependency has been switched to ω in order to discriminate from the eigenvalues Ω of Sec. 4.3.1. Hence, the real part of ω determines the growth rate, while its imaginary part stands for the angular phase. By substituting (4.53) into equations (4.26) and (4.47) and linearising we obtain

$$\begin{pmatrix} \Gamma+\omega & \Gamma \\ -\frac{1}{\gamma} & a_{I,K} \end{pmatrix} \cdot \begin{pmatrix} H \\ \Theta \end{pmatrix} = 0. \tag{4.54}$$

where $\Gamma = k^2(ReWek^2 + \zeta)/3$, $a_I = \omega + 1/(b\gamma)$ and $a_K = \omega$. After imposing the determinant of the matrix equal to zero, the dispersion relations are obtained

$$(\Gamma + \omega)(\omega + \frac{1}{b\gamma}) + \frac{\Gamma}{\gamma} = 0, \qquad (I) \tag{4.55a}$$

$$\Gamma(\gamma\omega + 1) + \omega^2\gamma = 0, \qquad (K) \tag{4.55b}$$

whose solutions, corresponding to the eigenvalues of the algebraic linear system (4.54), are

$$(\omega_{1,2})_I = -\left(\frac{\Gamma}{2} + \frac{1}{2r\gamma}\right)\left(1 \pm \sqrt{1 - \frac{4r\gamma\beta(b+1)}{(b\gamma\beta+1)^2}}\right) \tag{4.56a}$$

$$(\omega_{1,2})_K = -\frac{\Gamma}{2}\left(1 \pm \sqrt{1 - \frac{4}{\gamma\beta}}\right) \tag{4.56b}$$

The eigenvalues (4.56) are real in the domain of instability, therefore flutings do not laterally migrate, and they become complex conjugate in the domain of stability, i.e. there is not a preferential direction for the decay of the perturbation. This is a consequence of the transversal invariance of the problem and it shows that the above mathematical setting is well-posed. Referring to ω_2 as the eigenvalues with the minus in front of the square root, it can be shown that ω_2 is always negative, while in some parameter conditions, ω_1 becomes positive and thus flutings develop.

Due to eq. (4.52), the two control parameters for the growth rate ω_1 are: ϑ and Re. When Re is kept constant, by setting $\omega_1 = 0$, the neutral stability curves in the (k, ϑ) plane are obtained, as reported in Fig. 4.5a. The curves show that flutings develop when $\vartheta > \pi/2$ (so-called *inverted condition*). On the other hand, when ϑ is fixed at a particular value larger than $\pi/2$ and Re is variable, the neutral stability curves in the parameter plane (k, Re) start from the origin (Fig. 4.5b), that is all Reynolds number are unstable.

In Fig. 4.5c, the behaviour of ω_1 versus k is reported for different angles ϑ. It is interesting to highlight the main differences with bar instability in Chapter 2 (in particular see Fig. 2.2c).
At critical conditions for bar formation ($\beta = \beta_c$), the neutral wavenumber k_c has a finite value. While at critical conditions for fluting formation ($\vartheta = \pi/2$), the neutral wavenumber is null[1]. This classifies flutings as a long-wave instability (as all instabilities involving liquid films (Kalliadasis et al., 2011)). In long-wave instabilities, $k = 0$ is the mode associated with a homogeneous change of the base state (the so-called Goldstone mode in condensed matter physics). However, a homogeneous change of the base state is only possible through a change in the flow rate, which is fixed in the present analysis. Indeed, the Goldstone mode is a mathematical artefact, that is removed by finite-size effects (finite length of the channel) in the physical reality.
Another difference with bar instability is that, in unstable conditions for flutings ($\vartheta > \pi/2$), the range of unstable wavenumbers spans from zero ($k = [0, \sqrt{-\zeta/(ReWe)}]$). This means that the low modes and the subharmonics of the fundamental are linearly unstable and can destabilise the fundamental mode (the following nonlinear analysis will show that this does not happen).

[1] Fluting instability corresponds to the type II-stationary instability of the classification suggested by Cross and Hohenberg (1993).

Interestingly, although the analytical relations for ω_1 are different in the two environments, the cutoff wavenumber remains the same. This is due to the fact that the dynamics is driven by the water film, that acts similarly in both cases. Analogously, the selected wavenumber, which corresponds to the fastest growing mode, reads $k_s = \sqrt{-\zeta/(2ReWe)}$ for both environments. By recalling eqs. (4.1) and (4.52), the corresponding dimensional wavelength reads

$$\hat{L} = \frac{2\pi\hat{h}_0}{k_s} = \pi\hat{l}_c\sqrt{-8\sec\vartheta}, \tag{4.57}$$

where $\hat{l}_c = \sqrt{\sigma/\rho g}$ is the capillary length (recall that $\vartheta > \pi/2$). This result is quite peculiar because it shows that $\hat{L}$ does not depend on the hydrodynamics ($\hat{q}$), but only on the fluid properties (ρ,σ) and the geometry (ϑ). In Fig. 4.5d the behaviour of $\hat{L}$ versus the slope is reported.

The present results agree with the outcomes of the theory developed in (Camporeale, 2015), where a y-dependent differential eigenvalue problem was solved with the aid of the Stokes approximation. The present approach of the gradient expansion circumvents the Stokes approximation and it is more suitable for further weakly nonlinear analyses, since the equation are provided in a one-dimensional form, where the y-dependence has been explicitly solved (see eqs. (4.18)-(4.21) and Appendix C.1).

4.4 Nonlinear stability analysis

In this section, a weakly nonlinear analysis is performed through the technique of the center-unstable manifold projection. The aim is to provide an analytical solution for the finite amplitude of the fundamental mode. However, it is well-known that solving the amplitude equation for the fundamental mode is sometimes not sufficient. In fact, when nonlinearities are in play, the linear modes are not any longer decoupled, hence finite-amplitude monochromatic waves may be destabilized by nonlinear interactions with other modes satisfying the so-called resonance condition (Cheng and Chang, 1990). In the case of quadratic non-linearities, this condition reads: $k_l \pm k_p = k_m$, where k_m refers to the mode whose dynamic is in question and k_l and k_p are all possible modes that contribute to the dynamics of k_m. Although the fundamental k_m could be potentially unstable to any wavenumber (i.e., infinite

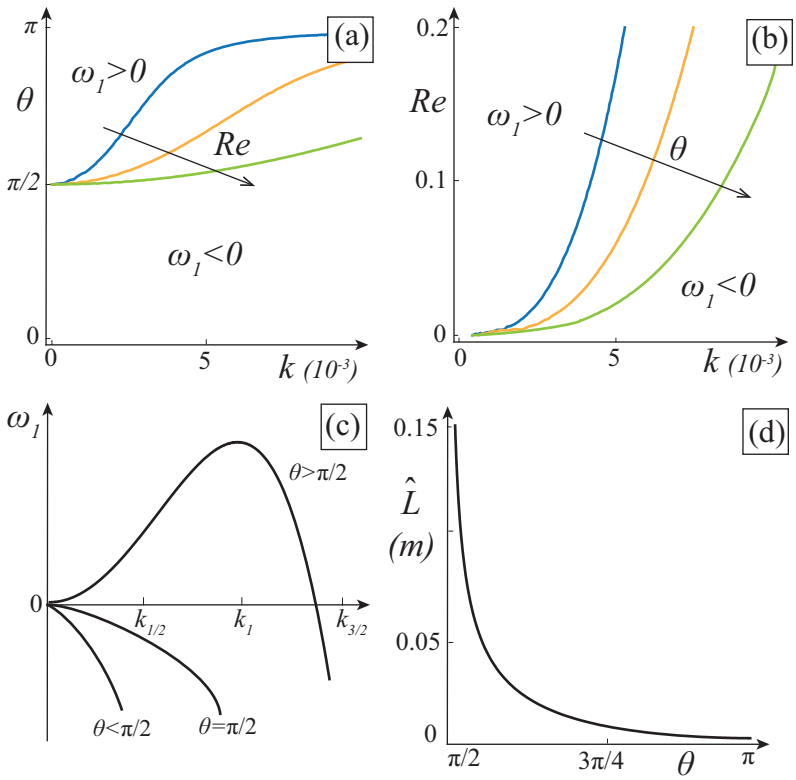

Fig. 4.5 Results of the linear stability analysis. (a) Neutral stability curves for the ice case with ϑ as control parameter ($Re = 10^{-1}, 10^{-2}, 10^{-3}$). The instability is triggered at inverted conditions ($\vartheta > \pi/2$). (b) Neutral stability curves for the ice case with Re as control parameter ($\vartheta - \pi/2 = \pi/36, \pi/18, \pi/9$). The plots for the karst case are qualitatively similar, with Re spanning between 10^{-4} and 10^{-6}. (c) Typical behavior of the eigenvalue ω_1 versus the wavenumber k. (d) Dimensional wavelength of flutings versus the angle with the horizontal ϑ.

combination of k_l and k_p), it is far simpler to derive stability criteria for disturbances of specific wavenumbers, if these disturbances are observed to be the dominant ones from physical observations. Concerning non-inverted falling films, experimental and theoretical works (Brauner and Maron, 1982; Cheng and Chang, 1995; Liu and Gollub, 1993) have shown that, depending on the frequency of the fundamental, a subharmonic or a sideband instability is triggered. Moreover, previous analyses on open-flow systems, with long-wave instabilities as ours (Kelly, 1967; Monkewitz, 1988; Prokopiou et al., 1991), have found instability to subharmonic disturbances. However, we point out that differently from these last works, in our system the modulation is not in the direction of the driving force, but it is transversal to it, see section 4.3.2. Definitely, it can be noticed that in our system the range of unstable wavenumbers spans from zero to $\sqrt{-\zeta/(ReWe)}$, see Fig. 4.5c. Hence, the 1/2 subharmonic of any wave within this range is linearly unstable, including the subharmonic of the fundamental, i.e., $k = k_s$, while the 3/2 subharmonic of the fundamental is stable. We will prove that, although the subharmonic of the fundamental is linearly unstable, the rising effect of the non-linearities may allow the fundamental to saturate and the subharmonic to decay.

4.4.1 Center-unstable manifold projection

The center-unstable manifold projection does not stipulate that the unstable modes are nearly neutral, the only stipulation is that their amplitudes are small. This approach is sometimes known as the invariant manifold expansion (Roberts, 1989), since the growth rates of the unstable modes are not expanded near the point where they vanish exactly at the neutral curve. Considering second order non-linearities, system (4.26)-(4.47) with the ansatz (4.53) can be written as

$$\mathbf{U}_{1,t} = \mathscr{L}\mathbf{U}_1 + \mathbf{N}(\mathbf{U}_1) + o(\mathbf{U}_1^2), \tag{4.58}$$

where $\mathscr{L}$ is the differential operator associated with the linear system and $\mathbf{N}(\mathbf{U}_1)$ contains all second order non-linearities. The linear eigenvalue problem associated with (4.58) states

$$\mathbf{L}\mathbf{f}_m = \omega_m \mathbf{f}_m, \tag{4.59}$$

where ω_m are the two eigenvalues reported in (4.56) and $\mathbf{f}_m$ are the correspondent eigenfunctions. The system is invariant to translation in z, therefore the linear

problem may be Fourier transformed as follows

$$\mathbf{f}_m(z) = \mathbf{v}_m(k)\,\mathrm{e}^{\mathrm{i}kz}. \tag{4.60}$$

Substituting (4.60) into (4.59) yields the projected eigenvalue problem

$$\mathbf{L}(k)\mathbf{v}_m(k) = \omega_m(k)\mathbf{v}_m(k), \tag{4.61}$$

where $\mathbf{L}$ is the same matrix appearing in (4.54). The corresponding adjoint eigenvalue problem reads

$$\mathbf{L}^\dagger \mathbf{v}_m^\dagger = \omega_m^* \mathbf{v}_m^\dagger, \tag{4.62}$$

where star * refers to complex conjugate, while the symbol † stands for the adjoint (the dependence on k has been considered implicitly). We remind that $\mathbf{L}^\dagger$ is defined by $(\mathbf{L}\,\mathbf{x})\cdot\mathbf{y}^* = \mathbf{x}\cdot(\mathbf{L}^\dagger\mathbf{y})^*$ and, because $\mathbf{L}$ has only real elements, its adjoint is simply the transpose, i.e., $\mathbf{L}^\dagger = \mathbf{L}^T$. After proper normalization, the eigenvectors $\mathbf{v}_i$ and the adjoint eigenvectors $\mathbf{v}^\dagger$ are orthonormal with respect to the dot product

$$\mathbf{v}_i \cdot \mathbf{v}_j^\dagger = \delta_{ij}. \tag{4.63}$$

The fundamental mode $\omega_1(k)$ and its subharmonic $\omega_1(k/2)$ are the only possible unstable modes, while all other subharmonic or superharmonic modes are stable. The perturbation $\mathbf{U}_1$ can be expanded in terms of the eigenfunctions $\mathbf{f}_m$ given by (4.60)

$$\mathbf{U}_1(z,t) = \sum_{p=-\infty}^{+\infty} \sum_{m=1}^{2} A_{[m,\frac{p}{2}]}(t)\mathbf{v}_m\left(\frac{pk}{2}\right)\exp\left(\frac{\mathrm{i}\,pkz}{2}\right), \tag{4.64}$$

where m and p are integer numbers and $A_{[m,\frac{p}{2}]}$ is the $p/2$ subharmonic associated with the eigenvalue m (we point out that eq. (4.64) also takes into account the complex conjugate amplitudes as $A^*_{[m,\frac{p}{2}]} = A_{[m,-\frac{p}{2}]}$). Notice that, with respect to the Fourier sum in the bar problem (2.20), we here consider the subharmonic modes $p/2$. Substituting (4.64) into (4.58), taking the dot product with the adjoint eigenfunctions and collecting the terms of the same Fourier modes, yields the equations for the two

unstable modes

$$\dot{A}_1 = \omega_1(k)A_1 + P_1 A_{\frac{1}{2}}^2 + P_2^{(1)} A_{\frac{1}{2}} A_{[2,\frac{1}{2}]} + P_2 A_{\frac{1}{2}}^* A_{[1,\frac{3}{2}]} + P_2^{(2)} A_{[2,\frac{1}{2}]}^* A_{[1,\frac{3}{2}]} + P_2^{(3)} A_{\frac{1}{2}}^* A_{[2,\frac{3}{2}]} + \sum_{m=1}^{2} P_m^{(4)} A_1^* A_{[m,2]}, \quad (4.65a)$$

$$\dot{A}_{\frac{1}{2}} = \omega_1(k/2)\, A_{\frac{1}{2}} + P_3 A_{\frac{1}{2}}^* A_1 + P_2^{(6)} A_{[2,\frac{1}{2}]}^* A_1 + P_2^{(7)} A_{\frac{1}{2}}^* A_{[2,1]} + P_4 A_1^* A_{[1,\frac{3}{2}]} + P_2^{(8)} A_{[2,1]}^* A_{[1,\frac{3}{2}]} + P_2^{(9)} A_1^* A_{[2,\frac{3}{2}]} + \sum_{m=1}^{2} P_m^{(10)} A_{[1,\frac{3}{2}]}^* A_{[m,2]}, \quad (4.65b)$$

where we have posed $A_{1,1} = A_1$ and $A_{1,\frac{1}{2}} = A_{\frac{1}{2}}$. Instead, the corresponding amplitude equations for the stable modes read

$$\dot{A}_{[2,\frac{1}{2}]} = \omega_2(k/2)A_{[2,\frac{1}{2}]} + S_2^{(1)} A_{\frac{1}{2}}^* A_1 + \cdots, \quad (4.66a)$$

$$\dot{A}_{[2,1]} = \omega_2(k/2)A_{[2,1]} + S_2^{(3)} A_{\frac{1}{2}}^2 + \cdots, \quad (4.66b)$$

$$\dot{A}_{[m,\frac{3}{2}]} = \omega_m(3k/2)A_{[m,\frac{3}{2}]} + S_m^{(5)} A_{\frac{1}{2}} A_1 + \cdots, \quad (4.66c)$$

$$\dot{A}_{[m,2]} = \omega_m(2k)A_{[m,2]} + S_m^{(6)} A_1^2 + \cdots. \quad (4.66d)$$

Eqs. (4.65)-(4.66) represent a Galerkin-type projection of the full equations truncated at the second order non-linearities. Dots in the right hand side of eq. (4.66) refer to omitted quadratic terms involving interactions of the stable modes, while the derivation of all coefficients appearing in the present analysis, e.g., $P_m^{(m)}$ and $S_i^{(n)}$ from (4.65)-(4.66), is reported in the Appendix C.3 and partially follows the nomenclature introduced by (Cheng and Chang, 1992).

At this point, the center-unstable manifold theory allows the amplitudes of the stable modes to be projected onto the unstable ones, so that any $A_{[m,p]}$ in (4.66) is recast as a non-linear combination of the neutral modes $A_1, A_{1/2}$ and their complex conjugate to $O(2)$. The procedure is analogous to the one presented in Sec. 2.2.5, but we here represent it as the number of modes involved is higher. Let us consider, for instance, the stable mode $A_{[2,\frac{1}{2}]} = E(A_1, A_{\frac{1}{2}}, A_1^*, A_{\frac{1}{2}}^*)$, where E represents an approximation of the unstable invariant manifold and it is defined as a power series

expansions to $O(2)$ of A_1 and $A_{\frac{1}{2}}$ with unknown coefficients, namely

$$E = aA_1^2 + bA_{\frac{1}{2}}^2 + cA_1^{*2} + dA_{\frac{1}{2}}^{*2} + eA_{\frac{1}{2}}A_1 + fA_{\frac{1}{2}}^*A_1 + gA_{\frac{1}{2}}A_1^* + hA_{\frac{1}{2}}^*A_1^*. \quad (4.67)$$

Hence, the temporal derivative of the stable modes $A_{[2,\frac{1}{2}]}$ reads

$$\dot{A}_{[2,\frac{1}{2}]} = \frac{\partial E}{\partial A_1}\dot{A}_1 + \frac{\partial E}{\partial A_{\frac{1}{2}}}\dot{A}_{\frac{1}{2}} + \frac{\partial E}{\partial A_1^*}\dot{A}_1^* + \frac{\partial E}{\partial A_{\frac{1}{2}}^*}\dot{A}_{\frac{1}{2}}^*. \quad (4.68)$$

Substituting eqs. (4.65)-(4.66a) and (4.67) in eq. (4.68), keeping only leading order terms and collecting like powers of $A_1, A_{\frac{1}{2}}, A_1^*, A_{\frac{1}{2}}^*$ yields

$$\begin{aligned} &a\,[2\omega_1(k) - \omega_2(k/2)]A_1^2 + b\,\omega_2(k/2)A_{\frac{1}{2}}^2 + g\,\omega_1^*(k)A_1^*A_{\frac{1}{2}} + \\ &\quad c\,[2\omega_1^*(k) - \omega_2(k/2)]A_1^{*2} + d\,[2\omega_1^*(k/2) - \omega_2(k/2)]A_{\frac{1}{2}}^{*2} + \\ &\quad e\,\omega_1(k)A_1A_{\frac{1}{2}} + h\,[\omega_1^*(k) + \omega_1^*(k/2) - \omega_2(k/2)]A_1^*A_{\frac{1}{2}}^* + \\ &\quad \{-S_2^{(1)} + f\,[\omega_1^*(k/2) + \omega_1(k) - \omega_2(k/2)]\}A_1A_{\frac{1}{2}}^* = 0. \end{aligned} \quad (4.69)$$

A solution to (4.69) is made by imposing all null coefficients except f, which reads

$$f = -\frac{S_2^{(1)}}{\omega_2(k/2) - \omega_1(k/2) - \omega_1(k)} = Z_2^{(1)}, \quad (4.70)$$

reminding that $\omega_1^* = \omega_1$. Repeating the same procedure for every stable amplitude of interest yields

$$\begin{aligned} A_{[2,\frac{1}{2}]} &\sim Z_2^{(1)}A_{\frac{1}{2}}^*A_1, & A_{[2,1]} &\sim Z_2^{(3)}A_{\frac{1}{2}}^2, \\ A_{[m,\frac{3}{2}]} &\sim Z_m^{(5)}A_{\frac{1}{2}}A_1, & A_{[m,2]} &\sim Z_m^{(6)}A_1^2. \end{aligned} \quad (4.71)$$

After substituting (4.71) into (4.65), the ultimate master amplitude equations for 1/2 subharmonic instabilities of quadratic systems with translational invariance in z and t are obtained

$$\dot{A}_1 = \omega_1A_1 + P_1A_{\frac{1}{2}}^2 + \tilde{G}_2|A_{\frac{1}{2}}|^2A_1 + G_1|A_1|^2A_1, \quad (4.72)$$

$$\dot{A}_{\frac{1}{2}} = \omega_{\frac{1}{2}}A_{\frac{1}{2}} + P_3A_{\frac{1}{2}}A_1 + \tilde{G}_5|A_1|^2A_{\frac{1}{2}} + G_6|A_{\frac{1}{2}}|^2A_{\frac{1}{2}}, \quad (4.73)$$

where $\omega_1 = \omega_1(k)$ and $\omega_{\frac{1}{2}} = \omega_1(k/2)$.

4.4.2 Stuart-Landau equation

The Stuart-Landau equation describes the dynamic of the fundamental without considering the influences of the other potentially destabilising modes. Therefore, it is readily obtained by neglecting the terms involving $A_{\frac{1}{2}}$ in (4.72)

$$\dot{A}_1 = (\omega_1 + \Xi\,|A_1|^2)A_1, \tag{4.74}$$

where both coefficients ω_1 and Ξ are real in the domain of instability, i.e., flutings do not laterally migrate. The fixed point of eq. (4.74) is obtained by setting $\dot{A}_1 = 0$, that gives, besides the trivial solution, the finite saturated amplitude

$$|A_s|^2_{I,K} = -\left(\frac{\omega_1}{\Xi}\right)_{I,K} = \frac{N_{I,K}}{D_{I,K}} \tag{4.75}$$

with

$$\begin{gathered} N_K = 4(\gamma\Gamma - 4) \\ N_I = 2b^2\Sigma_I(\Gamma\gamma b + 1) \\ D_K = 27\gamma^2\Gamma^2\Sigma_K\,(1+\Sigma_K)\,[-2+\Gamma\gamma(1+\Sigma_K)] \\ D_I = 9\left[\Gamma^3\gamma^3b^3(\Sigma_I+1) - \Gamma^2\gamma^2b^2(b+1)(\Sigma_I+3) - \Gamma\gamma b(b+1)(\Sigma_I-3) + \Sigma_I - 1\right] \end{gathered}$$

where $\Sigma_I = \sqrt{1 - 4\Gamma\gamma b(b+1)/(\Gamma\gamma b+1)^2}$ and $\Sigma_K = \sqrt{1 - 4/\Gamma\gamma}$. In order to dimensionally reconstruct the variables $\hat{h}$ and $\hat{\eta}$, one should use eq. (4.64) and the uniform flow depth $\hat{h}_0$. As we discuss in Sec. 4.4.4, wherein numerical simulations of the original eqs. (4.26) and (4.47) are showed, the solutions (4.75) lead to accurate predictions for the flow depth $\hat{h}$, but not for the bottom height $\hat{\eta}$. However, the direct use of the wall evolution eq. (4.47) allows us to bypass this drawback. Similar considerations regard the so-called saturation time $\hat{t}_s$, defined here so that $A_1(0)$=$0.001A_s$ and $A_1(t_s)$=$0.99A_s$.

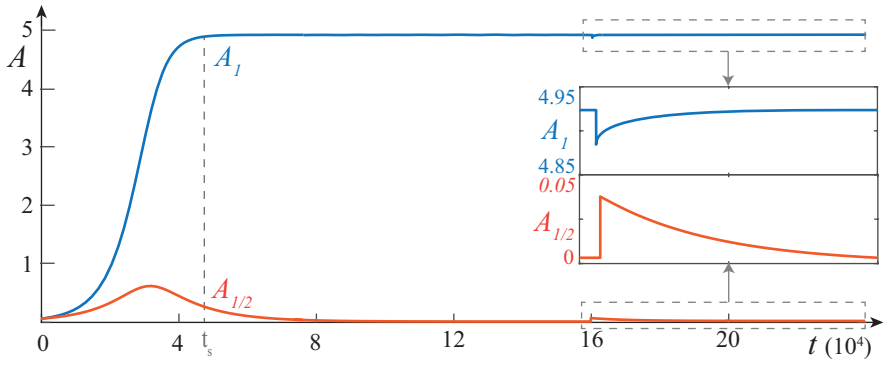

Fig. 4.6 Subharmonic stability. Numerical simulation of the nonlinear amplitude equations (4.72)-(4.73) for A_1 (blue line) and $A_{\frac{1}{2}}$ (red line). The subharmonic mode 1/2 is initially linearly unstable, then it is stabilised by the nonlinear interactions with the fundamental that saturates. The insets show how perturbations of the basic state $(A_1, A_{\frac{1}{2}}) = (A_s, 0)$ decrease in time, thus proving the stability of the fundamental. (Ice case, $Re = 0.05$ and $\vartheta = \pi/2 + \pi/36$. Same qualitatively results hold for the karst case

4.4.3 Subharmonic stability analysis

In order to study the stability of the saturated fundamental to disturbances with 1/2 its wavenumber, we perturb the fundamental and its 1/2 subharmonic around the state $(A_s, 0)$, respectively, as follows

$$(A_1, A_{\frac{1}{2}}) = (A_s, 0) + (a_1, a_{\frac{1}{2}}) \tag{4.76}$$

Substituting (4.76) into the master equations (4.72)-(4.73) and linearising, yields

$$\dot{a}_1 = 2\Xi A_s^2 a_1 \tag{4.77}$$

$$\dot{a}_{\frac{1}{2}} = (\omega_{\frac{1}{2}} + \tilde{G}_5 A_s^2 + P_3 A_s)\, a_{\frac{1}{2}} = \tilde{\omega}_{\frac{1}{2}} a_{\frac{1}{2}}. \tag{4.78}$$

It can be noticed that, since the fundamental is unstable, i.e., $\omega_1 > 0$, eq. (4.75) stipulates that Ξ must be negative for a saturated wave to exist. From eq. (4.77), it is therefore obtained that the saturated monochromatic wave is always stable to disturbances of the same wavenumber. The instability may instead arise from (4.78), depending on the sign of the growth rate of the subharmonic corrected by non-linearities, i.e., $\tilde{\omega}_{\frac{1}{2}}$. In both environments $\tilde{\omega}_{\frac{1}{2}}$ is negative in the domain of instability, that means that the fundamental is always stable to subharmonic disturbances. We have also tested numerically the previous conclusion by solving

directly the equations (4.72) and (4.73). The results of a representative simulation are reported in Fig. 4.6. Starting from a flat bottom, the fundamental A_1 (light blue line) and its subharmonic $A_{\frac{1}{2}}$ (red line) initially grow in agreement to the linear instability. Then, the influence of non-linearities become relevant, so that the fundamental saturates while its subharmonic decays to zero. This result is sufficient to prove the stability of the fundamental to 1/2 subharmonic when both modes are perturbed around the null state. Nevertheless, as the stability analysis (4.76) has been performed around the basic state $(A_1, A_{\frac{1}{2}}) = (A_s, 0)$, we have also introduced a small perturbation when the fundamental is already saturated while the subharmonic is vanishing, see insets. It can be observed that both perturbations decrease in time, showing once more the stability of the saturated fundamental to its 1/2 subharmonic.

4.4.4 Numerical simulations of the fully nonlinear system

The complete set of equations (4.26)-(4.47) has also been solved numerically for both environments. In Fig. 4.7a the wavy behaviour of saturated $\hat{h}$ in space is reported for the ice case. The y-axis has been reversed to remind the reader of the slightly overhanging conditions. The wavelength $\hat{L}$ corresponds exactly to the one expected by the linear theory, see eq. (4.57). The amplitude is well predicted by the center manifold projection, see eq. (4.75), especially for the lower limit of $\hat{h}$ (upper red line). Indeed, the amplitude of the fundamental can not catch the asymmetry of the solution, for which other harmonics and fully nonlinear effects should be included. Additionally, Fig. 4.7b shows the amplitude dynamics in time for a given spatial coordinate. Also in this case, the Stuart-Landau eq. (4.74) offers a good approximation in evaluating the saturation time $\hat{t}_s$.
Regarding the bottom height $\hat{\eta}$, the prediction of the linear analysis are robust, i.e., the wavelength $\hat{L}$ is consistent with the one of the water depth. However, the center manifold projection is not able to correctly capture the morphologic dynamics. This is likely due to the fact that the dynamics of η is mainly represented on the *stable* manifold of the $A_{[m,p]}$-phase space. This opens to two further separated remarks for the two different environments.

In the karst case, one can observe that the term $h-1$ in eq. (4.47b) is generally non-null, being the water depth wavy as in Fig. 4.7a. As there are no terms related to η (linearly or nonlinearly) to counteract the linear growing, flutings grow endlessly. This could explain the very large amplitude of flutings in flowstone worldwide, see

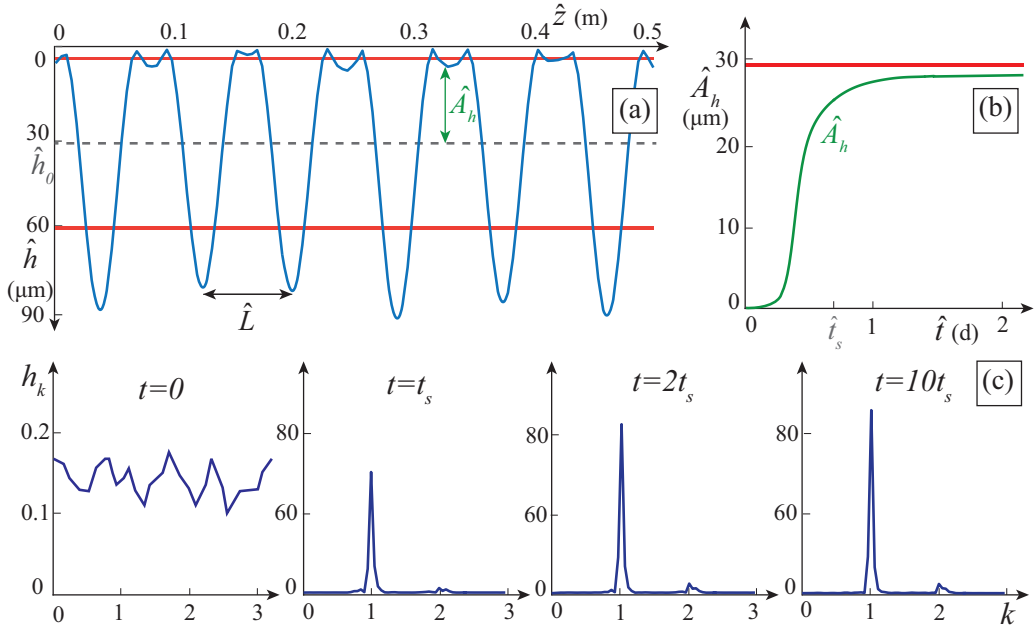

Fig. 4.7 Results of a numerical simulation (ice case, $Re = 0.05$, $\vartheta = \pi/2 + \pi/36$). (a) Wavy spatial behaviour of the saturated $\hat{h}$ (blue line). The initial condition is the uniform water depth $\hat{h}_0$ (grey dotted line). The red lines indicate the finite amplitude height expected by the nonlinear analytical theory. Both wavelength and amplitude ($\hat{L}$ and $\hat{A}_h$) are correctly predicted by the theory. (b) Evolution in time of water depth amplitude $\hat{A}_h$ for the case of panel *a* and $\hat{z} = 0.32$m. The Stuart-Landau eq. (4.74) fairly estimates the saturation time $\hat{t}_s$. (c) Evolution in time of the h spectrum starting from a white noise perturbation. The solutions converges to the fundamental and no nonlinear instabilities are detected.

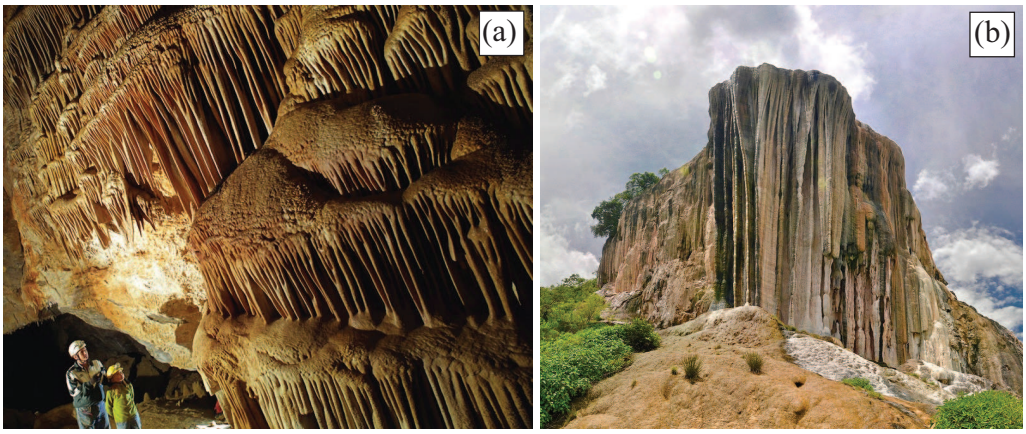

Fig. 4.8 Examples of very large amplitude karst flutings. (a) Yordas Cave, England. (b) Hierve el Agua, Mexico.

Fig. 4.8. Instead in the ice case, the linear term involving the perturbation of η in eq. (4.47a) does stop the pattern growth. Thus, by repeating the ansatz as in the linear analysis ($\eta = \bar{v}_I t + \eta_1$ and $h = 1 + h_1$), the r.h.s of eq. (4.47a) vanishes when the bottom height reaches a saturated value, η_{1s}, equal to

$$\eta_{1s} = b\, h_{1s}. \tag{4.79}$$

As h_{1s} is correctly given by the center manifold approximation through eq. (4.75), eq. (4.79) provides a very satisfactory result of the height of the pattern. Using the dimensional set of parameter of Fig. 4.7 and reminding that $b = \hat{b}/\hat{h}_0$, one obtains $\hat{\eta}_1 \sim 0.47$m.

Finally, to test the stability of the fundamental to nonlinear disturbances of other modes, we have performed long-term numerical simulation for the Benney-like eq. (4.26) with the bottom fixed. This latter choice is due to the fact that the dynamics of the whole system is driven by the water film. Fig. 4.7c shows the temporal evolution of the spectrum. Starting from a random white noise with all harmonics excited, the solution converges to the saturation of the fastest growing mode, i.e., the fundamental. This mode is not consequently destabilised nor by the 1/2 subharmonic, in agreement with the prediction of Sec. 4.4.3, nor by any other slow modes (higher order subharmonics at small wavenumbers that act at long times).

4.5 Discussion and Conclusion

In the present Chapter, fluting formation has been linearly and nonlinearly analysed through a unified approach which accounts for both the ice and the karst case. This task was addressed by combining two mathematical techniques: gradient expansion and center-unstable manifold projection.

Through the technique of gradient expansion, the Benney-type equation (4.26), accounting for the evolution of the evolving solid substrate, has been achieved. The coupling of the latter with the evolution equation for the substrate (4.47), provides a novel and parsimonious modelling of fluting dynamics. The outcomes of the linear analysis confirm the results previously obtained by a more sophisticated model (Camporeale, 2015), but also provide further achievements. Firstly, we have relaxed the Stokes approximation and solved the film flow field without the necessity to solve y-dependent differential equations. Secondly, the gain in the analytical treatment of the linear stability analysis has favoured the development of a nonlinear investigation.

Previous weakly nonlinear approaches have limited their validity close to the critical conditions (Stewartson and Stuart, 1971). The extension of the weakly nonlinear validity to the interior of the unstable domain has usually been conjectured since it was shown to be reasonable for some hydrodynamic instabilities (Godrèche et al., 2005). Whether this conjecture is also valid for morphodynamic instabilities remains open. Instead, the technique of center manifold projection furnishes the Stuart-Landau equation valid for any condition *close* to the neutral curve and not only in a neighbourhood of the critical point (Cheng and Chang, 1992).

The selected wavenumber (4.57) and the finite amplitude (4.75), given in a closed analytical form, provide the complete description of fluting system with respect to two control parameters: the Reynolds number and the angle with the horizontal. These quantitative results also have a value from a palaeo-reconstructive point of view. In fact, speleothems, such as cave flutings, contain information on the past climate since they evolve with a timescale of millennia (Fairchild et al., 2006; McDermott, 2004).

Nevertheless, defining quantitatively finite amplitude monochromatic waves may be not sufficient as they can be destabilized by nonlinear interactions with other modes. In particular, in other open flow systems with long-wave instabilities, the growth of subharmonic modes was detected. Therefore we have studied the linear

stability of the finite-amplitude fundamental mode to 1/2 subharmonic disturbances, verifying, both analytically and numerically, that flutings are stable to subharmonic disturbances as non-linearities allow the fundamental mode to saturate and the subharmonic to decay. From a practical point view, this means that the predictions of the linear and nonlinear analysis are robust.

Eventually, the numerical simulations of the equations (4.26)-(4.47) have confirmed most of the theoretical results. The linear theory is fully verified, while the nonlinear theory agrees correctly with the simulations for the hydrodynamics, but not for the morphodynamics. This is probably due to the fact that the center manifold projection looses some aspects of the dynamics of the stable manifold. Nevertheless, thanks to the correct prediction of the hydrodynamic behaviour, one may reconstruct the morphodynamics directly from the steady solution of eq. (4.47). This leads to the finite amplitude eq. (4.79) for ice flutings and to non-saturating patterns for the karst case.

Another issue that deserves further attention are the outcomes of the analysis close to verticality. In fact, when $\vartheta \to \pi/2^{+}$, the dimensional wavelength and the finite amplitude diverge to infinite (see Fig. 4.5d), that means that there is no wavelength selection nor amplitude saturation at this critical condition. This shortcoming could be remedied by a non-parallel stability theory, englobing the radius of curvature of the liquid-solid interface and non-parallelism of the flow field in a neighbourhood of the vertical tangent point (Camporeale, 2015).

Chapter 5

A stable model for icicle surface

5.1 Introduction

The work described in this chapter has been produced in collaboration with John Ladan and Stephen Morris (University of Toronto).

Icicles are common features of winter weather. Indeed, whoever is familiar with snow, has seen an uncountable numbers of icicles hanging from anthropic and natural ceilings. However, beside being beautiful, icicles are unwanted features on power lines and airplane wings (Farzaneh et al., 1992; Gent et al., 2000; Poots, 1996) and they can be reservoirs and vectors of pathogenic factors as fungi (Biedunkiewicz and Ejdys, 2011; Ejdys et al., 2014). Thus, a deeper understanding of icicle morphology, beside being a charming challenge for scientists (Chen and Morris, 2011; Ogawa and Furukawa, 2002; Ueno, 2007), could provide useful insights for practical applications.

Icicles form when cool water drips from an overhanging support under subfreezing ambient conditions. Therefore, their formation results from an interplay among the freezing ice, the cold air and the dripping water. Including all these aspects and some geometrical considerations, Short et al. (2006) derived a solution for the universal shape of icicles that fits most of the observations. Still, some icicles deviate from the self-similar shape, for example with bends, twists or spikes (Chen, 2014). In particular, one of icicle puzzling features are the regular ripples or ribs that may form around their circumference, see Fig. 1.4a. A recent extensive experimental study of icicles (Chen and Morris, 2013, 2011) revealed that small amounts of dis-

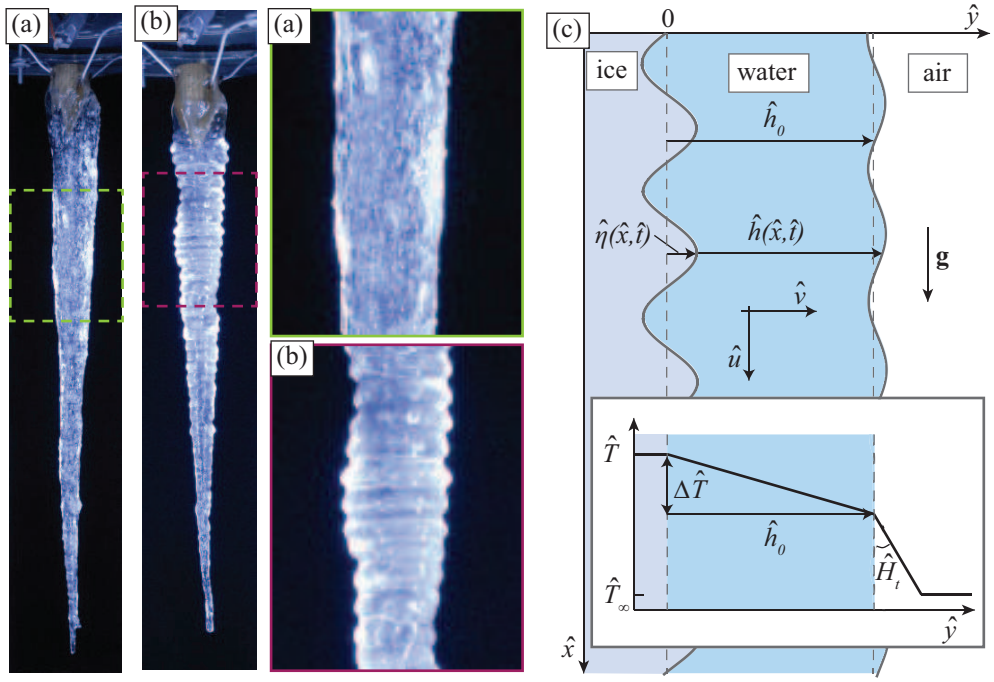

Fig. 5.1 Laboratory-grown icicles, showing the effect of impurities, and model sketch. (a) Icicle formed with distilled water, showing no ripples (Chen, 2018a). (b) Ripply icicle created with a NaCl solution with concentration 0.08 ppm (Chen, 2018b). (c) The coordinates and variables used in the model. The inset shows the dimensional temperature field in the unperturbed basic state.

solved impurities are required for ripples to appear. Fig 5.1a-b shows examples of laboratory-grown icicles. Existing linear stability theories of icicle ripples (Ogawa and Furukawa, 2002; Ueno, 2007; Ueno and Farzaneh, 2011; Ueno et al., 2009b) predict ripples on icicles made from pure water, which are not observed. In this Chapter, we outline a generic theory that shows that icicles made of distilled water do not develop ripples on their surfaces. Moreover, we present some theoretical considerations on how dissolved impurities, through freezing point depression at the growing ice surface, might drive the morphological instability.

The Chapter is organized as follows: in section 5.2, the mathematical problem leading to the governing equations is formulated; in section 5.3, the linear analysis is performed for icicles made of pure water; some theoretical considerations on the effect of impurities in the instability are presented in section 5.3.2; in section 5.4, a discussion of the results obtained so far and of the still open problems in icicle formations is presented.

5.2 Mathematical model

Icicles form when water drips from an overhanging support into a region of sub-freezing ambient air. The growing ice forms a substrate over which flows a very thin supercooled water film, usually less that 100μm thick. Only some of the water is consumed to form ice, while the rest drips off the growing tip of the icicle. Here, we ignore the large-scale shape of the icicle (Chen and Morris, 2011; Short et al., 2006), and, since the film thickness is much smaller than the icicle radius, treat the ice as a vertical plane. The water film is also much thinner than the ripple wavelength, which is about 1$\sim$cm, justifying a long wavelength approach. We solve for the gravity-driven, incompressible, two-dimensional Navier-Stokes flow with velocity $\hat{u} = (\hat{u}, \hat{v})$ in a plane perpendicular to the ice surface with $\hat{u}$ being the streamwise velocity and $\hat{v}$ the cross-stream velocity. The hat refers to dimensional variables. The coordinates and variables are shown in Fig. 5.1c. The growing ice-water interface is located at $\hat{y} = \hat{\eta}(x,t)$, while the free water-air interface is at $\hat{y} = \hat{\eta}(x,t) + \hat{h}(x,t)$. The $\hat{y}$ coordinate and $\hat{\eta}$ are measured relative to the position of the unperturbed, flat ice surface, which moves toward $+\hat{y}$ at speed $\bar{V}$, the average speed of ice growth. The importance of $\bar{V}$ in the icicle problem is the first main difference with the fluting problem in Chapter 4. The other differences regard the temperature $\hat{T}$ and the impurity concentration $\hat{c}$. Both these variables are governed, within the flowing film, by advection-diffusion equations such as

$$\hat{T}_{\hat{t}} + \hat{\mathbf{u}} \cdot \hat{\nabla} \hat{T} = \kappa_{\mathrm{w}} \hat{\nabla}^2 \hat{T}, \tag{5.1}$$

$$\hat{c}_{\hat{t}} + \hat{\mathbf{u}} \cdot \hat{\nabla} \hat{c} = D_{\mathrm{c}} \hat{\nabla}^2 \hat{c}\,, \tag{5.2}$$

where subscripts refer to partial derivatives and κ_{w} and D_c are the diffusivities of temperature and impurity concentration in water, respectively. Buoyancy effects due to differences of temperature and concentration are insignificant compared to the gravity-driven flow down the icicle, and so are neglected.

5.2.1 Boundary conditions

The boundary conditions for the hydrodynamics are basically the same as in the previous model for fluting formation, i.e., eqs. (4.11)-(4.14). The differences in the two model regard: the concentration of impurity $\hat{c}$, the temperature $\hat{T}$ and the mean

growth of the icicle $\bar{V}$. Moreover, here the possibility for a temperature dependent surface tension is included by writing (Kalliadasis et al., 2011)

$$\sigma = \sigma_f + \Lambda(\hat{T} - \hat{T}_f), \tag{5.3}$$

where $\hat{T}_f = 273.15$ K is the equilibrium melting temperature of pure water, σ_f is the surface tension at the melting point and $\Lambda = (-d\sigma/d\hat{T})|_{\hat{T}_f}$. To evaluate σ_f and Λ we have used the formula for seawater from Nayar et al. (2014), which fits the data for supercooled water well (Vins et al., 2015). In principle, σ might also be dependent on the concentration of the impurity $\hat{c} - \hat{c}_0$, but we estimate, following (Nayar et al., 2014), that $(d\sigma/d\hat{c})|_{\hat{c}_0}$ is too small to create a significant effect for our small concentrations. Similarly, the temperature and concentration dependence of the density ρ, kinematic viscosity ν, latent heat λ_f and of the thermal and molecular diffusivities κ_w, D_c, of the water are neglected.

Extra care is required to find the boundary conditions expressing the conservation of mass at the ice-water interface, because liquid water is actively solidifying onto the ice surface. The correct boundary conditions can be derived from the general expression for a kinematic condition, which, following a standard result of continuum mechanics (Hutter, 2017), states that the flux jump of a species across an interface must be zero;

$$\| \rho_s(\hat{\mathbf{u}}_s - \hat{\mathbf{v}}_I) \cdot \mathbf{n} \| = 0. \tag{5.4}$$

The brackets define the difference across the interface, $\|\psi\| = \psi^+ - \psi^-$; ρ_s and $\hat{\mathbf{u}}_s$ are the density and velocity of the considered species and $\hat{\mathbf{v}}_I$ is the velocity of the interface.

Applying (5.4) to the mass of water at the ice-water interface, we find

$$\mathbf{n} \cdot \hat{\mathbf{u}} = (1 - r_\rho)(\bar{V} + \hat{\eta}_{\hat{t}}), \qquad (\hat{y} = \hat{\eta}) \tag{5.5}$$

where $r_\rho = \rho_I/\rho$ is the ratio of ice and water densities . The physical meaning is that volumetric expansion of water freezing into ice imparts a cross-stream velocity. The non-zero velocity $\bar{V}$ relative to the ice surface will prove to be the biggest challenge for studying the icicles. Recall that $\bar{V}$ is the mean velocity of the ice surface in its flat, unperturbed, but still growing, state.

The temperature at the ice-water interface is assumed to be at the equilibrium freezing temperature which depends on the impurity concentration $\hat{c}$ through

$$\hat{T} = \hat{T}_f - \varsigma\,\hat{c}, \qquad (\hat{y} = \hat{\eta}) \tag{5.6}$$

where ς is the absolute value of the slope of the liquidus line. Equation (5.6) accounts for the equilibrium freezing point depression due to the impurity concentration and we believe is of fundamental importance in driving the ripple instability. The surface boundary condition (5.6) is the *only* point in the theory where the temperature and concentration fields interact. A second boundary condition on the temperature at the ice-water interface is given by the Stéfan condition,

$$\rho_I \lambda_f (\bar{V} + \hat{\eta}_{\hat{t}}) = -K_{\mathrm{w}} (\mathbf{n} \cdot \hat{\nabla}) \hat{T}, \qquad (\hat{y} = \hat{\eta}) \tag{5.7}$$

where K_w is the thermal conductivity of water. In eq. (5.7), no heat flux flows into the ice, which remains at a constant temperature. This choice is suggested by the geometrical and physical constraints on a free-hanging icicle, which does not normally require any sink for heat in its interior. In the flat, unperturbed state, the total heat flux can be determined from the mean growth speed $\bar{V}$ through (5.7),

$$\hat{J}_0 = \rho_I \lambda_f \bar{V}. \tag{5.8}$$

This flux defines a natural temperature scale

$$\Delta\hat{T} = \frac{\hat{J}_0 \hat{h}_0}{K_{\mathrm{w}}}, \tag{5.9}$$

which is the difference in temperature across the liquid film in its unperturbed state, as shown in Fig. 5.1c. The scale (5.9) is used to nondimensionalize the temperature.

Regarding the dissolved impurity, the assumption is that the growing ice completely excludes the dissolved impurity, leaving none trapped in the ice. This assumption yields a no flux boundary condition on the concentration $\hat{c}$ at the ice-water interface, analogous to the Stéfan condition,

$$\hat{c}(\bar{V} + \hat{\eta}_{\hat{t}}) = D_c (\mathbf{n} \cdot \hat{\nabla}) \hat{c}, \qquad (\hat{y} = \hat{\eta}). \tag{5.10}$$

It will be showed in the following section how dealing with eq. (5.10) is a complicated task. The model proposed is "one sided", in the sense that no heat or impurity flows into the ice, which remains pure and at a constant temperature. Regarding concentration, the choice of a one-sided model avoids additional physics for impure ice. This choice could be lifted, at the cost of additional complexity.

The constraint on the concentration at the water-air interface is simply a no flux condition, so that no impurities enter the air:

$$(\mathbf{n}\cdot\hat{\nabla})\hat{c}=0, \qquad (\hat{y}=\hat{\eta}+\hat{h}) \tag{5.11}$$

In this one-sided model, all of the latent heat released at the growing ice surface propagates outward through the water film and into the colder surrounding air. The temperature boundary condition at the water-air interface is given by

$$-K_{\mathrm{w}}\,(\mathbf{n}\cdot\nabla)\hat{T}=\hat{J}=\hat{H}_t\,(\hat{T}-\hat{T}_\infty), \qquad (\hat{y}=\hat{\eta}+\hat{h}) \tag{5.12}$$

where $\hat{J}$ is the total heat flux, $\hat{H}_t$ is a heat transfer coefficient and $\hat{T}_\infty$ is the temperature of the cold air far from the icicle. Unfortunately, $\hat{H}_t$ is not easy to measure directly, but it can be inferred experimentally by measuring the average speed of ice growth $\bar{V}$, as shown in the following

5.2.2 Water film dynamics through long-wave theory

Ripples on icicles usually develop with low Reynolds numbers ($Re<1$) and a small ratio between the film thickness and the pattern wavelength (order $10^{-2}-10^{-3}$), so that, as flutings in Chapter 4, they can be regarded as long-wave instabilities. For the icicle problem, the gradient expansion technique is extended to include, besides the evolving water-ice interface, the concentration of impurities, which was experimentally verified as the mechanism driving the rippling instability (Chen and Morris, 2013, 2011). As the film thickness is small with respect to the icicle radius, i.e., $\hat{h}_0 \ll \hat{R}_s$, a two-dimensional model with transversal invariance is considered, i.e., neglecting the curvature effect of the icicles. This assumption is also justified by the ice ripples experimentally observed on planar surfaces (Ueno et al., 2009b), which share same geometrical characteristics with the ones on cone-shaped icicles. The scaling for the hydrodynamic variables is the same as in (4.2). The concentration is

scaled by the inlet concentration, $\hat{c}_0$, while temperature is scaled according to (5.9)

$$\hat{c} = \hat{c}_0\, c, \qquad \hat{T} = \hat{T}_f + T\Delta\hat{T}. \tag{5.13}$$

After applying this scaling, the non-dimensional governing equations read

$$\varepsilon Re(u_t + u\,u_x + v\,u_y + P_x) = u_{yy} + 2, \tag{5.14}$$
$$Re\,P_y = \varepsilon\, v_{yy}, \tag{5.15}$$
$$u_x + v_y = 0, \tag{5.16}$$
$$\varepsilon Pe_T\,(T_t + u\,T_x + v\,T_y) = T_{yy}, \tag{5.17}$$
$$\varepsilon Pe_c\,(c_t + u\,c_x + v\,c_y) = c_{yy}, \tag{5.18}$$

where the film parameter $\varepsilon = \hat{h}_0/\hat{L}$ has been introduced ($\varepsilon \sim O(10^{-2})$). After applying the scaling and truncating at order ε, the boundary conditions at the ice surface, $y = \eta(x,t)$, read

$$u = 0, \tag{5.19}$$
$$v + \eta_x u = (1 - r_\rho)(\bar{v} + \eta_t), \tag{5.20}$$
$$T = -\mathscr{F} c, \tag{5.21}$$
$$r_\rho\, r_c \varepsilon\, Pe_h\, St\,(\bar{v} + \eta_t) = -T_y, \tag{5.22}$$
$$r_\rho\, Pe_c(\bar{v})c = -c_y. \tag{5.23}$$

These are the no-slip (5.19), conservation of water mass (5.20), undercooling (5.21), Stéfan (5.22) and impurity rejection (5.23) conditions. The dimensionless number $\mathscr{F} = \varsigma\hat{c}_0/\Delta T$ is introduced in (5.21) to capture the effect of impurities on the freezing point. A summary of the dimensionless numbers are listed in table 5.1. Notice also that We is considered of order ε^{-2} (Kalliadasis et al., 2011), St of order ε^{-2}, $\bar{v}$ of order ε (Chen and Morris, 2013) and, as we will show that the growth rate of the instability is a very small quantity, η_t is considered of order ε^2. This scaling separates the slow-moving dynamics from the boundary conditions except in the Stéfan condition (5.22).

Reynolds	Weber	Biot	Marangoni
$Re=\hat{h}_0\,\hat{u}_0/\nu$	$We=\sigma_f/(\rho\,\hat{h}_0\,\hat{u}_0^2)$	$Bi=\hat{H}_t\,\hat{h}_0/K_\mathrm{w}$	$M=\Lambda\Delta\hat{T}/(\rho\,\hat{h}_0\,\hat{u}_0^2)$
10^{-2}-1	10^3-10^6	$10^{-3}-10^{-2}$	$10^{-1}-10^2$
Peclet$_T$	**Peclet$_c$**	**Stéfan**	**Freezing point effect**
$Pe_T=\hat{h}_0\,\hat{u}_0/\kappa_{\mathrm{w,i}}$	$Pe_c=\hat{h}_0\,\hat{u}_0/D_c$	$St=\lambda_f/(c_\mathrm{i}\,\Delta\hat{T})$	$\mathscr{F}=\varsigma\,\hat{c}_0/\Delta\hat{T}$
$1-10$	$10-10^3$	10^4	$0-1$

Table 5.1 Definitions of the dimensionless numbers and their typical values.

The conditions at the air-water interface $y=\eta(x,t)+h(x,t)$ scale to

$$h_t+\eta_t+\bar{v}=v-u(h+\eta)_x, \tag{5.24}$$

$$u_y=\varepsilon M\,Re\,(T_x+(h+\eta)_xT_y), \tag{5.25}$$

$$Re\,\left[P+\varepsilon^2We\,(h+\eta)_{xx}\right]=2\varepsilon\left[v_y-(h+\eta)_x\,u_y\right], \tag{5.26}$$

$$Bi\,T+T_y+Bi\,r_\Delta=0, \tag{5.27}$$

$$c_y=0. \tag{5.28}$$

where (5.25)-(5.26) are the normal and tangential dynamic conditions; (5.24) is the kinematic condition for water that will be used later on as a solvability equation; (5.27) is the dimensionless form of (5.12) with $r_\Delta=(\hat{T}_f-\hat{T}_\infty)/\Delta\hat{T}$ appearing from the scaling; (5.28) is the kinematic condition for the dissolved species and it specifies the no flux of impurities through the air-water interface. It should be pointed out that, using the temperature scaling in (4.2) with (5.12), one obtains $Bi\,r_\Delta=(1+\mathscr{F})\,Bi+1$, from which

$$Bi=\frac{1}{r_\Delta-1-\mathscr{F}}. \tag{5.29}$$

The Biot number can be evaluated from (5.29) if the temperature of the air, the flow rate, the inlet uniform concentration and the average growth rate of the icicles are known. Thus avoiding the necessity to evaluate the non-trivial heat transfer coefficient $\hat{H}_t$.

Following the classical procedure of gradient expansion (Kalliadasis et al., 2011), a perturbative expansion in ε is carried out

$$(u,v,P,T,c)=(u^{(0)},v^{(0)},P^{(0)},T^{(0)},c^{(0)})+\varepsilon(u^{(1)},v^{(1)},P^{(1)},T^{(1)},c^{(1)})+O(\varepsilon^2). \tag{5.30}$$

Substituting (5.30) in the hydrodynamic problem (5.14-5.28), and collecting coefficients of like powers of ε, the problems at the different orders is obtained. At the leading order, the system reduces to

$$u_{yy}^{(0)} = -2, \quad u_x^{(0)} + v_y^{(0)} = 0, \quad P_y^{(0)} = 0, \quad T_{yy}^{(0)} = 0, \quad c_{yy}^{(0)} = 0, \tag{5.31}$$

with boundary conditions

$$u^{(0)}|_\eta = 0, \qquad u_y^{(0)}|_{\eta+h} = 0, \tag{5.32}$$

$$v^{(0)}|_\eta = 0, \qquad P^{(0)}|_{\eta+h} = -\varepsilon^2 We\,(h+\eta)_{xx}, \tag{5.33}$$

$$T^{(0)}|_\eta = -\mathscr{F} c^{(0)}|_\eta, \quad (Bi\,T^{(0)} + T_y^{(0)} + Bi\,r_\Delta)|_{\eta+h} = 0, \tag{5.34}$$

$$c_y^{(0)}|_\eta = 0, \qquad c_y^{(0)}|_{\eta+h} = 0. \tag{5.35}$$

The solutions of system (5.31) with boundary conditions (5.32) are

$$u^{(0)} = (y-\eta)(2h-y+\eta), \tag{5.36}$$

$$v^{(0)} = (y-\eta)[(\eta-y)\,h_x + (2h+\eta-y)\eta_x], \tag{5.37}$$

$$P^{(0)} = -\varepsilon^2 We\,(h+\eta)_{xx}, \tag{5.38}$$

$$T^{(0)} = \frac{\mathscr{F}\,[Bi(y-h-\eta)-1] - Bi\,r_\Delta(y-\eta)}{Bi\,h+1}, \tag{5.39}$$

$$c^{(0)} = 1. \tag{5.40}$$

Substituting the zero order solutions (5.36) in the kinematic free surface condition (5.24), we obtain at the leading order

$$h_t + q_x^{(0)} = 0 \tag{5.41}$$

where $q_0 = 2h^3/3$ is the dimensionless flow rate per unit-span at order 0. At the order ε, the system reads

$$u_x^{(1)} + v_y^{(1)} = 0, \tag{5.42}$$

$$Re\,(u_t^{(0)} + P_x^{(0)} + u^{(0)}\,u_x^{(0)} + v^{(0)}\,u_y^{(0)}) = u_{yy}^{(1)}, \tag{5.43}$$

$$Re\,P_y^{(1)} = v_{yy}^{(0)} \tag{5.44}$$

$$Pe_T\,(T_t^{(0)} + u^{(0)}\,T_x^{(0)} + v^{(0)}\,T_y^{(0)}) = T_{yy}^{(1)}, \tag{5.45}$$

$$Pe_c\,(c_t^{(0)} + u^{(0)}\,c_x^{(0)}) = c_{yy}^{(1)}, \tag{5.46}$$

with boundary conditions

$$u^{(1)}|_\eta = 0, \qquad u_y^{(1)}|_{h+\eta} + Re\,M\left[T_x^{(0)} + (h+\eta)_x\,T_y^{(0)}\right]_{h+\eta} = 0, \tag{5.47}$$

$$v^{(1)}|_\eta = \bar{v}(1-r_\rho), \qquad Re\,P^{(1)}|_{h+\eta} = 2[v_y^{(0)} - (h+\eta)_x\,u_y^{(0)}]_{h+\eta}, \tag{5.48}$$

$$T^{(1)}|_\eta = -\mathscr{F}\,c^{(1)}, \qquad (Bi\,T^{(1)} + T_y^{(1)})|_{h+\eta} = 0, \tag{5.49}$$

$$c_y^{(1)}|_\eta = 0, \qquad c_y^{(1)}|_{\eta+h} = -r_\rho\,Pe_c\bar{v}\,c^{(0)}, \tag{5.50}$$

whose solutions of $u^{(1)}$ and $T^{(1)}$ are cumbersome and reported in the Appendix D.1 for the sake of space.

5.2.3 Issue with the concentration of dissolved impurities

The two boundary conditions for the concentration (5.50) do not allow to solve the order ε problem for the concentration (5.46), which reads

$$c_{yy}^{(1)} = 0, \qquad c_y^{(1)}|_\eta = 0, \qquad c_y^{(1)}|_{\eta+h} = -r_\rho\,Pe_c\bar{v}\,c^{(0)}. \tag{5.51}$$

In fact, the advection-diffusion equation states that $c^{(1)}$ has a linear distribution in y, but the two boundary conditions give two different horizontal gradients. The reason of this failure is due to the slow build-up of impurities in the x-direction. During its flow, the liquid aqueous solution loses mass of water, which freezes to form the icicle, and preserves the same content of impurities, which are extruded by the forming ice. This double effect results in a growth of the concentration in the x-direction. This growth can not be detected by the gradient expansion technique, for which all x-dependencies are enclosed in the evolution of the two interfaces h and η.

From a more mathematical point of view, the inconsistency can also be noted from the value of Pe_c, which is not small (order ε^{-1}). By considering $Pe_c \sim \varepsilon^{-1}$, all terms l.h.s. of eq. (5.18) should be included in the equation for $c^{(0)}$ (5.31). This would allow to solve not even the $c^{(0)}$ problem through the gradient expansion method, again, because of the x-dependencies.
Thus, to properly include the effect of impurities in the icicle problem, the built-up of c in the x direction needs to be solved. At the moment of writing this thesis, we are dealing with this problem. Thus, apart from Section 5.3.2, where some preliminary results are discussed, we here present the model results for the case of pure water.

5.2.4 Evolution equations in the case of pure water

The expansion performed in the previous section has recast the physical variables (u, v, P, T) as functions of the unknown water-ice and air-water levels, i.e., η and $\eta + h$, respectively. The evolution equations for h and η are found by substituting the solutions of the flow field and temperature to $O(\varepsilon)$ into (5.22) and (5.24). Starting with (5.24), which dynamically describes the evolution of the free-surface, the first equation of the model is obtained

$$h_t + q_x^{(0)} + r_\rho \, \bar{v} + \varepsilon \, q_x^{(1)} = 0, \tag{5.52}$$

where $r_\rho \, \bar{v}$ (order ε) accounts for the loss of water due to the growing freezing icicle and $q^{(1)}$ is the order ε flow rate per unit-span, which reads

$$q^{(1)} = \frac{8}{15} Re \, h^6 h_x + \frac{1}{3} ReWe \, h^3 (h+\eta)_{xxx} + MRe \, h_x \, h \Gamma_2(h). \tag{5.53}$$

In (5.53), the first term is due to the inertia of the water flow; the second term accounts for surface tension and the last term accounts for the thermal Marangoni effect, where $\Gamma_i(h) = Bi \, r_\Delta h^{i-1} / [i(1+Bi\,h)^i]$. Neglecting thermocapillarity (Joo et al., 1991a) and the loss of water due to $\bar{v}$, (5.52) reduces to the Benney-type equation (4.26) at verticality.

The ice-water interface is dynamically described by the Stéfan equation (5.22), that, after substitution of $T^{(0)}$ and $T^{(1)}$, reads

$$r_\rho \, r_c \, Pe_T \, St \, \varepsilon (\bar{v} + \eta_t) - \Gamma_1(h) + \varepsilon \frac{1}{10} Pe_T \, h \, h_x \, [Bi\,h(4Bi\,h+5) - 10] \Gamma_3(h) = 0. \tag{5.54}$$

Where St and η_t are order ε^{-2} and $r_c = c_\mathrm{i}/c_\mathrm{w}$ is the ratio between specific heat of water and ice, respectively. Compared to Stefan equation (4.34) in the fluting problem, this Stefan equation (5.54) is one-sided (no heat flux in the ice), but all nonlinear terms have been retained.

5.3 Linear stability analysis

In this section, the stability of the uniform solution is considered. As the asymptotic expansion has been completed, x and t are rescaled so that x has the same scale as y, that is $\hat{L} = \hat{h}_0$ and $\hat{x} = \hat{h}_0 x$, or equivalently $\varepsilon = 1$. Then, the free-surface and the ice-water interface are infinitesimally perturbed around the base uniform solution as

$$\mathbf{U} = \mathbf{U}_0 + \mathbf{U}_1 = (h, \eta) = (1, 0) + (H, \Theta)\, \mathrm{e}^{ikx+\omega t}, \tag{5.55}$$

where k is the longitudinal wavenumber; ω is a complex number, whose real and imaginary parts determine the growth rate and the angular phase, respectively. It should be noted that $h = 1$ is a solution of the Benney-type eq. (5.52), if the loss of water due to the growing freezing icicle is neglected.

By substituting (5.55) in the two governing equations (5.52)-(5.54) under the quasi-steady approximation ($h_t \sim 0$), and linearizing, the system reduces to

$$\mathbf{L} \begin{pmatrix} H \\ \Theta \end{pmatrix} = 0, \tag{5.56}$$

where

$$\mathbf{L} = \begin{pmatrix} 10ReWek^3 - (16Bi_1 + 15M)Rek/Bi_1 + 60\,\mathrm{i} & 10k^3 ReWe \\ Bi_1(30BiBi_1 + \mathrm{i}(Bi(4Bi_1 + 1) - 10)kPe_T) & 30Bi_1^3 Pe_T r_c r_\rho St\,\omega \end{pmatrix}, \tag{5.57}$$

and $Bi_1 = Bi + 1$. The dispersion relation can then be found by setting the determinant of $\mathbf{L}$ equal to zero, to determine

$$\omega = \frac{k^3 ReWe(30BiBi_1 + \mathrm{i}(Bi(4Bi_1 + 1) - 10)kPe_T)}{3Bi_1 Pe_T\, r_c\, r_\rho\, St\,(10Bi_1 k^3 ReWe - 16Bi_1\, kRe + 60\,\mathrm{i}\,Bi_1 - 15kMRe)}, \tag{5.58}$$

Input parameters	Derived parameters	Dimensionless parameters
$\hat{Q} = 3.3 \times 10^{-8}$ m^3/s	$\Delta\hat{T} \sim 0.05$ K	$Re = 0.3$
$\hat{T}_\infty = \hat{T}_f - 10$ K	$\sigma_f = 0.076$ N/m	$We = 1.5 \times 10^4$
$\hat{c}_0 = 0 - 2$ ppt	$\Lambda = 1.4 \times 10^{-4}$ N/(m K)	$\bar{\nu} = 1.8 \times 10^{-4}$
$\bar{V} = 1.69 \times 10^{-6}$ m/s [1]	$\hat{R}_s = 1.7 \times 10^{-2}$ m [2]	$Bi = 5.3 \times 10^{-3}$

Table 5.2 Typical values of the parameters from the experiments of Chen and Morris (2013). The other dimensionless parameters, see tab. 5.1, can be evaluated from the ones here reported.

which is the eigenvalue of the linear system. In order to find a simpler form for ω, a quasi-steady approximation for h has been used ($h_t \sim 0$). It is possible to relax the quasi-steady approximation and obtain a dispersion relation with two eigenvalues $\omega_{1,2}$, where ω_1 is associated to the free surface instability (hydrodynamic waves) and ω_2 is related to the ice ripple instability. However, we have verified that ω_1 is numerically equivalent to the eigenvalue one would obtain neglecting the ice-water interface, i.e., longitudinal free surface waves of a falling vertical film (Craster and Matar, 2009; Kalliadasis et al., 2011), and ω_2 is numerically equivalent to ω in the dispersion relation (5.58), but its analytical expression is much more cumbersome. For this reason, the quasi-steady approximation has been used.

5.3.1 Stability for the case of pure water

In this section, the ω eigenvalue (5.58) is explored in the parameter space. In accord with the experiments (Chen and Morris, 2013, 2011), the results will show that pure water does not drive the rippling instability. If not differently specified, the plots have been obtained using the experimental values of Chen and Morris (2013), which are reported in table 5.2.

Physically speaking, the dimensional quantities controlling icicle formation in the pure water case are: the temperature of the air $\hat{T}_\infty$, which relates to r_Δ and Bi through (5.29); surface tension of water (We) and the dripping flow rate $\hat{Q}$. Regarding the

[1] Measured quantity

[2] Icicle radius, which determines the scaling and the Reynolds number, see (4.1)

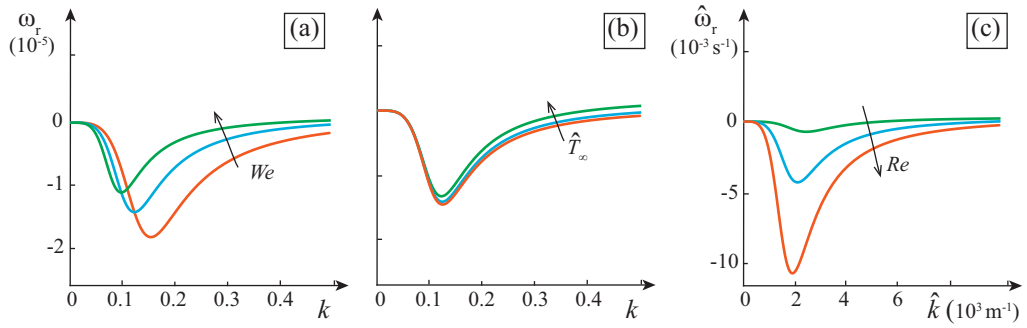

Fig. 5.2 Weak sensitivity of ω to the parameters. Blue lines refer to the reference case of tab. 5.2, while red and green lines are obtained: in panel (a), for doubling and halving surface tension σ_f; in panel (b), for $\hat{T}_\infty = \hat{T}_f - (5, 10, 20)$ K; and in panel (c) for $Re = 0.05, 0.3, 0.8$. Notice that in panel (c), the dimensional quantities have been plotted because the scaling (4.1) has an implicit dependence on Re.

latter, it can be noticed that

$$Re = \frac{\hat{Q}}{(2\pi \hat{R}_s \nu)} = \frac{\hat{q}}{\nu}, \tag{5.59}$$

so that the Nusselt scales $\hat{h}_0$ and $\hat{u}_0$ (4.1) can be evaluated from Re, instead of both $\hat{R}_s$ and $\hat{Q}$. Moreover, the derived dimensionless number can be recast in term of Re as follows

$$Pe_c = Re\, Pr_c, \qquad Pe_T = Re\, Pr_T, \qquad We = Ka\, Re^{-5/3}, \tag{5.60}$$

where Ka, $Pr_T = \nu/\kappa_w$, $Pr_c = \nu/D_c$, which are the Kapitza number and the thermal and mass Prandtl numbers, depend only on the fluid properties. Thus, varying Re it is possible to evaluate all flows condition (combinations of $\hat{R}_s$ and $\hat{Q}$). In Fig. 5.2, the growth rate ω_r is plotted for different parameter combinations. Overall, the plot show that none of the afore-mentioned quantity drastically changes the liner outcome: the water-ice interface is always stable for distilled water. Only surface tension (We) has a weak influence on ω_r (panel a). This is due to the stabilizing role surface tension has on the free surface. However, even though the reported dotted curves have been obtained halving and doubling the surface tension of pure water, thus exaggerating the interval of values that σ_f can actually assume, the effect on ω results weak. For this reason, the addition of a surfactant in some runs of the experiments by Chen and Morris (2013) has produced no noticeable differences. A rise in Re has an effect

on the temporal dynamics of the decaying perturbation. It should also be pointed out that panel (d) has been plotted with the dimensional quantities because of the implicit dependency of the scaling (4.1) on Re.

5.3.2 The freezing point depression effect

In this Section, we discuss how a longitudinal dependence of the concentration of dissolved impurities c can trigger the morphological instability through the depression of the freezing temperature (5.21). To do so, we have plotted in Fig. 5.3 the linear fields of concentration c, temperature T and horizontal heat flux T_y for the two cases: pure water (first raw) and aqueous solution (second raw). The fields are plotted on a x-wavelength in the water domain, i.e., between η and $\eta + h$, which have been perturbed as in (5.55). For the aqueous solution, we have introduced a non-physical approximation ($c \sim h^{-3}$) to show the importance of a x-dependent c in the thermodynamics. The proper approach would be to solve the slow built-up of concentration in the x-direction, as explained in Section 5.2.3.

Let us start from the case of pure water. The temperature field (b1) in the perturbed domain slightly differs from the temperature field in uniform condition, which is a horizontal linear distribution of temperature going from 0 to -1, see the temperature scaling (4.2) and the inset in Fig. 5.1c. A better physical intuition of the heat dynamics can be obtained by plotting $T_y + 1$ (c1), which is equivalent to the perturbation of the horizontal heat flux. Negative values of $T_y + 1$ (blue areas) show a rise in the heat flowing into the surrounding air. This heat comes from the additional latent heat released at the water-ice interface, which is thus freezing faster. The opposite stands for positive values (red areas). As on the perturbed η, water freezes faster (slower) in the trough (crest), the perturbation decays in time and the flat water-ice interface is eventually re-established.

The outcomes change drastically if the water contains dissolved impurities that distributes longitudinally. The perturbed temperature field (b2) becomes very different from the one in uniform condition, which is a horizontal linear distribution of temperature. In fact, panel (b2) shows a remarkable wavy structure caused by the concentration distribution (a2) and the consequent freezing point depression. The perturbed horizontal heat flux (c2) noticeably differs from the one for pure water (c1) for both the magnitude and the phase. The latter being the most important in

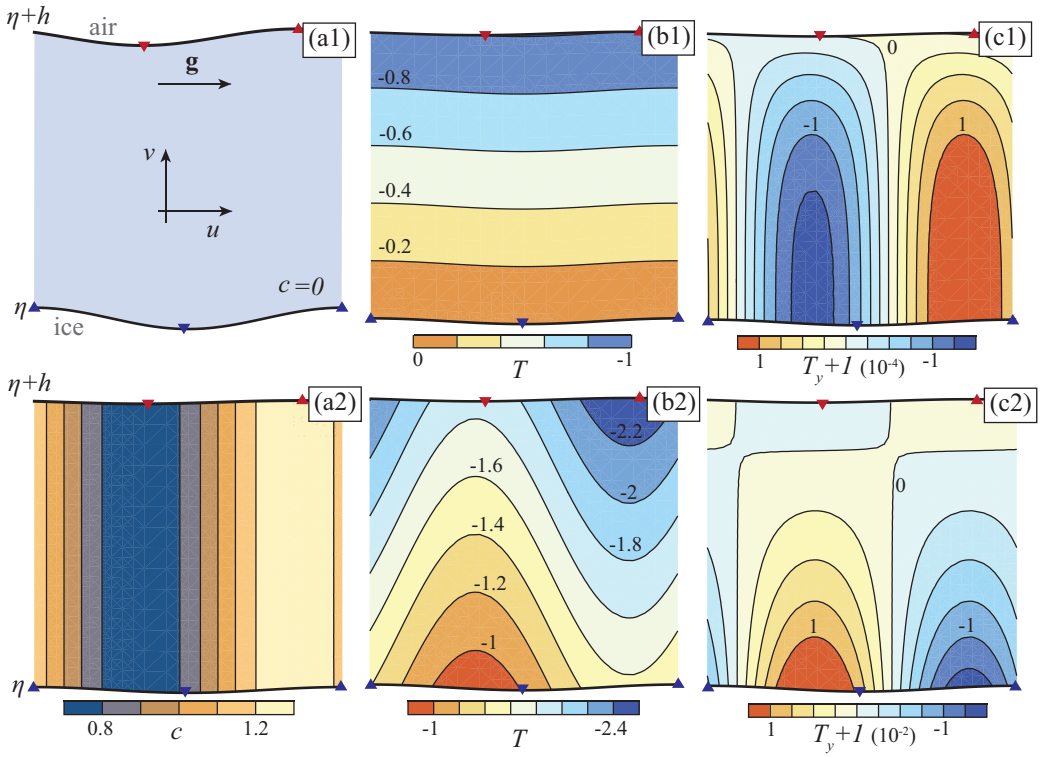

Fig. 5.3 Linear concentration and temperature fields. The first raw refers to the pure water case, while the second raw to an aqueous solution where the concentration has an unphysical longitudinal distribution ($c \sim h^{-3}$). The perturbation of η and h have been vertically exaggerated in panel (a1) to clarify the positions of crests and troughs (triangles) in all panels. Because of the freezing point depression, the concentration (a2) has a strong influence on the temperature field (b2) and to the horizontal heat flux (c2).

terms of the instability. In fact, as the peak of the additional latent heat is released slightly upstream the η crest, the water-ice interface perturbation grows in time, while migrating upstream. Moreover, it should be noticed that the heat fluxes (c2) are enhanced by the non-uniformity of the temperature at the ice-water interface and thus the deviations from the base state are two order of magnitude higher than in the pure water case (c1).

From these fictitious results, we are confident that properly solving the concentration field and its x-dependence could lead to a correct modelling of icicle morphological instability.

5.4 Concluding remarks

In this Chapter, a theoretical model for the morphological evolution of icicle surface has been presented. The model considers a thin water film flowing on a vertical plane of ice in a subfreezing ambient. The classical long-wave theory (Craster and Matar, 2009; Kalliadasis et al., 2011) has been applied to recast the variables as combinations of the ice-water, η, and water-air, $\eta + h$, interfaces. Consequently, the kinematic condition for the free surface (5.52) and the Stefan equation (5.54) have been used as the two solvability equations for the model.

The linear stability analysis of the uniform solution has revealed that icicles formed by pure water do not develop radial ripples on their surface. This result, which agrees with the experiments (Chen and Morris, 2013, 2011), represents a novelty, as existing linear stability theories predict ripples on icicles made from pure water (Ogawa and Furukawa, 2002; Ueno, 2007; Ueno and Farzaneh, 2011; Ueno et al., 2009b).

Recents experiments have also showed that small amounts of dissolved impurities are required for ripple formation on icicles (Chen and Morris, 2013, 2011). We could not properly address the problem, as the dynamics of the dissolved impurities could not be solved through the gradient expansion technique due to the complex boundary conditions, see Section 5.2.3. In particular, the issue is that as the aqueous solution flows down, part of the water is lost due to the freezing, but the content of impurity is preserved as the freezing ice extrudes the dissolved chemicals. This process causes a slow built-up of concentration in the x vertical direction, which can not be addressed

by the gradient expansion technique. The correct approach would be to first solve the problem of c in the x-direction, which we strongly believe to be responsible for the ripple instability, see Sec. 5.3.2, and then perform a stability analysis with a x-dependent base state. Such mathematical approach is the so-called global stability analysis (Huerre and Monkewitz, 1990; Schmid and Henningson, 2012) and, at the moment of writing this thesis, is in development.

Chapter 6

Conclusions

This thesis focuses on the analytical modelling of natural patterns that arise as morphological instabilities. These morphological patterns can be found in different natural environments (see Fig. 1.1-1.6), but because of their common fluid mechanical origin, they share very similar features. This similarity allows for a universal mathematical approach, i.e., the stability analysis. Such approach investigates the instability of the uniform flat solution to a small spatial perturbation, which grows in time to eventually generate the morphological pattern. The governing mathematical system of partial differential equations consists of the Navier-Stokes equations for the fluid flow and an evolution equation for the solid boundary, which depends on the environment considered. In nature, there is a plethora of morphological patterns that arise as instability. In this thesis, we have focused on some open issues regarding alternate bars in rivers (Chapters 2-3), flutings in ice-falls and caves (Chapter 4) and icicles (Chapter 5).

Main contributions

Bars are the most important fluvial patterns and they have been studied extensively in the last decades. However, the effect of suspended load on bar formation has been investigated using only a few analytical models and field studies. In Chapter 2, the linear analysis of the Shallow Water and Exner equations with suspended load performed by Federici and Seminara (2006) has been extended to the weakly nonlinear level through the Center Manifold Projection (CMP) technique. The main

result is the Stuart-Landau equation (2.34), which gives an analytical relations for the finite amplitude of alternate bars in presence of suspended load.

In Chapter 3, an analytical approach to link the three cornerstones of ecomorhodynamics (flow stochasticity, sediment transport and vegetation growth) is presented. The rationale of the approach is quite general, but here it is applied to investigate the conditions for vegetation spreading on alternate bars. Alternate bars are modelled through the relationships found in Chapter 2, flow stochasticity is addressed through the Compound Poisson Process (CPP) and vegetation grows as a secondary instability on the finite-amplitude bars. The main finding is that flow variability discourages vegetation proliferation, up to the point that above a certain threshold, c_v^* in eq. (3.6), plant spread is completely inhibited. Such transition from vegetated to bare state depends parametrically on flow stochasticity, morphology and plant biomechanical characteristics.

In Chapter 4, a unified mathematical approach is adopted in the study of karst and ice flutings. The model is obtained through the classical long-wave theory for falling liquid films and is a considerable simplification of previous theories (Camporeale, 2015). The linear stability analysis has verified that flutings develop on slightly overhanging walls and that the wavelength (4.57) depends only on the geometry. The weakly nonlinear analysis, through CMP, has provided the Stuart-Landau eq. (4.74) for fluting amplitude, and verified the stability of the finite-amplitude fundamental to subharmonic disturbances. These quantitative results for karst flutings have an additional value from a palaeo-reconstructive point of view, as karst flutings evolve with timescale of millennia.

In Chapter 5, a theoretical model for the morphological evolution of icicle surface is presented. The model considers a thin water film flowing on a vertical plane of ice in a subfreezing ambient. Thus, as in the fluting problem, the classical long-wave theory for falling liquid films has been applied. The linear stability analysis has revealed that icicles formed by pure water do not develop radial ripples on their surface. This result is in agreement with a recent and extensive set of experiments (Chen and Morris, 2013, 2011), that has shown that small quantities of dissolved impurities are necessary for radial ripples to appear. Some theoretical considerations on how dissolved impurities, through the depression of the freezing point, might trigger the ripple instability are also presented.

Validation of the theoretical models

The theoretical results of this thesis have all been, at least partially, validated through field observations, numerical simulations or experimental evidence.

In Chapter 2, the theoretical wavelength and amplitude for bars formed by suspended load have been verified with the few field observations of sandy alternate bars present in literature. The comparison with the field data has shown that the theoretical inclusion of suspension has increased the accuracy. Nonetheless, experiments would allow a more systematic validation to be made.

In Chapter 3, five rivers with vegetated alternate bars have been used for the validation of bar sizes and vegetation cover. As also reported in Fig. 3.4, the ecomorphodynamic theory quantitatively captures the underlying physics providing a good matching between theoretical predictions and field observations. A partial exception is the actual vegetation cover of the Arc river, which is not fully captured.

In Chapter 4, linear and nonlinear results on flutings have been validated through numerical simulations of the governing equations, see Fig. 4.7. For flutings and, more in general, karst patterns, very few field data are available in literature and experiments are impossible due to the secular timescales. At the moment of writing this thesis, we are working to a systematic collection of data in the Bossea Cave in Italy (Fig. 1.3), that we hope might serve future and past analytical models.

Regarding icicles, a very extensive dataset is freely available online (Chen et al., 2018) and the data therein have been deeply investigated (Chen and Morris, 2013, 2011), but a theoretical model that correctly explains ripple instability is still lacking. In fact, the previously published theories predict ripples on icicles made from pure water, which are not experimentally observed. The model proposed in Chapter 5 is a step forward in the direction of a correct modelling, as it predicts the no-ripple surface of icicle made of pure water. However, the model still lacks a correct solution for the dynamics of dissolved impurities.

Mathematical limitations

The Clay Math Institute offers a one million dollar prize for the first person to solve the Navier-Stokes equation (Institute, 2018), i.e., the equations governing fluid dynamics. However, these equations, found in XIX century, seem theoretically

unsolvable. Thus, to develop analytical models involving fluid dynamics, many simplifications have to be made. This is true also for morphological models, in which the fluid flow is the driving of the morphological instability.

The mathematical simplifications of the full Navier-Stokes equations arise from observations of the physical processes involved. In particular, the most crucial consideration is on the importance of the different scales, both temporal and spatial. In rivers, the water depth is usually much smaller than the channel width. This allows to vertically integrate the Navier-Stokes equations and derive the more amenable Shallow Water and Exner equations (2.1)-(2.4) used in Chapter 2 and 3. In falling liquid films, the wavelength of the free-surface wave, as well as the morphological pattern wavelength, is much longer than the film thickness. This allows to apply the long-wave theory to obtain the Benney-type equations (4.26)-(5.52) used in Chapter 4 and 5, which are a considerable simplifications of the initial Navier-Stokes system. Therefore, even before the stability analysis, the models are approximations of the physical reality, which would be described by the full Navier-Stokes equations.

The stability analysis of the ideally flat uniform solution introduces further approximations. Through the linear stability analysis, one usually obtains the pattern wavelength. The classical assumption is that all modes solutions of the system are initially infinitesimally small, so that the one that grows faster selects the pattern wavelength. However, in real situations, the presence of boundaries, local structures and defects might develop finite initial conditions for some modes, that could so prevail on the one that grows faster (Cross and Hohenberg, 1993).
Weakly nonlinear analyses are rigorous when the effect of the nonlinearities is *weak*, i.e., close to the conditions of neutrality (see for example the neutral stability curves in Figs. 2.2 and 4.5). From this point of view, the Center Manifold Projection offers the advantage of being valid in any condition close to the neutral stability curve, and not just around the critical point as multiple-scale theories (Wiggins, 2003). Still, the extension of the CMP results to the interior of the unstable domain remains a conjecture, whose validity can be proved only by full numerical simulations of the governing equations. Furthermore, the application of CMP needs just one eigenvalue to be unstable. So that, if more eigenvalues are unstable as in the case of multiple bars (Fig. 2.2), the results of CMP become unreliable.

Due to all the above-mentioned approximations and sources of complexity, in morphodynamics a perfect match between theoretical models and reality remains

elusive. A morphodynamic analytical model can be regarded as reliable when it furnishes predictions that agree with observations fairly good in the order of magnitude. In this sense, the models exposed in this thesis give satisfactory results. Moreover, analytical models are the necessary tools to deepen the comprehension of the underlying physical processes.

Ideas for future research

Human-kind has always exploited natural resources, but with a population of 7.6 billion and an increasing demand for wellness, the man-induced stresses on natural environments have become unsustainable (Falkenmark, 1997; Helne and Hirvilammi, 2015; Hoekstra and Wiedmann, 2014). Consequently, the concern for natural issues has increased in scientists, common people and governments, with some sad exceptions (e.g., Tollefson (2017)). Indeed, to try to contain the effect of human activities on natural environments, a deeper physical understanding of nature in its every aspect is crucial. In this context, *morphodynamics* is a broad discipline that can describe the behaviour of many natural environments, as shown in Figs. 1.1-1.6. Probably for these reasons, the scientific research on morphodynamic problems has increased significantly in the last decades (e.g., Blondeaux (2001); Dreybrodt (2012); Lancaster (2013); Seminara (2010)). Still, much research, both theoretical and experimental, needs to be performed. Here, we briefly suggest some ideas for future research that have arisen from writing this thesis.

1. The role of suspended load in bedform patterns has never been experimentally investigated. Indeed, dealing with suspended load in a laboratory is a very challenging task. However, it would give meaningful insights on the quantitative role suspension plays in shaping the riverbed.

2. The ecomorphological model proposed in Chapter 3 offers a general rationale that could be applied to study vegetational patterns in other morphodynamic environments, see Fig. 3.1.

3. Field data on cave patterns should be systematically collected to support and improve the theoretical models.

4. Research should be performed to find a quantitative relation among cave speleothem features (as wavelength and amplitude) and age. This would allow

non-destructive paleoclimate considerations directly in the cave (to the present day, speleothems need to be removed from their environment to be analysed).

5. Ripple instability on icicles still needs a theoretical model that properly addresses the concentration of dissolved impurities (see Sec. 5.2.3).

References

M. Abramowitz, I.A. Stegun, et al. Handbook of mathematical functions. *Appl. Math. Series*, 55:62, 1966.

L. Adami, W. Bertoldi, and G. Zolezzi. Multidecadal dynamics of alternate bars in the alpine rhine river. *Water Resour. Res.*, 52(11):8938–8955, 2016.

T. J. Algeo and S. E. Scheckler. Terrestrial-marine teleconnections in the devonian: links between the evolution of land plants, weathering processes, and marine anoxic events. *Philos. T. R. Soc. B*, 353(1365):113–130, 1998.

J.R.L. Allen. *Sedimentary structures, their character and physical basis*, volume 1. Elsevier, 1982.

B. Andreotti, P. Claudin, and O. Pouliquen. Aeolian sand ripples: Experimental study of fully developed states. *Phys. Rev. Lett.*, 96(2):028001, 2006.

D. Armbruster, J. Guckenheimer, and P. Holmes. Heteroclinic cycles and modulated travelling waves in systems with O(2) symmetry. *Physica D*, 29(3):257–282, 1988.

A. Ashton, A.B. Murray, and O. Arnoult. Formation of coastline features by large-scale instabilities induced by high-angle waves. *Nature*, 414(6861):296, 2001.

F. Ayoub, J.P. Avouac, C.E. Newman, M.I. Richardson, A. Lucas, S. Leprince, and N.T: Bridges. Threshold for sand mobility on mars calibrated from seasonal variations of sand flux. *Nat. Commun.*, 5:5096, 2014.

A. Baker, D. Genty, W. Dreybrodt, W.L. Barnes, N.J. Mockler, and J. Grapes. Testing theoretically predicted stalagmite growth rate with recent annually laminated samples: Implications for past stalagmite deposition. *Geochim. Cosmochim. Ac.*, 62(3):393–404, 1998.

N. L. Bankhead, R. E. Thomas, and A. Simon. A combined field, laboratory and numerical study of the forces applied to, and the potential for removal of, bar top vegetation in a braided river. *Earth Surf. Proc. Land.*, 42(3):439–459, 2017.

M.J. Baptist, V. Babovic, J. Rodríguez Uthurburu, M. Keijzer, R.E. Uittenbogaard, A. Mynett, and A. Verwey. On inducing equations for vegetation resistance. *J. Hydraul. Res.*, 45(4):435–450, 2007.

F. Bärenbold, B. Crouzy, and P. Perona. Stability analysis of ecomorphodynamic equations. *Water Resour. Res.*, 2016.

C.M. Bender and S.A. Orszag. *Advanced mathematical methods for scientists and engineers I: Asymptotic methods and perturbation theory*. Springer Science & Business Media, 2013.

S.J. Bennett and A. Simon. *Riparian vegetation and fluvial geomorphology*, volume 8. American Geophysical Union, 2004.

S.J. Bennett, W. Wu, C.V. Alonso, and S.S. Wang. Modeling fluvial response to in-stream woody vegetation: implications for stream corridor restoration. *Earth Surf. Proc. Land.*, 33(6):890–909, 2008.

D.J. Benney. Long waves on liquid films. *Stud. Appl. Math.*, 45(1-4):150–155, 1966.

M.B. Bertagni and C. Camporeale. Nonlinear and subharmonic stability analysis in film-driven morphological patterns. *Phys. Rev. E*, 96(5):053115, 2017.

M.B. Bertagni and C. Camporeale. Finite amplitude of alternate free bars with suspended load. *Water Resour. Res.*, 2018.

M.B. Bertagni, P. Perona, and C. Camporeale. Parametric transitions between bare and vegetated states in water-driven patterns. *P. Natl. Acad. Sci. USA*, 115(32): 8125–8130, 2018.

W. Bertoldi, A. Gurnell, N. Surian, K. Tockner, L. Zanoni, L. Ziliani, and G. Zolezzi. Understanding reference processes: linkages between river flows, sediment dynamics and vegetated landforms along the Tagliamento River, Italy. *River Res. Appl.*, 25(5):501–516, 2009.

W. Bertoldi, A. Siviglia, S. Tettamanti, M. Toffolon, D. Vetsch, and S. Francalanci. Modeling vegetation controls on fluvial morphological trajectories. *Geophys. Res. Lett.*, 41(20):7167–7175, 2014.

G. Besio, P. Blondeaux, and G. Vittori. On the formation of sand waves and sand banks. *J. Fluid Mech.*, 557:1–27, 2006.

J. Best. The fluid dynamics of river dunes: A review and some future research directions. *J. Geophys. Res.-Earth*, 110(F4), 2005.

A. Biedunkiewicz and E. Ejdys. Icicles as carriers of yeast-like fungi potentially pathogenic to human. *Aerobiologia*, 27(4):333–337, 2011.

P. Blondeaux. Mechanics of coastal forms. *Annu. Rev. Fluid Mech.*, 33(1):339–370, 2001.

P. Blondeaux and G. Seminara. A unified bar–bend theory of river meanders. *J. Fluid Mech.*, 157:449–470, 1985.

P. Blondeaux, E. Foti, and G. Vittori. Migrating sea ripples. *Eur. J. Mech. B-Fluids*, 19(2):285–301, 2000.

P. Blondeaux, H.E. De Swart, and G. Vittori. Long bed waves in tidal seas: an idealized model. *J. Fluid Mech.*, 636:485–495, 2009.

M. Bolla Pittaluga and G. Seminara. Depth-integrated modeling of suspended sediment transport. *Water Resour. Res.*, 39(5), 2003.

G. Botter, S. Basso, I. Rodriguez-Iturbe, and A. Rinaldo. Resilience of river flow regimes. *Proc. Natl. Acad. Sci. USA*, 110(32):12925–12930, 2013.

Neima Brauner and David Moalem Maron. Characteristics of inclined thin films, waviness and the associated mass transfer. *International Journal of Heat and Mass Transfer*, 25(1):99–110, 1982.

N.T. Bridges, F. Ayoub, J.P Avouac, S. Leprince, A. Lucas, and S. Mattson. Earth-like sand fluxes on mars. *Nature*, 485(7398):339, 2012.

R.A. Callander. Instability and river channels. *J. Fluid Mech.*, 36(3):465–480, 1969.

C. Camporeale. Hydrodynamically locked morphogenesis in karst and ice flutings. *J. Fluid Mech.*, 778:89–119, 2015.

C. Camporeale. An asymptotic approach to the crenulation instability. *J. Fluid Mech.*, 826:636–652, 2017. doi: 10.1017/jfm.2017.454.

C. Camporeale and L. Ridolfi. Riparian vegetation distribution induced by river flow variability: A stochastic approach. *Water Resour. Res.*, 42(10), 2006.

C. Camporeale and L. Ridolfi. Ice ripple formation at large Reynolds numbers. *J. Fluid. Mech.*, 694:225–251, 2012a.

C. Camporeale and L. Ridolfi. Hydrodynamic-driven stability analysis of morphological patterns on stalactites and implications for cave paleoflow reconstructions. *Phys. Rev. Lett.*, 108(23):238501, 2012b.

C. Camporeale, P. Perona, A. Porporato, and L. Ridolfi. On the long-term behavior of meandering rivers. *Water Resour. Res.*, 41(12), 2005.

C. Camporeale, E. Perucca, L. Ridolfi, and A.M. Gurnell. Modeling the interactions between river morphodynamics and riparian vegetation. *Rev. Geophys.*, 51(3): 379–414, 2013.

C. Camporeale, R. Vesipa, and L. Ridolfi. Convective-absolute nature of ripple instabilities on ice and icicles. *Phys. Rev. Fluids*, 2:053904, May 2017. doi: 10.1103/PhysRevFluids.2.053904. URL https://link.aps.org/doi/10.1103/PhysRevFluids.2.053904.

J. Carr and R. G. Muncaster. The application of centre manifolds to amplitude expansions. ii. infinite dimensional problems. *J. Diff. Eqn.*, 50(2):280–288, 1983.

H. Chang. Wave evolution on a falling film. *Ann. Rev. Fluid Mech.*, 26(1):103–136, 1994.

F. Charru. *Hydrodynamic instabilities*, volume 37. Cambridge University Press, 2011.

F. Charru, B. Andreotti, and P. Claudin. Sand ripples and dunes. *Annu. Rev. Fluid Mech.*, 45:469–493, 2013.

A. Chen and S.W. Morris. On the origin and evolution of icicle ripples. *New J. Phys.*, 15(10):103012, 2013.

A-S. Chen. Experiments on the growth and form of icicles, 2014. URL http://hdl.handle.net/1807/44105.

A. S. Chen. Icicle run 120803, 2018a. URL https://doi.org/10.5683/SP/WFP0U7.

A. S. Chen. Icicle run 120725, 2018b. URL https://doi.org/10.5683/SP/KDSCAD.

A. S. Chen and S. W. Morris. Experiments on the morphology of icicles. *Phys. Rev. E*, 83(2):026307, 2011.

A-S. Chen, J. Ladan, and S. W. Morris. The icicle atlas, 2018. URL https://dataverse.scholarsportal.info/dataverse/Icicle_Atlas.

M. Cheng and H. Chang. A generalized sideband stability theory via center manifold projection. *Phys. Fluids A F. (1989-1993)*, 2(8):1364–1379, 1990.

M. Cheng and H. Chang. Subharmonic instabilities of finite-amplitude monochromatic waves. *Phys. Fluids A F. (1989-1993)*, 4(3):505–523, 1992.

M. Cheng and H. Chang. Competition between subharmonic and sideband secondary instabilities on a falling film. *Phys. Fluids*, 7(1):34–54, 1995.

P. Claudin, O. Durán, and B. Andreotti. Dissolution instability and roughening transition. *J. Fluid Mech.*, 832, 2017.

M. Colombini. Revisiting the linear theory of sand dune formation. *J. Fluid Mech.*, 502:1–16, 2004.

M. Colombini and A. Stocchino. Three-dimensional river bed forms. *J. Fluid Mech.*, 695:63–80, 2012.

M. Colombini, G. Seminara, and M. Tubino. Finite-amplitude alternate bars. *J. Fluid Mech.*, 181:213–232, 1987.

R.V. Craster and O.K. Matar. Dynamics and stability of thin liquid films. *Rev. Mod. Phys.*, 81(3):1131, 2009.

A. Crosato, F.B. Desta, J. Cornelisse, F. Schuurman, and W.S.J. Uijttewaal. Experimental and numerical findings on the long-term evolution of migrating alternate bars in alluvial channels. *Water Resour. Res.*, 48(6), 2012.

M. Cross and P.C. Hohenberg. Pattern formation outside of equilibrium. *Rev. Mod. Phys.*, 65(3):851, 1993.

P. J. Crutzen. The "anthropocene". In *Earth system science in the anthropocene*, pages 13–18. Springer, 2006.

L.A. Dávalos-Orozco, S.H. Davis, and S.G. Bankoff. Nonlinear instability of a fluid layer flowing down a vertical wallunder imposed time-periodic perturbations. *Phys. Rev. E*, 55(1):374, 1997.

H.E. De Swart and J.T.F. Zimmerman. Morphodynamics of tidal inlet systems. *Annual review of fluid mechanics*, 41:203–229, 2009.

A. Defina. Numerical experiments on bar growth. *Water Resour. Res.*, 39(4), 2003.

M.G. Dosskey, P. Vidon, N.P. Gurwick, C.J. Allan, T.P. Duval, and R. Lowrance. The role of riparian vegetation in protecting and improving chemical water quality in streams1. *J. Am. Water Resour. As.*, 46(2):261–277, 2010.

W. Dreybrodt. *Processes in karst systems: physics, chemistry, and geology*, volume 4. Springer Science & Business Media, 2012.

J. Dronkers. *Dynamics of coastal systems*. 2005.

K. Edmaier, P. Burlando, and P. Perona. Mechanisms of vegetation uprooting by flow in alluvial non-cohesive sediment. *Hydrol. Earth Syst. Sci.*, 15(5):1615, 2011.

J.P.C. Eekhout, A.J.F. Hoitink, and E. Mosselman. Field experiment on alternate bar development in a straight sand-bed stream. *Water Resour. Res.*, 49(12):8357–8369, 2013.

H.A. Einstein et al. *The bed-load function for sediment transportation in open channel flows*, volume 1026. Citeseer, 1950.

E. Ejdys, A. Biedunkiewicz, M. Dynowska, and E. Sucharzewska. Snow in the city as a spore bank of potentially pathogenic fungi. *Sci. Total Environ.*, 470:646–650, 2014.

F. Engelund and E. Hansen. A monograph on sediment transport in alluvial streams. 1967.

I. J. Fairchild et al. Modification and preservation of environmental signals in speleothems. *Earth-Sci. Rev.*, 75(1):105–153, 2006.

M. Falkenmark. Meeting water requirements of an expanding world population. *Philos. T. Roy. Soc. B*, 352(1356):929–936, 1997.

M. Farzaneh, J.L. Laforte, et al. Effect of voltage polarity on icicles grown on line insulators. *Int. J. Offshore Polar*, 2(04), 1992.

B. Federici and C. Paola. Dynamics of channel bifurcations in noncohesive sediments. *Water Resour. Res.*, 39(6), 2003.

B. Federici and G. Seminara. Effect of suspended load on sandbar instability. *Water Resour. Res.*, 42(7), 2006.

R.I. Ferguson, D.J. Bloomer, and M. Church. Evolution of an advancing gravel front: observations from vedder canal, british columbia. *Earth Surf. Proc. Land.*, 36(9): 1172–1182, 2011.

S. Filhol and M. Sturm. Snow bedforms: A review, new data, and a formation model. *J. Geophys. Res. Earth*, 120(9):1645–1669, 2015.

D. Ford and P.D. Williams. *Karst hydrogeology and geomorphology*. John Wiley & Sons, 2013.

K. Fujimura. Centre manifold reduction and the stuart-landau equation for fluid motions. In *P. Roy. Soc. Lond. A Mat.*, volume 453, pages 181–203. The Royal Society, 1997.

R.W. Gent, N.P. Dart, and J.T. Cansdale. Aircraft icing. *Phylos. T. R. Soc. Lond.*, 358(1776):2873–2911, 2000.

M.R. Gibling and N.S. Davies. Palaeozoic landscapes shaped by plant evolution. *Nat. Geosci.*, 5(2):99–105, 2012.

D. Gilvear and N. Willby. Channel dynamics and geomorphic variability as controls on gravel bar vegetation; River Tummel, Scotland. *River Res. Appl.*, 22(4): 457–474, 2006.

B. Gjevik. Occurrence of finite-amplitude surface waves on falling liquid films. *Phys. Fluids*, 13(8):1918–1925, 1970.

C. Godrèche, P. Manneville, and B. Castaing. *Hydrodynamics and nonlinear instabilities*, volume 3. Cambridge University Press, 2005.

E.B. Goldstein and L. J. Moore. Stability and bistability in a one-dimensional model of coastal foredune height. *J. Geophys. Res. Earth Surf.*, 121(5):964–977, 2016.

A. S. Goudie. Mega-yardangs: A global analysis. *Geogr. Compass*, 1(1):65–81, 2007.

M. H. Gradowczyk. Wave propagation and boundary instability in erodible-bed channels. *J. Fluid Mech.*, 33(1):93–112, 1968.

K. Gran and C. Paola. Riparian vegetation controls on braided stream dynamics. *Water Resour. Res.*, 37(12):3275–3283, 2001.

J. Guckenheimer and P.J. Holmes. *Nonlinear oscillations, dynamical systems, and bifurcations of vector fields*, volume 42. Springer Science & Business Media, 2013.

G. Gyssels, J. Poesen, E. Bochet, and Y. Li. Impact of plant roots on the resistance of soils to erosion by water: a review. *Prog. Phys. Geog.*, 29(2):189–217, 2005.

P. Hall. Alternating bar instabilities in unsteady channel flows over erodible beds. *J. Fluid Mech.*, 499:49–73, 2004.

T. Helne and T. Hirvilammi. Wellbeing and sustainability: a relational approach. *Sustain. Dev.*, 23(3):167–175, 2015.

G. A. Heshmati and V. Squires. *Combating desertification in asia, africa and the Middle East*. Springer, 2013.

A.Y. Hoekstra and T.O. Wiedmann. Humanity's unsustainable environmental footprint. *Science*, 344(6188):1114–1117, 2014.

P. Huerre and P.A. Monkewitz. Local and global instabilities in spatially developing flows. *Annu. Rev. Fluid Mech.*, 22(1):473–537, 1990.

T. A. Hurst, A.J. Pope, and G.P. Quinn. Exposure mediates transitions between bare and vegetated states in temperate mangrove ecosystems. *Marine Ecol. Prog. Series*, 533:121–134, AUG 6 2015. ISSN 0171-8630. doi: {10.3354/meps11364}.

J. M. Huthnance. On one mechanism forming linear sand banks. *Estuar. Coast. Shelf S.*, 14(1):79–99, 1982.

K. Hutter. *Theoretical glaciology: material science of ice and the mechanics of glaciers and ice sheets*, volume 1. Springer, 2017.

J.M. Hyman, B. Nicolaenko, and S. Zaleski. Order and complexity in the kuramoto-sivashinsky model of weakly turbulent interfaces. *Physica D*, 23(1-3):265–292, 1986.

Clay Math Institute. Millenium Problem: the Navier-Stokes equations, 2018. URL http://www.claymath.org/millennium-problems/navier%E2%80%93stokes-equation.

Y. Ishikawa, T. Sakamoto, and K. Mizuhara. Effect of density of riparian vegetation on effective tractive force. *J. For. Res.*, 8(4):235–246, 2003.

M. Jaballah, C. Benoît, P. Lionel, and P. André. Alternate bar development in an alpine river following engineering works. *Adv. Water Resour.*, 81:103–113, 2015.

Z. Ji and C. Mendoza. Weakly nonlinear stability analysis for dune formation. *J. Hydraul. Eng.*, 123(11):979–985, 1997.

S.W. Joo, S.H. Davis, and S.G. Bankoff. Long-wave instabilities of heated falling films: two-dimensional theory of uniform layers. *J. Fluid Mech.*, 230:117–146, 1991a.

S.W. Joo, S.H. Davis, and S.G. Bankoff. On falling-film instabilities and wave breaking. *Phys. Fluids A-Fluid*, 3(1):231–232, 1991b.

S. Kalliadasis, C. Ruyer-Quil, B. Scheid, and M. G. Velarde. *Falling liquid films*, volume 176. Springer Science & Business Media, 2011.

R. Kelly. On the stability of an inviscid shear layer which is periodic in space and time. *J. Fluid Mech.*, 27(04):657–689, 1967.

J.L. Kemp, D.M. Harper, and G.A. Crosa. The habitat-scale ecohydraulics of rivers. *Ecol. Eng.*, 16(1):17–29, 2000.

S. Kinast, E. Meron, H. Yizhaq, and Y. Ashkenazy. Biogenic crust dynamics on sand dunes. *Phys. Rev. E*, 87(2):020701, 2013.

K. Kosugi, K. Nishimura, and N. Maeno. Snow ripples and their contribution to the mass transport in drifting snow. *Bound.-Lay. Meteorol.*, 59(1-2):59–66, 1992.

P. Kutiel, O. Cohen, M. Shoshany, and M. Shub. Vegetation establishment on the southern israeli coastal sand dunes between the years 1965 and 1999. *Landscape Urban Plan.*, 67(1-4):141–156, 2004.

F. Laio, A. Porporato, L. Ridolfi, and I. Rodriguez-Iturbe. Mean first passage times of processes driven by white shot noise. *Phys. Rev. E*, 63(3):036105, 2001.

N. Lancaster. *Geomorphology of desert dunes*. Routledge, 2013.

S. Lanzoni. Experiments on bar formation in a straight flume: 1. uniform sediment. *Water Resour. Res.*, 36(11):3337–3349, 2000.

S.L. Lewis and M.A. Maslin. Defining the anthropocene. *Nature*, 519(7542):171, 2015.

S.P. Lin. Finite amplitude side-band stability of a viscous film. *J. Fluid Mech.*, 63 (3):417–429, 1974.

T-S. Lin and L. Kondic. Thin films flowing down inverted substrates: Two dimensional flow. *Phys. Fluids*, 22(5):052105, 2010.

J. Liu and J.P. Gollub. Onset of spatially chaotic waves on flowing films. *Phys. Rev. Lett.*, 70(15):2289, 1993.

T.B. Liverpool and S.F. Edwards. Dynamics of a meandering river. *Phys. Rev. Lett.*, 75(16):3016, 1995.

H. Ma, J.A. Nittrouer, K. Naito, X. Fu, Y. Zhang, A.J. Moodie, Y. Wang, B. Wu, and G. Parker. The exceptional sediment load of fine-grained dispersal systems: Example of the Yellow River, China. *Sci. Adv.*, 3(5):e1603114, 2017.

E. Mantelli, C. Camporeale, and L. Ridolfi. Supraglacial channel inception: Modeling and processes. *Water Resour. Res.*, 51(9):7044–7063, 2015.

M. Marani, A. D'Alpaos, S. Lanzoni, L. Carniello, and A. Rinaldo. The importance of being coupled: Stable states and catastrophic shifts in tidal biomorphodynamics. *J. Geophys. Res-Earth*, 115(F4), 2010.

A. Martín-Pérez, R. Martín-García, and A. M. Alonso-Zarza. Diagenesis of a drapery speleothem from castañar cave: from dissolution to dolomitization. *Int. J. Speleol.*, 41(2):11, 2012.

F. McDermott. Palaeo-climate reconstruction from stable isotope variations in speleothems: a review. *Quaternary Sci. Rev.*, 23(7-8):901–918, 2004.

P. Meakin and B. Jamtveit. Geological pattern formation by growth and dissolution in aqueous systems. page rspa20090189, 2009.

D.M. Merritt and E.E. Wohl. Processes governing hydrochory along rivers: hydraulics, hydrology, and dispersal phenology. *Ecol. Appl.*, 12(4):1071–1087, 2002.

E. Meyer-Peter and R. Müller. Formulas for bed-load transport. IAHR, 1948.

P. A. Monkewitz. Subharmonic resonance, pairing and shredding in the mixing layer. *J. Fluid. Mech.*, 188:223–252, 1988.

D.R. Montgomery. River management: What's best on the banks? *Nature*, 388 (6640):328–329, 1997.

J. Mossa. Sediment dynamics in the lowermost Mississippi River. *Eng. Geol.*, 45 (1-4):457–479, 1996.

R. Muneepeerakul, A. Rinaldo, and I. Rodríguez-Iturbe. Effects of river flow scaling properties on riparian width and vegetation biomass. *Water Resour. Res.*, 43(12), 2007.

A.B. Murray and C. Paola. A cellular model of braided rivers. *Nature*, 371(6492): 54, 1994.

E. Naumburg, R. Mata-Gonzalez, R.G. Hunter, T. Mclendon, and D.W. Martin. Phreatophytic vegetation and groundwater fluctuations: a review of current research and application of ecosystem response modeling with an emphasis on great basin vegetation. *Environ. Man.*, 35(6):726–740, 2005.

K.G. Nayar, D. Panchanathan, G.H. McKinley, and J.H. Lienhard. Surface tension of seawater. *J. Phys. Chem. Ref. Data*, 43(4):043103, 2014.

J.M. Nield and A.C. Baas. The influence of different environmental and climatic conditions on vegetated aeolian dune landscape development and response. *Global Planet. Change*, 64(1-2):76–92, 2008.

W. Nusselt. Die oberflachenkondesation des wasserdamffes the surface condensation of water. *Zetrschr. Ver. Deutch. Ing.*, 60:541–546, 1916.

N. Ogawa and Y. Furukawa. Surface instability of icicles. *Phys. Rev. E*, 66:041202, 2002.

A. Oron and P. Rosenau. Nonlinear evolution and breaking of interfacial rayleigh–taylor waves. *Phys. Fluids A-Fluid*, 1(7):1155–1165, 1989.

G. Parker. Sediment inertia as cause of river antidunes. *J. Hydraul. Div-Asce*, 101 (2):211–221, 1975a.

G. Parker. Meandering of supraglacial melt streams. *Water Resour. Res.*, 11(4): 551–552, 1975b.

G. Parker. On the cause and characteristic scales of meandering and braiding in rivers. *J. Fluid Mech.*, 76(3):457–480, 1976.

G. Parker, Y. Shimizu, G.V. Wilkerson, E.C. Eke, J.D. Abad, J.W. Lauer, C. Paola, W.E. Dietrich, and V.R. Voller. A new framework for modeling the migration of meandering rivers. *Earth Surf. Proc. Land.*, 36(1):70–86, 2011.

Nicola Pasquale, P Perona, R Francis, and Paolo Burlando. Effects of streamflow variability on the vertical root density distribution of willow cutting experiments. *Ecol. Eng.*, 40:167–172, 2012.

P. Perona, P. Molnar, B. Crouzy, E. Perucca, Z. Jiang, S. McLelland, D. Wüthrich, K. Edmaier, R. Francis, C. Camporeale, et al. Biomass selection by floods and related timescales: Part 1. experimental observations. *Adv. Water Resour.*, 39: 85–96, 2012.

P. Perona, B. Crouzy, S. McLelland, P. Molnar, and C. Camporeale. Ecomorphodynamics of rivers with converging boundaries. *Earth Surf. Proc. Land.*, 39(12): 1651–1662, 2014.

E. Perucca, C. Camporeale, and L. Ridolfi. Significance of the riparian vegetation dynamics on meandering river morphodynamics. *Water Resour. Res.*, 43(3), 2007.

G. Poots. *Ice and snow accretion on structures*, volume 338. Research Studies Press, 1996.

S. B. Pope. *Turbulent flows*. Cambridge University Press, 2000.

C.J. Proctor, A. Baker, W.L. Barnes, and M.A. Gilmour. A thousand year speleothem proxy record of north atlantic climate from scotland. *Clim. Dynam.*, 16(10-11): 815–820, 2000.

T. Prokopiou, M. Cheng, and H. Chang. Long waves on inclined films at high reynolds number. *J. Fluid Mech.*, 222:665–691, 1991.

K. Pye and H. Tsoar. *Aeolian sand and sand dunes*. Springer Science & Business Media, 2008.

M.T. Ramirez and M.A. Allison. Suspension of bed material over sand bars in the Lower Mississippi River and its implications for mississippi delta environmental restoration. *Journal of Geophys. Res.-Earth*, 118(2):1085–1104, 2013.

O. Reynolds. An experimental investigation of the circumstances which determine whether the motion of water shall he direct or sinuous, and of the law of resistance in parallel channels. *Philos. T. R. Soc. Lond.*, 174:935–982, 1883.

F. Ribas, A. Falques, H.E. De Swart, N. Dodd, R. Garnier, and D. Calvete. Understanding coastal morphodynamic patterns from depth-averaged sediment concentration. *Rev. of Geophys.*, 53(2):362–410, 2015.

K.J. Richards. The formation of ripples and dunes on an erodible bed. *J. Fluid Mech.*, 99(3):597–618, 1980.

L.C.V Rijn. Sediment transport, part ii: suspended load transport. *J. Hydraul. Eng.*, 110(11):1613–1641, 1984a.

L.C.V Rijn. Sediment transport, part iii: bed forms and alluvial roughness. *J. Hydraul. Eng.*, 110(12):1733–1754, 1984b.

A. Roberts. The utility of an invariant manifold description of the evolution of a dynamical system. *SIAM J. Math. Anal.*, 20(6):1447–1458, 1989.

D. Romanov, G. Kaufmann, and W. Dreybrodt. Modeling stalagmite growth by first principles of chemistry and physics of calcite precipitation. *Geochim. Cosmochim. Acta*, 72(2):423–437, 2008.

J.T. Rominger, A.F. Lightbody, and H.M. Nepf. Effects of added vegetation on sand bar stability and stream hydrodynamics. *J. Hydraulic. Eng.*, 136(12):994–1002, 2010.

P. Rosenau, A. Oron, and J.M. Hyman. Bounded and unbounded patterns of the benney equation. *Phys. Fluids A-Fluid*, 4(6):1102–1104, 1992.

L. Rubinšteĭn. *The Stefan problem*, volume 8. American Mathematical Soc., 2000.

C. Ruyer-Quil and P. Manneville. Modeling film flows down inclined planes. *Eur. Phys. J. B*, 6(2):277–292, 1998.

C. Ruyer-Quil and P. Manneville. Improved modeling of flows down inclined planes. *Eur. Phys. J. B*, 15(2):357–369, 2000.

F. Sabater, A. Butturini, E. MartÍ, I. Muñoz, A. Romaní, J. Wray, and S. Sabater. Effects of riparian vegetation removal on nutrient retention in a mediterranean stream. *J. N. Am. Benthol. Soc.*, 19(4):609–620, 2000.

R. Schielen, A. Doelman, and H.E. De Swart. On the nonlinear dynamics of free bars in straight channels. *J. Fluid Mech.*, 252:325–356, 1993.

P.J. Schmid and D.S. Henningson. *Stability and transition in shear flows*, volume 142. Springer Science & Business Media, 2012.

G. Seminara. Fluvial sedimentary patterns. *Annu. Rev. Fluid Mech.*, 42:43–66, 2010.

A.J. Serlet, A. M. Gurnell, G. Zolezzi, G. Wharton, P. Belleudy, and C. Jourdain. Biomorphodynamics of alternate bars in a channelized, regulated river: an integrated historical and modelling analysis. *Earth Surf. Proc. Land.*, 2018.

M. B. Short, J. C. Baygents, and R. E. Goldstein. Stalactite growth as a free-boundary problem. *Phys. Fluids (1994-present)*, 17(8):083101, 2005.

M.B. Short, J.C. Baygents, and R.E. Goldstein. A free-boundary theory for the shape of the ideal dripping icicle. *Phys. Fluids*, 18(8):083101, 2006.

S. Silvestro, L.K. Fenton, D.A. Vaz, N.T. Bridges, and G.G. Ori. Ripple migration and dune activity on mars: Evidence for dynamic wind processes. *Geophys. Res. Lett.*, 37(20), 2010.

G.I. Sivashinsky and D.M. Michelson. On irregular wavy flow of a liquid film down a vertical plane. *Prog. Theor. Phys.*, 63(6):2112–2114, 1980.

A. Siviglia and A. Crosato. Numerical modelling of river morphodynamics: Latest developments and remaining challenges. *Adv. Water Resour.*, 93:1–3, 2016.

A. Siviglia, G. Stecca, D. Vanzo, G. Zolezzi, E. Toro, and M. Tubino. Numerical modelling of two-dimensional morphodynamics with applications to river bars and bifurcations. *Adv. Water Resour.*, 52:243–260, 2013.

J. Stefan. Über die theorie der eisbildung, insbesondere über die eisbildung im polarmeere. *Annalen der Physik*, 278(2):269–286, 1891.

J.C. Stella, P.M. Rodríguez-González, S. Dufour, and J. Bendix. Riparian vegetation research in mediterranean-climate regions: common patterns, ecological processes, and considerations for management. *Hydrobiologia*, 719(1):291–315, 2013.

K. Stewartson and J.T. Stuart. A non-linear instability theory for a wave system in plane poiseuille flow. *J. Fluid Mech.*, 48(03):529–545, 1971.

M.R. Sweeney, H. Lu, M. Cui, J.A. Mason, H. Feng, and Z. Xu. Sand dunes as potential sources of dust in northern china. *Sci. China Earth Sci.*, 59(4):760–769, 2016.

A.M. Talmon, N. Struiksma, and M.C.L.M. Van Mierlo. Laboratory measurements of the direction of sediment transport on transverse alluvial-bed slopes. *J. Hydraul. Res.*, 33(4):495–517, 1995.

N. Tambroni and P. Blondeaux. Sand banks of finite amplitude. *J. Geophys. Res. Oceans*, 113(C10), 2008.

N. Tambroni, J. F. da Silva, R.W. Duck, S.J. McLelland, C. Venier, and S. Lanzoni. Experimental investigation of the impact of macroalgal mats on the wave and current dynamics. *Adv. Water Resour.*, 93:326–335, 2016.

J. Tollefson. Us science envoy resigns in protest at trump policies. *Nature News*, 548 (7669):509, 2017.

M. Tubino. Growth of alternate bars in unsteady flow. *Water Resour. Res.*, 27(1): 37–52, 1991.

M. Tubino, R. Repetto, and G. Zolezzi. Free bars in rivers. *J. Hydraul. Res.*, 37(6): 759–775, 1999.

K. Ueno. Characteristics of the wavelength of ripples on icicles. *Phys. Fluids (1994-present)*, 19(9):093602, 2007.

K. Ueno and M. Farzaneh. Linear stability analysis of ice growth under supercooled water film driven by a laminar airflow. *Phys. Fluids*, 23(4):042103, 2011.

K. Ueno, M. Farzaneh, S. Yamaguchi, and H. Tsuji. Numerical and experimental verification of a theoretical model of ripple formation in ice growth under supercooled water film flow. *Fluid. Dyn. Res.*, 42(2):025508, 2009a.

K. Ueno, M. Farzaneh, S. Yamaguchi, and H. Tsuji. Numerical and experimental verification of a theoretical model of ripple formation in ice growth under supercooled water film flow. *Fluid Dyn. Res.*, 42(2):025508, 2009b.

J. W. van de Meene and L.C. van Rijn. The shoreface-connected ridges along the central dutch coast—part 1: field observations. *Cont. Shelf Res.*, 20(17): 2295–2323, 2000.

R. Vesipa, C. Camporeale, and L. Ridolfi. Effect of river flow fluctuations on riparian vegetation dynamics: Processes and models. *Adv. Water Resour.*, 110:29–50, 2017.

V. Vins, M. Fransen, J. Hykl, and J. Hruby. Surface tension of supercooled water determined by using a counterpressure capillary rise method. *J. Phys. Chem. B*, 119(17):5567–5575, 2015.

F. Visconti, C. Camporeale, and L. Ridolfi. Role of discharge variability on pseudo-meandering channel morphodynamics: Results from laboratory experiments. *J. Geophys. Res. Earth Surf.*, 115(F4), 2010.

G. Vittori and P. Blondeaux. Sand ripples under sea waves part 2. Finite-amplitude development. *J. Fluid. Mech.*, 218:19–39, 1990.

X. Wang, F. Chen, E. Hasi, and J. Li. Desertification in china: an assessment. *Earth-Sci. Rev.*, 88(3-4):188–206, 2008.

C.N. Waters, J. Zalasiewicz, C. Summerhayes, A. D. Barnosky, C. Poirier, A. Gałuszka, A. Cearreta, M. Edgeworth, E.C. Ellis, M. Ellis, et al. The anthropocene is functionally and stratigraphically distinct from the holocene. *Science*, 351 (6269):aad2622, 2016.

B.T. Werner and T.M. Fink. Beach cusps as self-organized patterns. *Science*, 260 (5110):968–971, 1993.

S. Wiggins. *Introduction to applied nonlinear dynamical systems and chaos*, volume 2. Springer Science & Business Media, 2003.

D.C. Wilcox. *Turbulence modeling for CFD*, volume 2. DCW industries La Canada, CA, 1998.

E. Wohl, S.N. Lane, and A. C. Wilcox. The science and practice of river restoration. *Water Resour. Res.*, 51(8):5974–5997, 2015.

W. Wu and S.S. Wang. Formulas for sediment porosity and settling velocity. *J. Hydraul. Res.*, 132(8):858–862, 2006.

M. Yokokawa, N. Izumi, K. Naito, G. Parker, T. Yamada, and R. Greve. Cyclic steps on ice. *J. Geophys. Res. Earth Surf.*, 121(5):1023–1048, 2016.

D.P. Zhang and T. Sunamura. Multiple bar formation by breaker-induced vortices: a laboratory approach. In *Coastal Engineering 1994*, pages 2856–2870. 1995.

Appendix A

Appendix for Chapter 2

A.1 Closure relationships for the SWE

The closure relationships necessary to solve the (2.1)-(2.4) system are furnished hereafter. The dimensionless shear stress is defined as

$$(\tau_s, \tau_n) = C_f\,(U,V)\,\sqrt{U^2+V^2}, \tag{A.1}$$

where the friction factor C_f can be determined by means of the Einstein et al. (1950) formula for plane bed

$$C_f = \left(6+2.5\log\frac{D}{2.5d_s}\right)^{-2}, \tag{A.2}$$

or from Engelund and Hansen (1967) for a dune covered bed

$$\theta' = 0.06+0.4\,\theta^2, \tag{A.3}$$

$$C_f = \frac{\theta}{\theta'}\left(6+2.5\log\frac{\theta' D}{2.5\,\theta\,d_s}\right)^{-2}. \tag{A.4}$$

In (A.3)-(A.4), θ and $d_s = \hat{d}/\hat{D}_0$ are the Shield stress and the relative roughness, respectively, and bedload transport is defined as follows:

$$(Q_s^b, Q_n^b) = (\cos\alpha, \sin\alpha)\Phi, \tag{A.5}$$

with α being here the angle between the average particle path and the longitudinal direction, which is assumed to be small, so that

$$\cos\alpha \sim 1, \qquad \sin\alpha \sim \frac{V}{\sqrt{U^2+V^2}} - \frac{r}{\beta\sqrt{\theta}}\partial_n\eta, \tag{A.6}$$

with $r=0.56$ (Talmon et al., 1995). Bedload intensity Φ in (A.5) is defined through the Meyer Peter and Muller formula

$$\Phi = 8\,(\theta' - 0.047)^{3/2}, \tag{A.7}$$

where $\theta' = \theta$ if there are no bedforms.

A.2 Asymptotic expansion for ψ

A.2.1 Settling velocity

The settling velocity can be computed as

$$\hat{W}_s = \frac{P}{Q}\frac{\nu}{\hat{d}}\left[\sqrt{\frac{1}{4}+\left(\frac{4Q}{3P^2}d^3\right)^{(1/q)}} - \frac{1}{2}\right]^q, \qquad d = \hat{d}\left(\frac{\Delta g}{\nu^2}\right)^{1/3}, \tag{A.8}$$

where d is the dimensionless particle diameter, ν is the water kinematic viscosity and $P=53.5\exp(-0.65S_p)$, $Q=5.65\exp(-2.5S_p)$, $q=0.7+0.9S_p$ with shape parameter $S_p=0.7$ (Wu and Wang, 2006).

A.2.2 Relationships for ψ

In order to avoid repetitions of previous works, only the most important analytical relationships - or the information that is lacking in Appendix B of Federici and Seminara (2006)- are reported here. Reference should be made to that work for the expressions of the Rouse number Z, as well as the integrals I_1, I_2, K_0 and K_2.

It should be recalled that the expressions for suspended sediment that have not yet been expanded in the perturbations of the state variables, read

$$\psi^{(0)} = \frac{\bar{\psi}_0 K_0}{1-\lambda_p}, \qquad \psi^{(1)} = \frac{K_1 D(U\partial_s \bar{\psi}_0 + V\partial_n \bar{\psi}_0)}{1-\lambda_p}. \tag{A.9}$$

In (A.9), $\bar{\psi}_0$ is the depth-averaged concentration in uniform condition, and it reads

$$\bar{\psi}_0 = \frac{1}{1-y_r} C_e I_1, \tag{A.10}$$

where y_r is the dimensionless value of the reference elevation at which $\psi = \psi_e$ and ψ_e is the reference concentration that is defined from Rijn (1984a). It should be noted that the effective Shield stress θ' is defined as in (A.3), while the effective roughness that accounts for the effect of dunes reads

$$\varepsilon_e = 3\hat{d} + i\,\hat{\eta}_d 1.1 \left(1 - \mathrm{e}^{-25\hat{\eta}_d/\hat{\lambda}_d}\right) \tag{A.11}$$

where $i = 0$ ($i = 1$) for the plane (dune covered) bed. $\hat{\lambda}_d$ and $\hat{\eta}_d$ are the dune wavelength and height, respectively (Rijn, 1984b)

$$\hat{\lambda}_d = 7.3\hat{D}_0, \qquad \hat{\eta}_d = 0.11\,\hat{D}_0\, d_s^{0.3} \left[1 - \exp\left(-0.5\frac{\theta' - \theta_c}{\theta_c}\right)\right]\left(25 - \frac{\theta' - \theta_c}{\theta_c}\right), \tag{A.12}$$

with $\theta_c = 0.06$. For the evaluation of the expanded $\psi^{(0)}$ and $\psi^{(1)}$ in the state variables, eq. (2.22)-(2.23), these last expressions are needed

$$\psi_0^{(0)} = \frac{K_0 \bar{\psi}_0}{1-\lambda_p}, \qquad K_n = \frac{K_1 C_e}{(1-\lambda_p)(1-y_r)}, \tag{A.13}$$

where K_1 is reported in the next section.

A.2.3 Variation of parameters for the analytical solution of K_1

An expression for $K_1 = \sqrt{C_{f,0}} K_3/\kappa$ is required to evaluate the order δ correction in (A.9), where $C_{f,0}$ is the friction coefficient for the uniform condition and κ is the von Karman constant. From the asymptotic theory developed in Bolla Pittaluga and

Seminara (2003), we obtain

$$K_3 = \int_{y_r}^{1} C_{12} F_1(\xi) \mathrm{d}\xi - \log(y_0) \int_{y_r}^{1} C_{12} \mathrm{d}\xi, \tag{A.14}$$

where y_0 is the conventional dimensionless value of the reference elevation for no slip in uniform flows ($y_0 = y_r$ for a plane bed and $y_0 = 3\hat{d}$ for a dune covered bed) and C_{12} is obtained analytically by solving the following PDE problem

$$\frac{1}{Z}\{\partial_y [y\,(1-y)\,\partial_y]\} C_{12} + \partial_y C_{12} = \phi_0(y) F(y), \tag{A.15}$$

with the following boundary conditions

$$\frac{1}{Z} y(1-y)\partial_y C_{12} + C_{12} = 0 \qquad (y = 1), \tag{A.16}$$

$$\partial_y C_{12} = 0 \qquad (y = y_r). \tag{A.17}$$

Reference should be made to Bolla Pittaluga and Seminara (2003) for the expressions of $\phi_0(y)$, $F_1(y)$ and $F(y)$. By using the method of variation of parameters (Bender and Orszag, 2013) it is possible to write

$$C_{12} = u_1(y) v_1(y) + u_2(y) v_2(y), \tag{A.18}$$

where $v_1(y) = -(1-y)^Z/(Z y^{-Z})$ and $v_2 = 1$ are two linearly independent solution of the homogeneous equation (A.15), and the particular solutions $u_1(y)$ and $u_2(y)$ are given as

$$u_1(y) = -\int_y \frac{a_2(y') v_2(y')}{W(y')} \mathrm{d}y' + c_1, \quad u_2(y) = -\int_y \frac{a_2(y') v_1(y')}{W(y')} \mathrm{d}y' + c_2, \tag{A.19}$$

where $W(y) = -(1-y)^{-1+Z} y^{-1-Z}$ is the Wronskian of $v_1(y)$ and $v_2(y)$. The c_1 and c_2 constants are specified by imposing the boundary conditions (A.16)-(A.17) on (A.18).

A.3 Linear matrix

The corresponding algebraic eigenvalue problem of a generic harmonic m, reads $(\mathbf{L}_0^m \omega_m - \mathbf{L}_1^m)\mathbf{u}_1 = 0$, where $\mathbf{L}_0^m$ is a matrix with null elements, except for the lower

right entry, which is 1, while $\mathbf{L}_1^m$ reads:

$$\mathbf{L}_1^m = \begin{pmatrix} a_{11} & a_{12} & a_{13} & a_{14} \\ a_{21} & a_{22} & a_{23} & a_{24} \\ a_{31} & a_{32} & a_{33} & a_{34} \\ a_{41} & a_{42} & a_{43} & a_{44} \end{pmatrix}, \tag{A.20}$$

$$a_{11} = \frac{2C_{f,0}\beta}{C_t - 1} - \mathrm{i}k, \qquad a_{12} = 0, \qquad a_{13} = \frac{C_{f,0}(C_d + C_t - 1)\beta}{C_t - 1} - \frac{\mathrm{i}k}{Fr^2}, \tag{A.21}$$

$$a_{14} = -\frac{\mathrm{i}k}{Fr^2}, \qquad a_{21} = 0, \qquad a_{22} = -\mathrm{i}k - C_{f,0}\beta, \tag{A.22}$$

$$a_{23} = a_{24} = (-1)^m \frac{m\pi}{2Fr^2}, \qquad a_{31} = -\mathrm{i}k, \qquad a_{32} = (-1)^{m+1}\frac{m\pi}{2}, \tag{A.23}$$

$$a_{33} = -\mathrm{i}k, \qquad a_{34} = 0, \tag{A.24}$$

$$a_{41} = k\left(K_n k t_3 \delta + \frac{2\mathrm{i}\Upsilon\phi_0\phi_t}{C_t - 1} - i(t_1 + 1)\psi^{(0)}\right), \tag{A.25}$$

$$a_{43} = k\left(K_n k t_4 \delta + \frac{\mathrm{i}\Upsilon\phi_0(-C_t\phi_d + \phi_d + C_d\phi_t)}{C_t - 1} - \mathrm{i}\,(t_2 + 1)\psi^{(0)}\right), \tag{A.26}$$

$$a_{42} = -\frac{1}{2}(-1)^m m\pi(\Upsilon\phi_0 + \psi^{(0)}), \qquad a_{44} = -\frac{(-1)^{2m}m^2\pi^2\Upsilon r\phi_0}{4\sqrt{\theta_0}\beta}, \tag{A.27}$$

where the subscript 0 refers to the undisturbed uniform flow solution and according to Colombini et al. (1987)

$$C_d = \frac{1}{C_{f,0}}\frac{\partial C}{\partial D}, \qquad C_t = \frac{\theta_0}{C_{f,0}}\frac{\partial C}{\partial \theta}, \tag{A.28}$$

$$\phi_d = \frac{1}{\phi_0}\frac{\partial \phi}{\partial D}, \qquad \phi_t = \frac{\theta_0}{\phi_0}\frac{\partial \phi}{\partial \theta}. \tag{A.29}$$

The dispersion relation is readily achieved by imposing $|(\mathbf{L}_0^m\omega_m - \mathbf{L}_1^m)|$=0, from which one obtains the eigenvalue ω_m. The analytical expression of ω_m is particularly cumbersome. Thus, we have here reported the expressions that can be directly copied and pasted in numerical codes (in Python® language).

```
omegam=(sqrt(-1)*Fr**(-2)*k*kn**2*pd**2+(-2)*Cf0*((-1)+Ct)**(-1)*Fr**(-2
)*kn**2*pd**2*beta+(sqrt(-1)*(-1))*Fr**(-2)*((-1)+Fr**2)*k**2*(k+(sqrt(-1)*
(-1))*Cf0*beta)+(-1)*Cf0*((-1)+Ct)**(-1)*((-3)+Cd+Ct)*k*beta*(k+(sqrt(-1)*(
-1))*Cf0*beta))**(-1)*(((-1)+Ct)**(-1)*Fr**(-2)*k**2*Kn*(sqrt(-1)*((-1)+Ct)*
```

```
k*(k**2*(t3+(-1)*t4)+(-1)*kn**2*pd**2*t4)+Cf0*(((-1)+Ct)*k**2*(t3+(-1)*t4)+
kn**2*pd**2*((1+(-1)*Cd+(-1)*Ct)*t3+2*t4))*beta)*delta+sqrt(-1)*Fr**(-2)*((
-1)+Fr**2)*k**3*kn**2*pd**2*gamma*r*rtheta0**(-1)*beta**(-1)*phi0+(sqrt(-1)*
(-1))*Cf0**2*((-1)+Ct)**(-1)*((-3)+Cd+Ct)*k*kn**2*pd**2*gamma*r*rtheta0**(-1
)*beta*phi0+((-1)+Ct)**(-1)*Fr**(-2)*kn**4*pd**4*gamma*r*rtheta0**(-1)*beta*
*(-1)*((sqrt(-1)*(-1))*((-1)+Ct)*k+2*Cf0*beta)*phi0+((-1)+Ct)**(-1)*Fr**(-2)
*k**3*(k+(sqrt(-1)*(-1))*Cf0*beta)*(gamma*phi0*(phid+(-1)*Ct*phid+((-2)+Cd)*
phit)+((-1)+Ct)*(t1+(-1)*t2)*psi00)+((-1)+Ct)**(-1)*Fr**(-2)*k**2*kn**2*pd**
2*rtheta0**(-1)*(Cf0*(1+(-1)*Ct+((-4)+Cd+2*Ct)*Fr**2)*gamma*r*phi0+gamma*rt
heta0*phi0*((-1)+Ct+phid+(-1)*Ct*phid+Cd*phit)+(-1)*((-1)+Ct)*rtheta0*t2*ps
i00)+(sqrt(-1)*(-1))*Cf0*((-1)+Ct)**(-1)*Fr**(-2)*k*kn**2*pd**2*beta*(gamma*
phi0*((-3)+Cd+Ct+2*phid+2*phit)+((1+(-1)*Cd+(-1)*Ct)*t1+2*t2)*psi00))
```

In which: omegam= ω_m, kn = $\pi m/2$, Kn = K_n, pd = $(-1)^m$, gamma = γ, beta = β, delta = δ, Cf0 = $C_{f,0}$, Cd = C_d, Ct = C_t, phi0 = ϕ_0, phid = ϕ_d, phit = ϕ_t, theta0 = θ_0, rtheta0 = $\sqrt{\theta_0}$, psi00= $\psi_0^{(0)}$. Notice that to neglect suspended load is sufficient to set $\psi_0^{(0)} = t_1 = t_2 = t_3 = t_4 = 0$.

Moreover, at this link (http://www.envirofluidgroup.it/it/ricerca/164-bars.html) we furnish free and ready-to-use codes (a Jupyter notebook and a Mathematica toolbox), which provide bar sizes (wavelength and amplitude) for a given set of parameters.

A.4 CMP coefficients

The nonlinear coefficients of the amplitude equations are

$$P_j = 2\mathbf{N}[\mathbf{u}_1(-k,n)\mathrm{e}^{-\mathrm{i}ks}, \mathbf{u}_j(2k,n)\mathrm{e}^{2\mathrm{i}ks}] \cdot \mathbf{u}_1^{\dagger,*}(k,n)\mathrm{e}^{-\mathrm{i}ks}, \tag{A.30}$$

$$S_j = \mathbf{N}[\mathbf{u}_1(k,n)\mathrm{e}^{\mathrm{i}ks}, \mathbf{u}_1(k,n)\mathrm{e}^{\mathrm{i}ks}] \cdot \mathbf{u}_j^{\dagger,*}(2k,n)\mathrm{e}^{-2\mathrm{i}ks}, \tag{A.31}$$

where $\mathbf{N}$ is the symmetric function that contains all the second order non-linearities of the system (2.19), for which the internal product (2.26) is needed; † and * refer to the complex conjugate and adjoint, respectively. The Landau coefficient reads

$$\Xi = -\frac{P_1 S_1}{\omega_1(2k) - 2\omega_1(k)} - \frac{P_2 S_2}{\omega_2(2k) - 2\omega_1(k)}. \tag{A.32}$$

The analytical expression of Ξ is extremely long and cumbersome. Thus, we have reported in the following the expression that can be directly copied and pasted in numerical codes (in Python® language). Moreover, at this link (http://www.envirofluidgroup.it/it/ricerca/164-bars.html) we furnish free and ready-to-use codes (a Jupyter notebook and a Mathematica toolbox), which provide bar sizes (wavelength and amplitude) for a given set of parameters.

```
Xi=(-128/9)*((-1)+Ct)**(-1)*Fr**(-2)*k**2*((-16)*((-1)+Ct)*((-1)+Fr**2)*
k**3+(sqrt(-1)*8)*Cf0*(1+((-4)+Cd)*Fr**2+Ct*((-1)+2*Fr**2))*k**2*beta+sqrt(
-1)*Cf0*pi**2*beta+k*(((-1)+Ct)*pi**2+4*Cf0**2*((-3)+Cd+Ct)*Fr**2*beta**2))*
*(-2)*((-4)*((-1)+Ct)*((-1)+Fr**2)*k**3+(sqrt(-1)*(-4))*Cf0*(1+((-4)+Cd)*Fr
**2+Ct*((-1)+2*Fr**2))*k**2*beta+(sqrt(-1)*(-2))*Cf0*pi**2*beta+k*(((-1)+Ct
)*pi**2+4*Cf0**2*((-3)+Cd+Ct)*Fr**2*beta**2))**(-1)*((-4)*((-1)+Ct)*((-1)+F
r**2)*k**3+(sqrt(-1)*4)*Cf0*(1+((-4)+Cd)*Fr**2+Ct*((-1)+2*Fr**2))*k**2*beta
+(sqrt(-1)*2)*Cf0*pi**2*beta+k*(((-1)+Ct)*pi**2+4*Cf0**2*((-3)+Cd+Ct)*Fr**2*
beta**2))**(-3)*(2*(((-1)+Ct)*k*((-4)*((-1)+Fr**2)*k**2+pi**2)+(sqrt(-1)*2)
*Cf0*(2*(1+(-1)*Ct+((-4)+Cd+2*Ct)*Fr**2)*k**2+pi**2)*beta+4*Cf0**2*((-3)+Cd
+Ct)*Fr**2*k*beta**2)**(-1)*(4*((-1)+Ct)**(-1)*Fr**(-2)*k**2*Kn*(sqrt(-1)*(
(-1)+Ct)*k*(4*k**2*(t3+(-1)*t4)+(-1)*pi**2*t4)+Cf0*(4*((-1)+Ct)*k**2*(t3+(-1
)*t4)+pi**2*((1+(-1)*Cd+(-1)*Ct)*t3+2*t4))*beta)*delta+(sqrt(-1)*4)*Fr**(-2
)*((-1)+Fr**2)*k**3*pi**2*gamma*r*rtheta0**(-1)*beta**(-1)*phi0+(sqrt(-1)*(
-4))*Cf0**2*((-1)+Ct)**(-1)*((-3)+Cd+Ct)*k*pi**2*gamma*r*rtheta0**(-1)*beta*
phi0+((-1)+Ct)**(-1)*Fr**(-2)*pi**4*gamma*r*rtheta0**(-1)*beta**(-1)*((sqrt
(-1)*(-1))*((-1)+Ct)*k+2*Cf0*beta)*phi0+16*((-1)+Ct)**(-1)*Fr**(-2)*k**3*(k+
(sqrt(-1)*(-1))*Cf0*beta)*(gamma*phi0*(phid+(-1)*Ct*phid+((-2)+Cd)*phit)+((-
1)+Ct)*(t1+(-1)*t2)*psi00)+4*((-1)+Ct)**(-1)*Fr**(-2)*k**2*pi**2*rtheta0**(-
1)*(Cf0*(1+(-1)*Ct+((-4)+Cd+2*Ct)*Fr**2)*gamma*r*phi0+gamma*rtheta0*phi0*((
-1)+Ct+phid+(-1)*Ct*phid+Cd*phit)+(-1)*((-1)+Ct)*rtheta0*t2*psi00)+(sqrt(-1)
*(-4))*Cf0*((-1)+Ct)**(-1)*Fr**(-2)*k*pi**2*beta*(gamma*phi0*((-3)+Cd+Ct+2*p
hid+2*phit)+((1+(-1)*Cd+(-1)*Ct)*t1+2*t2)*psi00))+(-1)*(2*((-1)+Ct)*k*((-16
)*((-1)+Fr**2)*k**2+pi**2)+(sqrt(-1)*2)*Cf0*(8*(1+(-1)*Ct+((-4)+Cd+2*Ct)*Fr
**2)*k**2+pi**2)*beta+8*Cf0**2*((-3)+Cd+Ct)*Fr**2*k*beta**2)**(-1)*(16*((-1)
+Ct)**(-1)*Fr**(-2)*k**2*Kn*((sqrt(-1)*2)*((-1)+Ct)*k*(16*k**2*(t3+(-1)*t4)+
(-1)*pi**2*t4)+Cf0*(16*((-1)+Ct)*k**2*(t3+(-1)*t4)+pi**2*((1+(-1)*Cd+(-1)*C
t)*t3+2*t4))*beta)*delta+(sqrt(-1)*32)*Fr**(-2)*((-1)+Fr**2)*k**3*pi**2*gam
ma*r*rtheta0**(-1)*beta**(-1)*phi0+(sqrt(-1)*(-8))*Cf0**2*((-1)+Ct)**(-1)*(
```

```
(-3)+Cd+Ct)*k*pi**2*gamma*r*rtheta0**(-1)*beta*phi0+((-1)+Ct)**(-1)*Fr**(-2
)*pi**4*gamma*r*rtheta0**(-1)*beta**(-1)*((sqrt(-1)*(-2))*((-1)+Ct)*k+2*Cf0
*beta)*phi0+128*((-1)+Ct)**(-1)*Fr**(-2)*k**3*(2*k+(sqrt(-1)*(-1))*Cf0*beta)
*(gamma*phi0*(phid+(-1)*Ct*phid+((-2)+Cd)*phit)+((-1)+Ct)*(t1+(-1)*t2)*psi00
)+16*((-1)+Ct)**(-1)*Fr**(-2)*k**2*pi**2*rtheta0**(-1)*(Cf0*(1+(-1)*Ct+((-4)
+Cd+2*Ct)*Fr**2)*gamma*r*phi0+gamma*rtheta0*phi0*((-1)+Ct+phid+(-1)*Ct*phid
+Cd*phit)+(-1)*((-1)+Ct)*rtheta0*t2*psi00)+(sqrt(-1)*(-8))*Cf0*((-1)+Ct)**(-
1)*Fr**(-2)*k*pi**2*beta*(gamma*phi0*((-3)+Cd+Ct+2*phid+2*phit)+((1+(-1)*Cd
+(-1)*Ct)*t1+2*t2)*psi00)))**(-1)*(2*(128*Cf0*((-1)+Ct)*(4+(-3)*Cd+2*Ct)*k**
6*beta+(sqrt(-1)*4)*Cf0**2*((-22)+7*Cd**2+Cd*(7+(-14)*Ct)+31*Ct+(-23)*Ct**2)
*k**3*pi**2*beta**2+(sqrt(-1)*(-1))*Cf0**2*((-4)+Ct)*((-1)+Cd+Ct)*k*pi**4*be
ta**2+Cf0**3*((-1)+3*Cd**2+(-2)*Ct+3*Ct**2+Cd*((-2)+6*Ct))*pi**4*beta**3+Cf
0*k**2*pi**2*beta*(3*((-1)+Ct)*((-1)+Cd+Ct)*pi**2+4*Cf0**2*((-28)+3*Cd**2+C
d*(17+(-14)*Ct)+27*Ct+(-17)*Ct**2)*beta**2)+(sqrt(-1)*(-16))*((-1)+Ct)*k**5*
(((-1)+Ct)*pi**2+4*Cf0**2*(3*Cd+(-2)*(2+Ct))*beta**2)+(-8)*Cf0*((-1)+Ct)*k**
4*beta*(((-1)+5*Cd+6*Ct)*pi**2+8*Cf0**2*(3*Cd+(-2)*(2+Ct))*beta**2))*((sqrt
(-1)*(-1))*((-1)+Ct)*k**2*Kn*(t3+(-1)*Fr**2*t4)*delta+sqrt(-1)*Cf0*Fr**2*be
ta*(gamma*phi0*((-3)+Cd+Ct+2*phid+2*phit)+((1+(-1)*Cd+(-1)*Ct)*t1+2*t2)*psi
00)+k*(Cf0*Fr**2*Kn*(((-1)+Cd+Ct)*t3+(-2)*t4)*beta*delta+gamma*phi0*((-1)+C
t*(1+Fr**2*((-1)+phid))+2*phit+(-1)*Fr**2*((-1)+phid+Cd*phit))+(-1)*((-1)+C
t)*(t1+(-1)*Fr**2*t2)*psi00))+(-1)*(16*Cf0*((-2)+Cd)*((-1)+Ct)*k**4*beta+sq
rt(-1)*Cf0**2*(43+8*Cd**2+(-30)*Ct+3*Ct**2+Cd*((-35)+11*Ct))*k*pi**2*beta**
2+(-1)*Cf0**3*(3+Cd**2+2*Cd*((-2)+Ct)+(-4)*Ct+Ct**2)*pi**2*beta**3+2*Cf0*k**
2*beta*((1+(-1)*Ct)*((-7)+3*Cd+3*Ct)*pi**2+4*Cf0**2*((-2)+Cd)*((-3)+Cd+Ct)*
beta**2)+(sqrt(-1)*8)*k**3*(((-1)+Ct)**2*pi**2+Cf0**2*((-2)+Cd)*((-11)+5*Cd+
Ct)*beta**2))*((sqrt(-1)*(-4))*((-1)+Ct)*k**4*Kn*(t3+(-1)*Fr**2*t4)*delta+(
sqrt(-1)*(-2))*Cf0*pi**2*beta*(gamma*phi0+psi00)+k*((1+(-1)*Ct)*pi**2*(gamm
a*phi0+psi00)+(-4)*Cf0**2*Fr**2*beta**2*((-2)*gamma*phi0*(phid+phit)+((-3)+
Cd+Ct+(-1)*t1+Cd*t1+Ct*t1+(-2)*t2)*psi00))+4*k**3*(Cf0*Kn*((1+((-1)+Cd)*Fr**
2+Ct*((-1)+Fr**2))*t3+((-3)+Ct)*Fr**2*t4)*beta*delta+2*gamma*phi0*phit+psi0
0+(-1)*Ct*psi00+t1*psi00+(-1)*Ct*t1*psi00+Fr**2*(gamma*phi0*(((-1)+Ct)*phid
+(-1)*Cd*phit)+((-1)+Ct)*(1+t2)*psi00))+(sqrt(-1)*(-4))*Cf0*k**2*beta*(Cf0*F
r**2*Kn*(((-1)+Cd+Ct)*t3+(-2)*t4)*beta*delta+2*gamma*phi0*phit+psi00+(-1)*C
t*psi00+t1*psi00+(-1)*Ct*t1*psi00+Fr**2*(gamma*phi0*(((-3)+Ct)*phid+(-1)*(2+
Cd)*phit)+((-4)+(-1)*t1+Cd*(1+t1)+(-3)*t2+Ct*(2+t1+t2))*psi00))))*((sqrt(-1)
```

```
*(-1))*((-16)*Cf0*((-1)+Ct)*(4+(-3)*Cd+2*Ct)*k**6*beta+(sqrt(-1)*8)*Cf0**2*(
Cd+Cd**2+(-2)*Cd*Ct+(-2)*((-1)+Ct+Ct**2))*k**3*pi**2*beta**2+(sqrt(-1)*(-2))
*Cf0**2*((-4)+Ct)*((-1)+Cd+Ct)*k*pi**4*beta**2+Cf0**3*((-1)+3*Cd**2+(-2)*Ct+
3*Ct**2+Cd*((-2)+6*Ct))*pi**4*beta**3+(sqrt(-1)*(-8))*((-1)+Ct)*k**5*(((-1)+
Ct)*pi**2+4*Cf0**2*(3*Cd+(-2)*(2+Ct))*beta**2)+(-4)*Cf0*((-1)+Ct)*k**4*beta
*(((-5)+(-2)*Cd+3*Ct)*pi**2+4*Cf0**2*(3*Cd+(-2)*(2+Ct))*beta**2)+Cf0*k**2*pi
**2*beta*(3*((-1)+Ct)*((-1)+Cd+Ct)*pi**2+4*Cf0**2*(5+3*Cd**2+(-5)*Ct**2+(-2
)*Cd*(2+Ct))*beta**2))*((sqrt(-1)*(-4))*((-1)+Ct)*k**2*Kn*(t3+(-1)*Fr**2*t4
)*delta+sqrt(-1)*Cf0*Fr**2*beta*(gamma*phi0*((-3)+Cd+Ct+2*phid+2*phit)+((1+
(-1)*Cd+(-1)*Ct)*t1+2*t2)*psi00)+2*k*(Cf0*Fr**2*Kn*(((-1)+Cd+Ct)*t3+(-2)*t4
)*beta*delta+gamma*phi0*((-1)+Ct*(1+Fr**2*((-1)+phid))+2*phit+(-1)*Fr**2*((
-1)+phid+Cd*phit))+(-1)*((-1)+Ct)*(t1+(-1)*Fr**2*t2)*psi00))+(-1)*(((-1)+Ct)
*k+(sqrt(-1)*(-1))*Cf0*((-3)+Cd+Ct)*beta)*((sqrt(-1)*(-4))*Cf0*((-2)+Cd)*k**
3*beta+(sqrt(-1)*(-2))*Cf0*((-2)+Cd+Ct)*k*pi**2*beta+(-1)*Cf0**2*((-1)+Cd+C
t)*pi**2*beta**2+k**2*(((-1)+Ct)*pi**2+(-4)*Cf0**2*((-2)+Cd)*beta**2))*((sq
rt(-1)*(-32))*((-1)+Ct)*k**4*Kn*(t3+(-1)*Fr**2*t4)*delta+(sqrt(-1)*(-1))*Cf
0*pi**2*beta*(gamma*phi0+psi00)+k*((1+(-1)*Ct)*pi**2*(gamma*phi0+psi00)+(-4)
*Cf0**2*Fr**2*beta**2*((-2)*gamma*phi0*(phid+phit)+((-3)+Cd+Ct+(-1)*t1+Cd*t1
+Ct*t1+(-2)*t2)*psi00))+16*k**3*(Cf0*Kn*((1+((-1)+Cd)*Fr**2+Ct*((-1)+Fr**2))
*t3+((-3)+Ct)*Fr**2*t4)*beta*delta+2*gamma*phi0*phit+psi00+(-1)*Ct*psi00+t1*
psi00+(-1)*Ct*t1*psi00+Fr**2*(gamma*phi0*(((-1)+Ct)*phid+(-1)*Cd*phit)+((-1)
+Ct)*(1+t2)*psi00))+(sqrt(-1)*(-8))*Cf0*k**2*beta*(Cf0*Fr**2*Kn*(((-1)+Cd+Ct
)*t3+(-2)*t4)*beta*delta+2*gamma*phi0*phit+psi00+(-1)*Ct*psi00+t1*psi00+(-1
)*Ct*t1*psi00+Fr**2*(gamma*phi0*(((-3)+Ct)*phid+(-1)*(2+Cd)*phit)+((-4)+(-1
)*t1+Cd*(1+t1)+(-3)*t2+Ct*(2+t1+t2))*psi00))))+(1/128)*pi**4*((-4)*((-1)+Ct
)*((-1)+Fr**2)*k**3+(sqrt(-1)*2)*Cf0*(1+((-4)+Cd)*Fr**2+Ct*((-1)+2*Fr**2))*
k**2*beta+sqrt(-1)*Cf0*pi**2*beta+k*(((-1)+Ct)*pi**2+Cf0**2*((-3)+Cd+Ct)*Fr
**2*beta**2))**(-1)*((-4)*((-1)+Ct)*((-1)+Fr**2)*k**3+(sqrt(-1)*(-4))*Cf0*(1
+((-4)+Cd)*Fr**2+Ct*((-1)+2*Fr**2))*k**2*beta+(sqrt(-1)*(-2))*Cf0*pi**2*bet
a+k*(((-1)+Ct)*pi**2+4*Cf0**2*((-3)+Cd+Ct)*Fr**2*beta**2))**(-1)*(((sqrt(-1
)*2)*Fr**(-2)*k*pi**2+(-2)*Cf0*((-1)+Ct)**(-1)*Fr**(-2)*pi**2*beta+(sqrt(-1
)*(-4))*Fr**(-2)*((-1)+Fr**2)*k**2*(2*k+(sqrt(-1)*(-1))*Cf0*beta)+(sqrt(-1)*
2)*Cf0*((-1)+Ct)**(-1)*((-3)+Cd+Ct)*k*beta*((sqrt(-1)*2)*k+Cf0*beta))**(-1)*
(4*((-1)+Ct)**(-1)*Fr**(-2)*k**2*Kn*((sqrt(-1)*8)*((-1)+Ct)*k**3*(t3+(-1)*t4
)+(sqrt(-1)*(-2))*((-1)+Ct)*k*pi**2*t4+4*Cf0*((-1)+Ct)*k**2*(t3+(-1)*t4)*be
```

```
ta+Cf0*pi**2*((1+(-1)*Cd+(-1)*Ct)*t3+2*t4)*beta)*delta+(sqrt(-1)*8)*Fr**(-2)
*((-1)+Fr**2)*k**3*pi**2*gamma*r*rtheta0**(-1)*beta**(-1)*phi0+(sqrt(-1)*(-2
))*Cf0**2*((-1)+Ct)**(-1)*((-3)+Cd+Ct)*k*pi**2*gamma*r*rtheta0**(-1)*beta*p
hi0+((-1)+Ct)**(-1)*Fr**(-2)*pi**4*gamma*r*rtheta0**(-1)*beta**(-1)*((sqrt(
-1)*(-2))*((-1)+Ct)*k+2*Cf0*beta)*phi0+8*((-1)+Ct)**(-1)*Fr**(-2)*k**3*(2*k+
(sqrt(-1)*(-1))*Cf0*beta)*(gamma*phi0*(phid+(-1)*Ct*phid+((-2)+Cd)*phit)+((-
1)+Ct)*(t1+(-1)*t2)*psi00)+4*((-1)+Ct)**(-1)*Fr**(-2)*k**2*pi**2*rtheta0**(-
1)*(Cf0*(1+(-1)*Ct+((-4)+Cd+2*Ct)*Fr**2)*gamma*r*phi0+gamma*rtheta0*phi0*((
-1)+Ct+phid+(-1)*Ct*phid+Cd*phit)+(-1)*((-1)+Ct)*rtheta0*t2*psi00)+(sqrt(-1)
*(-2))*Cf0*((-1)+Ct)**(-1)*Fr**(-2)*k*pi**2*beta*(gamma*phi0*((-3)+Cd+Ct+2*p
hid+2*phit)+((1+(-1)*Cd+(-1)*Ct)*t1+2*t2)*psi00))+(sqrt(-1)*(1/2))*((-1)+Ct)
*Fr**2*(((-1)+Ct)*k*((-4)*((-1)+Fr**2)*k**2+pi**2)+(sqrt(-1)*2)*Cf0*(2*(1+(
-1)*Ct+((-4)+Cd+2*Ct)*Fr**2)*k**2+pi**2)*beta+4*Cf0**2*((-3)+Cd+Ct)*Fr**2*k*
beta**2)**(-1)*(4*((-1)+Ct)**(-1)*Fr**(-2)*k**2*Kn*(sqrt(-1)*((-1)+Ct)*k*(4*
k**2*(t3+(-1)*t4)+(-1)*pi**2*t4)+Cf0*(4*((-1)+Ct)*k**2*(t3+(-1)*t4)+pi**2*(
(1+(-1)*Cd+(-1)*Ct)*t3+2*t4))*beta)*delta+(sqrt(-1)*4)*Fr**(-2)*((-1)+Fr**2)
*k**3*pi**2*gamma*r*rtheta0**(-1)*beta**(-1)*phi0+(sqrt(-1)*(-4))*Cf0**2*((-
1)+Ct)**(-1)*((-3)+Cd+Ct)*k*pi**2*gamma*r*rtheta0**(-1)*beta*phi0+((-1)+Ct)*
*(-1)*Fr**(-2)*pi**4*gamma*r*rtheta0**(-1)*beta**(-1)*((sqrt(-1)*(-1))*((-1)
+Ct)*k+2*Cf0*beta)*phi0+16*((-1)+Ct)**(-1)*Fr**(-2)*k**3*(k+(sqrt(-1)*(-1))*
Cf0*beta)*(gamma*phi0*(phid+(-1)*Ct*phid+((-2)+Cd)*phit)+((-1)+Ct)*(t1+(-1)*
t2)*psi00)+4*((-1)+Ct)**(-1)*Fr**(-2)*k**2*pi**2*rtheta0**(-1)*(Cf0*(1+(-1)*
Ct+((-4)+Cd+2*Ct)*Fr**2)*gamma*r*phi0+gamma*rtheta0*phi0*((-1)+Ct+phid+(-1)
*Ct*phid+Cd*phit)+(-1)*((-1)+Ct)*rtheta0*t2*psi00)+(sqrt(-1)*(-4))*Cf0*((-1
)+Ct)**(-1)*Fr**(-2)*k*pi**2*beta*(gamma*phi0*((-3)+Cd+Ct+2*phid+2*phit)+((
1+(-1)*Cd+(-1)*Ct)*t1+2*t2)*psi00)))**(-1)*((-8)*k**2*(((-1)+Ct)*k+(sqrt(-1)
*(-1))*Cf0*((-3)+Cd+Ct)*beta)*((sqrt(-1)*(-1))*((-1)+Ct)*k*(4*k**2+pi**2)+2
*Cf0*((-2)*((-1)+Ct)*k**2+pi**2)*beta)*(((-1)+Ct)*k*((-4)*((-1)+Fr**2)*k**2+
pi**2)+(sqrt(-1)*2)*Cf0*(2*(1+(-1)*Ct+((-4)+Cd+2*Ct)*Fr**2)*k**2+pi**2)*bet
a+4*Cf0**2*((-3)+Cd+Ct)*Fr**2*k*beta**2)**(-2)*((-4)*((-1)+Ct)*((-1)+Fr**2)*
k**3+(sqrt(-1)*2)*Cf0*(1+((-4)+Cd)*Fr**2+Ct*((-1)+2*Fr**2))*k**2*beta+sqrt(-
1)*Cf0*pi**2*beta+k*(((-1)+Ct)*pi**2+Cf0**2*((-3)+Cd+Ct)*Fr**2*beta**2))**(-
1)*(pi**2*((sqrt(-1)*(-2))*((-1)+Ct)*k*Kn*t3*delta+gamma*phi0*((-1)+Ct+2*ph
it)+(-1)*((-1)+Ct)*t1*psi00)+2*Fr**2*k*(2*k+(sqrt(-1)*(-1))*Cf0*beta)*((sqr
t(-1)*2)*((-1)+Ct)*k*Kn*(t3+(-1)*t4)*delta+gamma*phi0*(phid+(-1)*Ct*phid+((
```

```
-2)+Cd)*phit)+((-1)+Ct)*(t1+(-1)*t2)*psi00))+sqrt(-1)*rtheta0**(-1)*beta**(-
1)*((-4)*((-1)+Ct)*((-1)+Fr**2)*k**3+(sqrt(-1)*4)*Cf0*(1+((-4)+Cd)*Fr**2+Ct
*((-1)+2*Fr**2))*k**2*beta+(sqrt(-1)*2)*Cf0*pi**2*beta+k*(((-1)+Ct)*pi**2+4*
Cf0**2*((-3)+Cd+Ct)*Fr**2*beta**2))**(-2)*((sqrt(-1)*4)*Cf0**2*pi**4*gamma*
r*beta**2*phi0*((-1)+2*phid+2*phit)+(sqrt(-1)*16)*((-1)+Ct)*((-1)+Fr**2)*k**
6*gamma*r*phi0*((-2)+Cd+2*((-1)+Ct)*phid+4*phit+(-2)*Cd*phit)+(-16)*k**5*be
ta*(Cf0*(2+((-5)+Cd)*Fr**2+Ct*((-2)+3*Fr**2))*gamma*r*phi0*(2+(-2)*((-1)+Ct)
*phid+(-4)*phit+Cd*((-1)+2*phit))+(-2)*((-1)+Ct)*rtheta0*(gamma*phi0*((-1)+C
t+(-1)*phid+Ct*phid+2*phit+(-1)*Cd*phit)+(-1)*((-1)+Ct)*((-1)+t1+(-1)*t2)*p
si00))+4*k**3*beta*(4*Cf0**3*((-3)+Cd+Ct)*Fr**2*gamma*r*beta**2*phi0*(2+(-2)
*((-1)+Ct)*phid+(-4)*phit+Cd*((-1)+2*phit))+Cf0*pi**2*gamma*r*phi0*(Cd**2*Fr
**2*(1+(-2)*phit)+2*((-2)+(-2)*(3+(-4)*Ct+Ct**2)*phid+((-1)+Ct)*Fr**2*(1+2*(
(-3)+Ct)*phid+(-2)*phit)+4*phit)+2*Cd*(2+(-1)*Fr**2*(2+phid+(-4)*phit)+(-4)*
phit+Ct*((-1)+Fr**2*(1+phid+(-2)*phit)+2*phit)))+8*Cf0**2*((-3)+Cd+Ct)*rthe
ta0*beta**2*(gamma*phi0*(1+phid+(-1)*Ct*(1+phid)+(-2)*phit+Cd*phit)+((-1)+C
t)*((-1)+t1+(-1)*t2)*psi00)+2*((-1)+Ct)*pi**2*rtheta0*(gamma*phi0*(((-1)+Ct
)*phid+(-1)*Cd*phit)+((-1)+Ct)*(1+t2)*psi00))+(sqrt(-1)*(-4))*k**4*(((-1)+C
t)*pi**2*gamma*r*phi0*((-2)+(-2)*((-1)+Ct)*((-2)+Fr**2)*phid+4*phit+Cd*((-2
)+Fr**2)*((-1)+2*phit))+(-4)*Cf0*beta**2*(Cf0*(1+((-7)+2*Cd)*Fr**2+Ct*((-1)+
3*Fr**2))*gamma*r*phi0*(2+(-2)*((-1)+Ct)*phid+(-4)*phit+Cd*((-1)+2*phit))+2
*((-4)+Cd+2*Ct)*rtheta0*(gamma*phi0*(1+phid+(-1)*Ct*(1+phid)+(-2)*phit+Cd*ph
it)+((-1)+Ct)*((-1)+t1+(-1)*t2)*psi00)))+2*Cf0*k*pi**2*beta*(pi**2*gamma*r*
phi0*(Cd+(-2)*Cd*phit+((-1)+Ct)*((-1)+4*phid+2*phit))+4*Cf0*((-3)+Cd+Ct)*be
ta**2*(Cf0*Fr**2*gamma*r*phi0*((-1)+2*phid+2*phit)+rtheta0*(gamma*phi0*((-1
)+Cd+Ct+2*phid+2*phit)+((1+(-1)*Cd+(-1)*Ct)*t1+2*(1+t2))*psi00)))+sqrt(-1)*
k**2*pi**2*(4*Cf0*Cd**2*gamma*beta**2*phi0*(2*rtheta0*phit+Cf0*Fr**2*r*((-1)
+2*phit))+(-2)*(((-1)+Ct)**2*pi**2*gamma*r*phi0*phid+4*Cf0**2*gamma*r*beta**
2*phi0*((-1)+(-4)*phid+Ct**2*Fr**2*phid+2*phit+(-1)*Ct*((-1)+2*Fr**2)*((-1)+
4*phid+2*phit)+Fr**2*((-4)+11*phid+8*phit))+4*Cf0*((-1)+Ct)*rtheta0*beta**2
*(gamma*phi0*(1+Ct*((-1)+phid)+(-5)*phid+(-2)*phit)+((-5)+(-1)*t1+(-5)*t2+Ct
*(1+t1+t2))*psi00))+Cd*(((-1)+Ct)*pi**2*gamma*r*phi0*((-1)+2*phit)+(-4)*Cf0*
beta**2*(Cf0*gamma*r*phi0*(2+(-4)*phit+Fr**2*((-1)+Ct+(-6)*phid+2*Ct*phid+2*
phit+(-2)*Ct*phit))+2*rtheta0*(gamma*phi0*(1+(-1)*phid+Ct*((-1)+phid+(-1)*p
hit)+3*phit)+((-1)+Ct)*(1+t1+t2)*psi00))))))*((sqrt(-1)*(-4))*k**2*(16*((-1
)+Ct)**2*k**4+(sqrt(-1)*4)*Cf0*((-1)+Ct)*((-4)+Cd+2*Ct)*k**3*beta+sqrt(-1)*
```

```
Cf0*((-1)+Ct)*((-5)+Cd+Ct)*k*pi**2*beta+(-4)*Cf0**2*((-3)+Cd+Ct)*pi**2*beta
**2+4*((-1)+Ct)*k**2*(((-1)+Ct)*pi**2+2*Cf0**2*((-3)+Cd+Ct)*beta**2))*((-4)*
((-1)+Ct)*((-1)+Fr**2)*k**3+(sqrt(-1)*4)*Cf0*(1+((-4)+Cd)*Fr**2+Ct*((-1)+2*F
r**2))*k**2*beta+(sqrt(-1)*2)*Cf0*pi**2*beta+k*(((-1)+Ct)*pi**2+4*Cf0**2*((-
3)+Cd+Ct)*Fr**2*beta**2))**(-1)*(pi**2*((sqrt(-1)*(-1))*((-1)+Ct)*k*Kn*t3*d
elta+gamma*phi0*((-1)+Ct+2*phit)+(-1)*((-1)+Ct)*t1*psi00)+4*Fr**2*k*(k+(sqr
t(-1)*(-1))*Cf0*beta)*(sqrt(-1)*((-1)+Ct)*k*Kn*(t3+(-1)*t4)*delta+gamma*phi
0*(phid+(-1)*Ct*phid+((-2)+Cd)*phit)+((-1)+Ct)*(t1+(-1)*t2)*psi00))+(-1)*rt
heta0**(-1)*beta**(-1)*(2*Cf0**2*pi**4*gamma*r*beta**2*phi0*((-1)+2*phid+2*
phit)+(-16)*((-1)+Ct)*((-1)+Fr**2)*k**6*gamma*r*phi0*((-2)+Cd+2*((-1)+Ct)*p
hid+4*phit+(-2)*Cd*phit)+(sqrt(-1)*(-8))*k**5*beta*((-1)*Cf0*((-1)+Ct+((-11)
+4*Cd)*Fr**2+3*Ct*Fr**2)*gamma*r*phi0*((-2)+Cd+2*((-1)+Ct)*phid+4*phit+(-2)*
Cd*phit)+(-8)*((-1)+Ct)*rtheta0*(gamma*phi0*((-1)+Ct+(-1)*phid+Ct*phid+2*ph
it+(-1)*Cd*phit)+(-1)*((-1)+Ct)*((-1)+t1+(-1)*t2)*psi00))+(sqrt(-1)*(-2))*k*
*3*beta*(8*Cf0**3*((-3)+Cd+Ct)*Fr**2*gamma*r*beta**2*phi0*(2+(-2)*((-1)+Ct)*
phid+(-4)*phit+Cd*((-1)+2*phit))+Cf0*pi**2*gamma*r*phi0*((-1)*Cd*(7+(-8)*Fr
**2*(2+phid+(-4)*phit)+Ct*(1+8*Fr**2*(1+phid+(-2)*phit)+(-2)*phit)+(-14)*phi
t)+4*Cd**2*Fr**2*((-1)+2*phit)+(-2)*((-8)+(3+(-4)*Ct+Ct**2)*phid+16*phit+((-
1)+Ct)*Fr**2*((-5)+((-6)+8*Ct)*phid+10*phit)))+16*Cf0**2*((-3)+Cd+Ct)*rthet
a0*beta**2*(gamma*phi0*(1+phid+(-1)*Ct*(1+phid)+(-2)*phit+Cd*phit)+((-1)+Ct)
*((-1)+t1+(-1)*t2)*psi00)+(-8)*((-1)+Ct)*pi**2*rtheta0*(gamma*phi0*(((-1)+Ct
)*phid+(-1)*Cd*phit)+((-1)+Ct)*(1+t2)*psi00))+4*k**4*(((-1)+Ct)*pi**2*gamma
*r*phi0*((-2)+(-2)*((-1)+Ct)*((-2)+Fr**2)*phid+4*phit+Cd*((-2)+Fr**2)*((-1)+
2*phit))+2*Cf0*beta**2*(Cf0*(1+((-7)+2*Cd)*Fr**2+Ct*((-1)+3*Fr**2))*gamma*r
*phi0*(2+(-2)*((-1)+Ct)*phid+(-4)*phit+Cd*((-1)+2*phit))+2*((-4)+Cd+2*Ct)*r
theta0*(gamma*phi0*(1+phid+(-1)*Ct*(1+phid)+(-2)*phit+Cd*phit)+((-1)+Ct)*((-
1)+t1+(-1)*t2)*psi00)))+(sqrt(-1)*(-1))*Cf0*k*pi**2*beta*(pi**2*gamma*r*phi
0*(Cd*((-4)+8*phit)+((-1)+Ct)*((-5)+2*phid+10*phit))+8*Cf0*((-3)+Cd+Ct)*bet
a**2*(Cf0*Fr**2*gamma*r*phi0*((-1)+2*phid+2*phit)+rtheta0*(gamma*phi0*((-1)+
Cd+Ct+2*phid+2*phit)+((1+(-1)*Cd+(-1)*Ct)*t1+2*(1+t2))*psi00)))+(-1)*k**2*p
i**2*(2*Cf0*Cd**2*gamma*beta**2*phi0*(Cf0*Fr**2*r*(1+(-2)*phit)+(-2)*rtheta
0*phit)+2*((-1)*((-1)+Ct)**2*pi**2*gamma*r*phi0*phid+2*Cf0**2*gamma*r*beta**
2*phi0*((-1)+(-4)*phid+Ct**2*Fr**2*phid+2*phit+(-1)*Ct*((-1)+2*Fr**2)*((-1)+
4*phid+2*phit)+Fr**2*((-4)+11*phid+8*phit))+2*Cf0*((-1)+Ct)*rtheta0*beta**2
*(gamma*phi0*(1+Ct*((-1)+phid)+(-5)*phid+(-2)*phit)+((-5)+(-1)*t1+(-5)*t2+Ct
```

```
*(1+t1+t2))*psi00))+Cd*(((-1)+Ct)*pi**2*gamma*r*phi0*((-1)+2*phit)+2*Cf0*bet
a**2*(Cf0*gamma*r*phi0*(2+(-4)*phit+Fr**2*((-1)+Ct+(-6)*phid+2*Ct*phid+2*ph
it+(-2)*Ct*phit))+2*rtheta0*(gamma*phi0*(1+(-1)*phid+Ct*((-1)+phid+(-1)*phi
t)+3*phit)+((-1)+Ct)*(1+t1+t2)*psi00))))))
```

In which: Xi= Ξ, pi = π, gamma = γ, beta = β, delta =δ, Cf0 = $C_{f,0}$, Cd = C_d, Ct = C_t, phi0 = ϕ_0, phid = ϕ_d, phit = ϕ_t, theta0 = θ_0, rtheta0 = $\sqrt{\theta_0}$, psi00= $\psi_0^{(0)}$. Notice that to neglect suspended load is sufficient to set $\psi_0^{(0)} = t_1 = t_2 = t_3 = t_4 = 0$.

Appendix B

Appendix for Chapter 3

In Fig. B.1, the finite amplitude of alternate bars is given in the parameter space.

B.1 Vegetation parameters

Fluvial trees usually experience maximum growth when the water table is at an optimum depth ($\hat{D}=\hat{l}_{opt}$). At lower stages the roots cannot tap the water ($\hat{D}<\hat{l}_2$), while at higher stages water logging occurs ($\hat{D}>\hat{l}_1$), thus reducing respiration and gas exchange in the root zone. Therefore, the carrying capacity for vegetation growth has been evaluated as a quadratic function (parabola) of the water depth $\hat{K}(\hat{D})$, e.g,

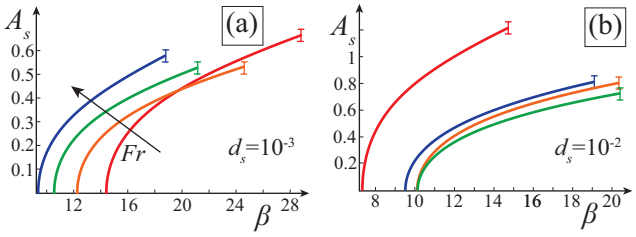

Fig. B.1 Finite amplitude bar. A_s versus β for diffferent Fr and d_s. Each line is plotted from the β_c of the first mode (alternate bars) to the β_c of the second mode (central bars). $Fr=\{0.4,0.7,1,1.3\}$ for panel (a) and $Fr=\{0.5,0.7,1,1.3\}$ for panel (b), with same color scale.

Camporeale and Ridolfi (2006),

$$\hat{K}(\hat{D}) = \begin{cases} \hat{a}[\hat{D}^2 - (\hat{l}_1 + \hat{l}_2)\hat{D} + \hat{l}_1\hat{l}_2] & \hat{l}_2 \leq \hat{D} \leq \hat{l}_1 \\ 0 & \text{otherwise,} \end{cases} \tag{B.1}$$

where $\hat{a} = 1/[(\hat{l}_1 - \hat{l}_{opt})(\hat{l}_2 - \hat{l}_{opt})]$ and we have assumed $\hat{l}_1 = -0.3$ m, $\hat{l}_{opt} = -0.8$ m, $\hat{l}_2 = -1.3$ m and $\hat{K}_{opt} = 5$ plants/m^2.

The dimensionless growth and decay factors of vegetation read

$$\nu_g = \frac{\hat{\nu}_g \hat{D}_0 \hat{K}_{opt}}{\hat{U}_0}\beta, \qquad \nu_d = \hat{\nu}_d \hat{D}_0 \hat{U}_0^2 \beta, \tag{B.2}$$

where $\hat{\nu}_g$ and $\hat{\nu}_d$ are the dimensional growth and decay coefficients, respectively. Considering the logistic growth of vegetation (see Eq. (4)), the time plants need to reach a mature state in optimum condition ($\hat{K} = \hat{K}_{opt}$) reads

$$\hat{t}_g = \int_{0.05\hat{K}_{opt}}^{0.95\hat{K}_{opt}} \left(\frac{\hat{\nu}_g \hat{\phi}}{\hat{K}_{opt} - \hat{\phi}} \right) d\hat{\phi} = \frac{5.88}{\hat{\nu}_g \hat{K}_{opt}}, \tag{B.3}$$

where ϕ is the number of plants per unit area. Assuming that in optimum condition mature vegetation develops in 20 years (growth rates of some riparian species are reported in Tab. 1 of Camporeale and Ridolfi (2006)), one obtains $\hat{\nu}_g \sim 10^{-9}$m^2/(s plants). Instead, the numerical value for the dimensional death factor $\hat{\nu}_d$ is not a trivial task as the processes leading to plant uprooting are still a research argument (e.g., Bankhead et al. (2017); Vesipa et al. (2017)) and no numerical data on the coefficient are avaiable at the present day. Our values are based on the experiments of Edmaier et al. (2011), in which uprooting times for sativa plants were calculated for a fixed flow rate. Introducing the experimental set-up data in Eq. 3.3 and integrating in time, one obtains $\hat{\nu}_d \sim 1000\hat{\nu}_g$, in agreement with the much faster process of uprooting with respect to growth. This estimate has some uncertainty and more research, both in field and experimental, should be performed, for example to understand how the root systems decreases the $\hat{\nu}_d$ value. However, Fig. 3.3c shows the weakly dependence of the results (AVI index and c_v^*) on the ratio between growth and death coefficients (notice the x-log scale), providing reliability to the outcomes.

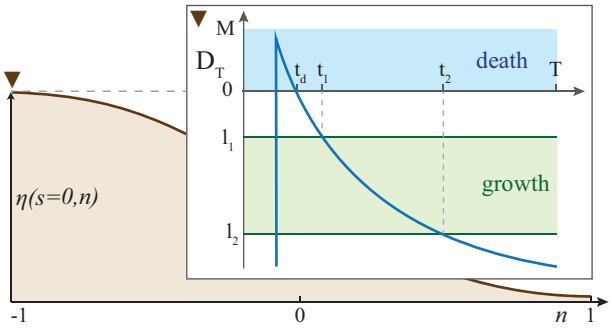

Fig. B.2 In the background, a river section in correspondence to a bar crest. In the inset, the flow depth, evaluated at the bar top (brown reverse triangle), versus time for a period Δt. $M = D_{max} + A_T$ and the depth (time) intervals M-0 (0-t_d) and l_1-l_2 (t_1-t_2) define the vegetation death and growth, respectively.

B.2 Threshold variation coefficient

In this section, we briefly explain how to evaluate c_v^*, which is the threshold variation coefficient above which plant growth is completely inhibited by flow variability, namely AVI decays to zero. An explicative sketch is provided in Fig. B.2, where a transversal river section accounting for the bar presence is shown. We obtain the parametric transition to a non-vegetated state at the bar top, which is the most favorable spatial point for vegetation to develop. To this regard, the inset of Fig. B.2 shows an exemplary trend for the water depth at the bar top. The effect may not be unique, e.g., there could be only death or growth or none of the two, but it represents the significant condition for the parametric transition from the vegetated to the bare state.

Let us start from the Compound Poisson Process for the water discharge. Once the bars are formed and the formative event is over, the flow decreases to ordinary values. At this point, the stochastic time series is substituted by a statistically equivalent periodic one, whose event of period Δt is $Q = Q_{max}(c_v)\exp(-t/\tau)$. The corresponding spatially extended water depth reads

$$D(s,n,t) = D_{max}(c_v)\,\mathrm{e}^{-\frac{3t}{5\mathscr{T}}} + A_s \sin\left(\frac{\pi n}{2}\right)\left(\hat{D}_1(k)\,\mathrm{e}^{\mathrm{i}ks} + c.c.\right) \tag{B.4}$$

where $\hat{D}_1$ is the water depth component of the first mode eigenvector. The first term in the r.h.s. of (B.4) comes from the periodic uniform condition, whereas the second term takes into account the morphological presence of the bars. Indeed at the bar

top, (B.4) reduces to

$$D_T(\Delta t) = D_{max}(c_v)\, \mathrm{e}^{-\frac{3t}{5\mathscr{T}}} + A_T \tag{B.5}$$

with the subscript T referring to bar top and $A_T = A_s[\hat{D}_1(k) + \hat{D}_1(-k)]$. From (B.5) and the inset in Fig. B.2, the times defining the uprooting and growth intervals read

$$t_d = \frac{5}{3}\mathscr{T} \ln\left(-\frac{D_{max}(c_v)}{A_T}\right) \qquad t_{1,2} = \frac{5}{3}\mathscr{T} \ln\left(\frac{D_{max}(c_v)}{l_{1,2} - A_T}\right) \tag{B.6}$$

where the existence of t_d,t_1,t_2 is not general as other conditions may be present, e.g., only death active ($t_d > \Delta t$). The threshold variation coefficient c_v^* can now be obtained by imposing the Floquet exponent (3.5) equal to zero and integrating the growth and death terms in the respective time intervals reported in ((B.6)). However, as the time boundaries depend on c_v, to find a solution for c_v^* is not a trivial task. A good approximation (error within 10%) for c_v^* is given by imposing $t_d(c_v^*) = 0$. This can be done without any loss of generality due to the very fast uprooting process and it simplifies considerably the calculus of the threshold variation coefficient ($D_{max}(c_v^*) = -A_T$). The approximated critical threshold so evaluated corresponds to eq. (3.6) and a comparison to the exact result obtained with the time intervals in (B.6) is furnished in Fig. 3.3c.

B.3 Rivers satellite photos and historical discharge series

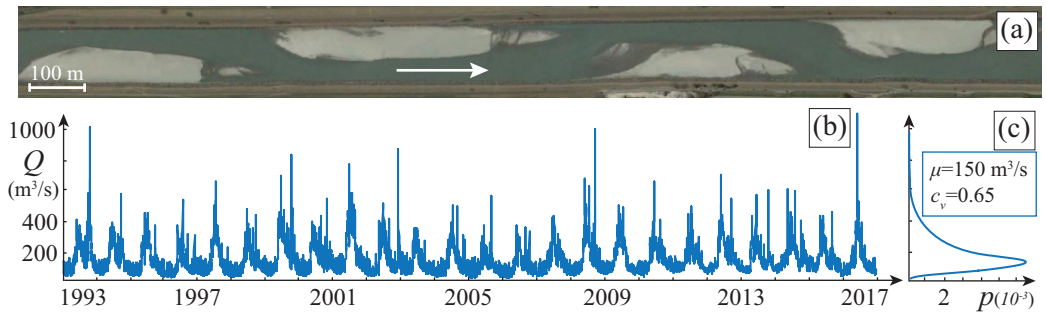

Fig. B.3 Alpine Rhine. (a) Satellite photo of the bare bars in the Alpine Rhine river near Meierhof, Liechtentstein 2012. (b-c) Mean daily discharge series measured at Domat (Switzerland) and its pdf. The data account for the confluence with the Landquart tributary just upstream the bars. The formative event has been considered as the 99% percentile, as lower flow rates are irrelevant to bar morphology (Adami et al., 2016; Tubino, 1991)

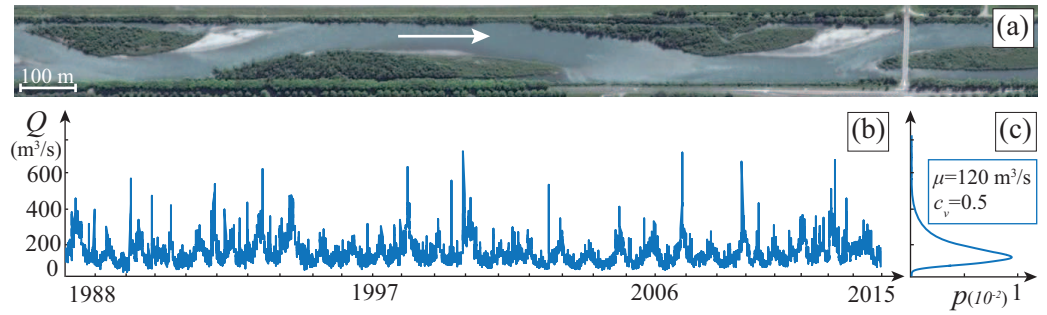

Fig. B.4 Isère. (a) Satellite photo of the vegetated bars in the Isère river near Arbin, France 2011. (b-c) Mean daily discharge series measured at Montmèlian and its pdf. The formative event has been considered as the 50- year flood.

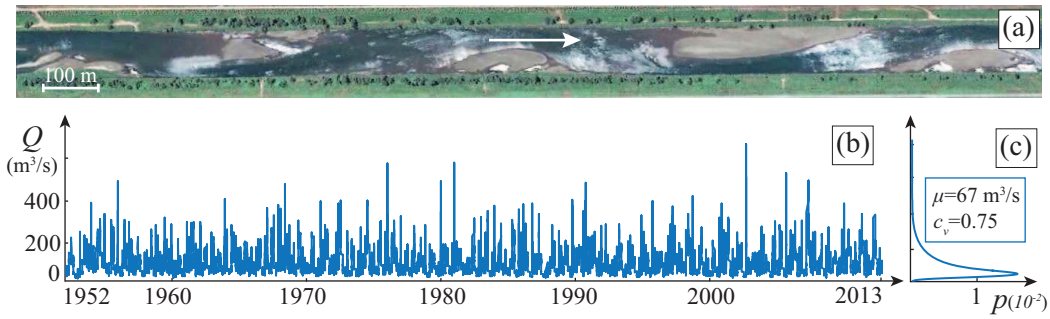

Fig. B.5 Vedder Canal. (a) Satellite photo of the bare bars in the Vedder canal near Barrowtown (Canada) in 2017. (b-c) Mean daily discharge series measured at Vedder Crossing and its pdf.

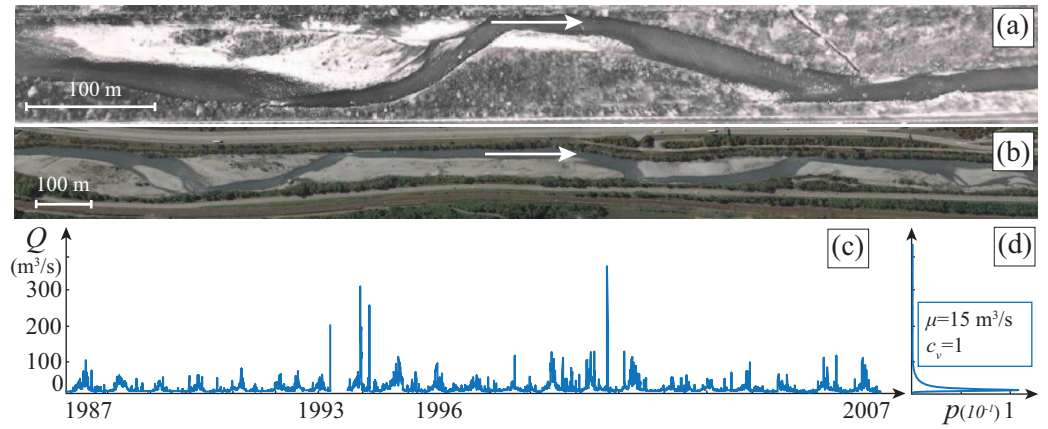

Fig. B.6 Arc river, before and after the highway construction (1994-1996). (a) Aerial photo of the vegetated bars near Les Champagnes (France) in 1989. (b) Satellite photo of the almost bare bars in 2015. (c-d) Mean daily discharge series measured at Saint-Remy de Maurienne and its pdf.

Appendix C

Appendix for Chapter 4

C.1 Order ε solution

Here we report the order ε solutions to the system (4.22)-(4.25):

$$u_1 = \frac{1}{6}(y-\eta)(y-2h-\eta)\{3\zeta\,(h+\eta)_x - 3ReWe\,[(h+\eta)_{xzz}+(h+\eta)_{zzz}] + Rehh_x\left[2h(\eta-y)-4h^2+(y-\eta)^2\right]\}, \tag{C.1}$$

$$w_1 = \frac{1}{2}(y-\eta)(-2h-\eta+y)\{\delta\,(h+\eta)_z - ReWe\,[(h+\eta)_{zzz}+(h+\eta)_{xxz}]\}, \tag{C.2}$$

$$v_1 = \int_\eta^y (u_{1,x}+w_{1,z})\,dy. \tag{C.3}$$

We point out that the expression for p_1 is not reported as it is not needed to reach eq. (4.26).

C.2 Linear matrix, dispersion relation and eigenvalues for the 2D model

The matrix associated with the linear system (4.50) depends on the environment considered. Its general form reads

$$\mathbf{L}_{I,K} = \begin{pmatrix} a_1 & a_2 \\ a_3 & a_4 \end{pmatrix}. \tag{C.4}$$

In the ice case

$$\begin{aligned} a_1 &= 30\,\mathrm{i}\tilde{k} + 5\tilde{K}^2\left(\zeta + \tilde{K}^2 ReWe\right) - 8\tilde{k}^2 Re + 15\Omega, & a_3 &= -b, \\ a_2 &= 5\tilde{K}^2(\tilde{K}^2 ReWe + \zeta), & a_4 &= 1 + b\gamma\omega \end{aligned}$$

and $\tilde{K}^2 = k^2 + \tilde{k}^2$. Imposing the determinant equal to zero gives the dispersion relation

$$5\tilde{K}^2(b\gamma\Omega + b + 1)(\tilde{K}^2 ReWe + \zeta) + (1 + b\gamma\Omega)\left(30\,\mathrm{i}\tilde{k} - 8\tilde{k}^2 Re + 15\Omega\right) = 0, \tag{C.5}$$

whose two complex conjugate solutions are the eigenvalues of the linear system

$$\Omega_{1,2} = \frac{1}{30b\gamma}\left(A \pm \sqrt{B}\right), \tag{C.6}$$

with

$$A = -15 - 30\,\mathrm{i}\tilde{k}\gamma - 5\tilde{K}^2 b\gamma\left(\zeta + \tilde{K}^2 ReWe\right) + 8\gamma\tilde{k}^2 Re,$$

$$\begin{aligned} B = -60b\gamma\left[2\alpha(15\,\mathrm{i} - 4R\alpha) + 5K^2(1+b)(\tilde{K}^2 ReWe + \zeta)\right] \\ + \left[15 + 2b\tilde{k}(15\,\mathrm{i} - 4Re\tilde{k})\gamma + 5K^2 r\gamma(\tilde{K}^2 ReWe + \zeta)\right]^2. \end{aligned}$$

In the karst case, the first line of the matrix remains the same, while $a_3 = -1$ and $a_4 = \gamma\omega$. Imposing the determinant equal to zero gives the dispersion relation

$$5\tilde{K}^2(\gamma\Omega + 1)(\tilde{K}^2 ReWe + \zeta) + \gamma\Omega\left(30\,\mathrm{i}\tilde{k} - 8\tilde{k}^2 Re + 15\Omega\right) = 0, \tag{C.7}$$

whose two complex conjugate solutions are the eigenvalues of the linear system

$$\Omega_{1,2} = \frac{1}{30\gamma}\left(A \pm \sqrt{B}\right), \tag{C.8}$$

with

$$A = -30\mathrm{i}\tilde{k} - 5\tilde{K}^2\left(\zeta + \tilde{K}^2 ReWe\right) + 8\tilde{k}^2 Re,$$

$$B = \gamma\{-300\tilde{K}^2\left(\zeta + \tilde{K}^2 ReWe\right) + \gamma\left[5\tilde{K}^2\left(\zeta + \tilde{K}^2 ReWe\right) + 2\tilde{k}(-4\tilde{k}Re + 15\mathrm{i})\right]^2\}.$$

C.3 Nonlinear coefficients

Following (Cheng and Chang, 1992), we define a function F_1

$$F_1(\alpha,\beta,\gamma,j,m,n) = \mathbf{N}[\mathbf{v}_m(\beta k)\,\mathrm{e}^{\mathrm{i}\beta kx}, \mathbf{v}_n(\gamma k)\,\mathrm{e}^{\mathrm{i}\gamma kx}] \cdot \hat{\mathbf{v}}_j(\alpha k)\,\mathrm{e}^{-\mathrm{i}\alpha kx}, \tag{C.9}$$

where (α,β,γ) are the indices for the interacting Fourier modes that satisfy the resonant condition $\alpha = \beta + \gamma$, and (j,m,n) stands for the eigenmodes. Let us consider two generic vectors $\mathbf{u} = (u_1,u_2)$ and $\mathbf{v} = (v_1,v_2)$, $\mathbf{N}[\mathbf{u},\mathbf{w}] = (N_1,N_2)$ is the symmetric function containing all second order non-linearities of system (4.58)

$$\begin{aligned} N_1 = \frac{1}{2}\{&u_{1,z}\left[\zeta\left(v_1+v_2\right)_z - ReWe\left(v_1+v_2\right)_{zzz}\right] \\ &+u_1\left[\zeta\left(v_1+v_2\right)_{zz} - ReWe\left(v_1+v_2\right)_{zzzz}\right]\} \\ +\frac{1}{2}\{&v_{1,z}\left[\zeta\left(u_1+u_2\right)_z - ReWe\left(u_1+u_2\right)_{zzz}\right] \\ &+v_1\left[\zeta\left(u_1+u_2\right)_{zz} - ReWe\left(u_1+u_2\right)_{zzzz}\right]\} \end{aligned} \tag{C.10}$$

and $N_2 = 0$. The interaction coefficients in (4.65)-(4.66) are:

$$
\begin{aligned}
P_1 &= F_1[1,1/2,1/2,1,1,1], & P_2 &= 2F_1[1,-1/2,3/2,1,1,1],\\
P_3 &= 2F_1[1/2,-1/2,1,1,1,1], & P_4 &= 2F_1[1/2,-1,3/2,1,1,1],\\
P_j^{(1)} &= F_1[1,1/2,1/2,1,j,1], & P_j^{(2)} &= 2F_1[1,-1/2,3/2,1,j,1],\\
P_j^{(3)} &= 2F_1[1,-1/2,3/2,1,1,j], & P_j^{(4)} &= 2F_1[1,-1,2,1,1,j],\\
P_j^{(5)} &= 2F_1[1,-3/2,5/2,1,1,j], & P_j^{(6)} &= 2F_1[1/2,-1/2,1,1,j,1],\\
P_j^{(7)} &= 2F_1[1/2,-1/2,1,1,1,j], & P_j^{(8)} &= 2F_1[1/2,-1,3/2,1,j,1],\\
P_j^{(9)} &= 2F_1[1/2,-1,3/2,1,1,j], & P_j^{(10)} &= 2F_1[1/2,-3/2,2,1,1,j],\\
S_j^{(1)} &= 2F_1[1/2,-1/2,1,j,1,1], & S_j^{(3)} &= F_1[1,1/2,1/2,j,1,1],\\
S_j^{(5)} &= 2F_1[3/2,1/2,1,j,1,1], & S_j^{(6)} &= F_1[2,1,1,j,1,1].
\end{aligned}
$$

After defining the function H

$$H(S,\alpha,m,n) = -S/[\omega_j(\alpha k) - \omega_1(mk) - \omega_1(nk)], \tag{C.11}$$

the coefficients of the center-unstable manifold projection (4.71) read

$$
\begin{aligned}
Z_j^{(1)} &= H[S_j^{(1)},1/2,-1/2,1], & Z_j^{(3)} &= H[S_j^{(3)},1,1/2,1/2],\\
Z_j^{(5)} &= H[S_j^{(5)},3/2,1/2,1], & Z_j^{(6)} &= H[S_j^{(6)},2,1,1].
\end{aligned}
$$

The coefficients of the projected equations (4.72)-(4.73) are

$$
\begin{aligned}
G_1 &= P_1^4 Z_1^{(6)} + P_2^4 Z_2^{(6)}, & G_2 &= P_2^{(1)} Z_2^{(1)} + P_2^{(3)} Z_2^{(5)},\\
G_5 &= P_2^{(6)} Z_2^{(1)} + P_2^{(9)} Z_2^{(5)}, & G_6 &= P_2^{(7)} Z_2^{(3)},\\
\tilde{G}_2 &= G_2 - P_2 P_5/(\omega_{3/2} - \omega_{1/2} - \omega_1), & \tilde{G}_5 &= G_5 - P_4 P_5/(\omega_{3/2} - \omega_{1/2} - \omega_1).
\end{aligned}
$$

Appendix D

Appendix for Chapter 5

D.1 Order ε solution

From eq. (5.42) with boundary conditions (5.47), the longitudinal velocity at order ε reads

$$u^{(1)} = \frac{N_{u^{(1)}}}{D_{u^{(1)}}}, \tag{D.1}$$

$$\begin{aligned} N_{u^{(1)}} = Re\,(y-\eta)\{h_x[h\,(Bih+1)^2(-2h-\eta+y)\left(2h(\eta-y)-4h^2+(y-\eta)^2\right) \\ +6BiMr_\Delta]+3We(Bih)+1)^2\,(h+\eta)_{xxx}\,(2h+\eta-y)\}, \\ D_{u^{(1)}} = 6(Bih+1)^2, \end{aligned}$$

where the time derivative of the free surface has been approximated with the zero-order kinematic condition (5.41) (Kalliadasis et al., 2011). The vertical velocity is obtained through the continuity equation at order ε, i.e., $v_1 = \int_\eta^y u_{1,x}\,dy$. Neglecting the concentration of dissolved impurities, for the reasons explaind in Sec. 5.2.3, the order ε temperature reads

$$T^{(1)} = -\frac{N_{T^{(1)}}}{D_{T^{(1)}}}, \tag{D.2}$$

$$\begin{aligned} N_{T^{(1)}} = BiPe_T\,r_\Delta h_x(y-\eta)\{20h^3\left(Bi^2\eta(\eta-2y)+Bi^2y^2+1\right)-8Bi^2h^5 \\ -5Bih^2\,(y-\eta)^2(-3Bi\eta+3Biy-4)+Bih(y-\eta)^3(-3Bi\eta+3Biy-20) \\ -10Bih^4+(y-\eta)^3(-3Bi\eta+3Biy-5)\}, \end{aligned}$$

$$D_{T^{(1)}} = 60(Bih+1)^3.$$